SAND2022-7930

SANDIA REPORT
SAND2022-xxxxx
Printed June 2022

Sandia
National
Laboratories

Final report of activities for the LDRD-CIS project #226834 titled: “Asymptotic preserving methods for fluid electron-fluid models in the large magnetic field limit with mathematically guaranteed properties”.

Ignacio Tomas (PI), John Shadid (Co-PI), Matthias Maier, Abner Salgado

Prepared by
Sandia National Laboratories
Albuquerque, New Mexico 87185
Livermore, California 94550

Issued by Sandia National Laboratories, operated for the United States Department of Energy by National Technology & Engineering Solutions of Sandia, LLC.

Available to DOE and DOE contractors from
U.S. Department of Energy
Office of Scientific and Technical Information
P.O. Box 62
Oak Ridge, TN 37831

Telephone: (865) 576-8401
Facsimile: (865) 576-5728
E-Mail: reports@osti.gov
Online ordering: http://www.osti.gov/scitech

Available to the public from
U.S. Department of Commerce
National Technical Information Service
5301 Shawnee Road
Alexandria, VA 22312

Telephone: (800) 553-6847
Facsimile: (703) 605-6900
E-Mail: orders@ntis.gov
Online order: https://classic.ntis.gov/help/order-methods

Final report of activities for the LDRD-CIS project #226834 titled: “Asymptotic preserving methods for fluid electron-fluid models in the large magnetic field limit with mathematically guaranteed properties”.

Ignacio Tomas (PI)
Computational Mathematics, MS-1320
Sandia National Laboratories
Albuquerque, NM 87185-1320
itomas@sandia.gov

John Shadid (Co-PI)
Center for Computing Research, MS-1320
Sandia National Laboratories
Albuquerque, NM 87185-1320
jnshadi@sandia.gov

Matthias Maier
Department of Mathematics, MS-3368
Texas A&M University
College Station, TX 77843-3368
maier@math.tamu.edu

Abner Salgado
Department of Mathematics
University of Tennessee,
Knoxville TN 37996
asalgad1@utk.edu

SAND2022-xxxxx

ACKNOWLEDGMENTS

This material is based upon work supported by the LDRD-CIS program of Sandia National Laboratories, project #226834 titled: “Asymptotic preserving methods for fluid electron-fluid models in the large magnetic field limit with mathematically guaranteed properties”. Their encouragement and financial and support throughout the development of this project is greatly acknowledged. Without their financial support prototype code-development and algorithmic evaluation would have not been possible.

CONTENTS

LIST OF FIGURES

LIST OF TABLES

1. INTRODUCTION

The current manuscript is a final report on the activities carried out under the Project LDRD-CIS #226834. In scientific terms, the work reported in this manuscript is a continuation of the efforts started with Project LDRD-express #223796 with final report of activities SAND2021-11481, see [83]. In this section we briefly explain what pre-existing developments motivated the current body of work and provide an overview of the activities developed with the funds provided.

The overarching goal of the current project LDRD-CIS #226834 and the previous project LDRD-express #223796 is the development of numerical methods with mathematically guaranteed properties in order to solve the Euler-Maxwell system of plasma physics and generalizations thereof. Even though Project #223796 laid out general foundations of space and time discretization of Euler-Maxwell system, overall, it was focused on the development of numerical schemes for purely electrostatic fluid-plasma models. In particular, the project developed a family of schemes with mathematically guaranteed robustness in order to solve the Euler-Poisson model. This model is an asymptotic limit where only electrostatic response of the plasma is considered. Its primary feature is the presence of a non-local force, the electrostatic force, which introduces effects with infinite speed propagation into the problem. Even though instantaneous propagation of perturbations may be considered nonphysical, there are plenty of physical regimes of technical interest where such an approximation is perfectly valid.

Within the scope of the proposed targets, project #223796 yielded a successful research program leading to a family of technically-meaningful mathematically-robust schemes in order to solve purely electrostatic fluid-plasma models. In the final report [83], the reader can also find early attempts at solving the Euler-Poisson model with a 'given' magnetic field (see [83, Section 8.2]). However, such computational results were only preliminary efforts, that did not have the same level of mathematical rigour supporting the other computational results presented in such report. Around the same time, related efforts within our ASCR-OFES project, using the code DREKAR, were exploring the development of computational capabilities in order to solve problems with large magnetic fields, low temperature, strong-vacuum, and small electron mass, see for instance [19, Section 7.5]. These developments aimed at the so-called cold-plasma E×B-drift limit of plasma physics. Concurrently, the work reported in [55] was also brought to our attention, pointing directly at the critical importance of E×B-drift limits and its related physics in the context of SNL applications. These and other factors motivated the developments of LDRD-CIS #226834 described in the current report.

Given the large number of applications associated to it, understanding the mathematical behavior of PDE models describing strongly magnetized plasmas and magnetic drift-limits is a topic of continuous and active scientific interest. The mathematical understanding of kinetic models and corresponding numerical schemes in the context of E×B-drift limits, and generally speaking 'strongly magnetized plasmas', is a topic that has received significant attention in the last two decades [40, 41, 38, 10, 71, 2, 57, 56, 39, 29, 58]. However, the body of scientific literature related to the numerical approximation of E×B-drift limits using plasma fluid-models is minimal. Two mathematically meaningful references on this topic are [27, 11].

For both, kinetic and fluid models, the problem is hard enough such that a few strong assumptions are usually made in order to make, at the very least, some partial progress. For instance, standard assumptions are that the magnetic field **B** is perfectly perpendicular to the velocity field. Similarly, it is very common to see that a large number of papers in the scientific literature assume that either the electric field **E** and/or the magnetic field **B** are ‘given’ (rather than computed self-consistently from the evolution equations). This approach allows to isolate difficulties, focus on a number of specific issues, and the development of rigorous analysis.

The fundamental difficulty associated to the numerical approximation of E×B-drift limits is caused by a change of type of the PDE. For instance, the barotropic Euler-Poisson system with a self-consistent electric field and a given magnetic field, can be considered to be a hyperbolic balance law subject to an elliptic constraint (a constraint that propagates at an infinite speed of propagation) coupling the density, momentum and electric field. The hyperbolic character is given by Euler’s equation of gas dynamics describing conservation of mass and momentum, while the elliptic character is given by the electric potential and the electrostatic force. Even though the notion of hyperbolic characteristics does not really apply to hyperbolic systems in one or more space dimensions, formally, we could say that the barotropic Euler’s system has three ‘characteristics’ in two space dimensions. In the asymptotic limit of zero electron-mass, the barotropic Euler-Poisson system with a given magnetic field loses a significant portion of its hyperbolic character: the original PDE system having four-scalar components collapses into a single scalar-valued non-local ODE describing the evolution of electron density, see Section 2.2. Formally, we could say that some hyperbolic characteristics ‘cease to exist’ in the limit of vanishing electron mass. This pathological PDE-behavior, leading to a radical change of type, reduction of the number of components of the PDE, and hyperbolic characteristics that ‘cease to exist’, is a staple of many PDE models of fluid mechanics and plasma physics.

Situations like this one are at the core of what is usually known as asymptotic preserving schemes [59, 34, 43]. Such schemes are meant to be capable of retaining formal consistency and stability of the scheme in the context of vanishingly-small parameters that may lead to a change of type of the original PDE. The usual procedure associated to the development of asymptotic-preserving schemes follows the pattern:

(i) From the original PDE: write down the formal limit-PDE when the small parameter goes to zero.
(ii) Develop a stable scheme for the limit-PDE.
(iii) Develop a scheme consistent with the original PDE that is also (formally) a ‘regular perturbation’ of the scheme developed in (ii).
(iv) Supply rigorous mathematical results (indisputable proofs) showing that the scheme is indeed asymptotic preserving.
(v) Supply computational evidence comparing the numerical behavior of the scheme developed in (iii) with any of the so-called ‘standard approaches’.

Bullets (i)-(v) define a computationally, mathematically, and technically sound road map in order to develop and evaluate numerical concepts. However, early departure from SNL of one the team members of this LDRD led to a significant reduction of the number of months available in order to execute such an ambitious plan. The original work plan underwent major restructuring: some the items associated to the work-plan (i)-(v), described above, where either cut-short, eliminated, or replaced by other not less important tasks. The work-plan actually executed with the funds supplied by LDRD-CIS would be much more accurately described by:

(i) Mathematical development of a stable scheme for the limit-PDE (magnetic drift-limit model). Essentially, all the mathematical work reached full completion. The primary motivation to have such a scheme at our disposal was having a reference scheme and numerical solution to compare with. However, this scheme was not implemented. Primary focus of the software development efforts were diverted into the isothermal Euler-Poisson system with a given magnetic field, which is a much more technically relevant model.

(ii) The activities developed in (i) required revisiting the scheme originally developed in [83] for the Euler-Poisson system. Some new developments in relationship to the preservation of Gauss-law were advanced. These developments were used for all the computational results used in this report.

(iii) Mathematical development and implementation of a semi-implicit scheme capable of preserving positivity of density, internal energy, and boundedness of the total energy (mechanical + potential) of the system. These activities were dominated by a heavy workload of software development, evaluation and bench-marking of the proposed ideas. An unintended, but welcome, consequence of this work is the development of a new computational technique for the efficient assembly of the electric potential problem that avoids Schur complements (in their entirety) and is readily compatible with matrix-free methods, see Section 4.4. The new scheme possesses quite a few provable mathematical properties that are explained in this report. But given the time constraints at place, we do not provide a proof of asymptotic preservation at this point in time.

(iv) The activities developed in (iii) required revisiting the pre-existing scientific literature of Diagonally Implicit Runge-Kutta (DIRK) methods [1, 21]. This activity was started as an ancillary line of research, however, it proved to be of critical importance for the success of the activities developed in (iii). The final outcome is an entirely new body of analysis of DIRK methods [81] that is significantly much more conclusive than any previous notion of algebraic stability. The results advanced in [81] are of critical importance in order to guarantee the energy-stability of the numerical scheme used to solve the Euler-Poisson system with a given magnetic field.

Overall, we believe that the outcomes from the above described activities (i)-(iv) have set the stage for the final goal of developing unconditionally robust numerical methods for full Euler-Maxwell system. The results presented in this report will lead to both: a body of scientific journal publications and improved knowledge that will guide the development of production SNL plasma codes and enable more advanced DOE computational efforts.

The outline of the current report is as follows: in Section 2 we describe the isothermal Euler-Poisson model with a given magnetic field. In Section 2.2 we derive the cold-plasma drift-limit of the isothermal Euler-Poisson system. In Section 2.3 we describe the basic mathematical properties satisfied by such drift-limit PDE-model. In Section 3 we layout the elements of the most straightforward scheme we could use in order to solve the drift-limit PDE-model. In Section 4 we describe a family of numerical schemes in order to solve the isothermal Euler-Poisson model with a given magnetic field. The choice of source-update scheme appears to be of critical importance for the overall performance the scheme. That is why in Section 4.3 we describe three choices of source-update scheme, and in Section 4.4 we explain how to develop an efficient computational implementation (we avoid Schur complements in their entirety). In Section 5 we establish, rigorously, the minimal structural conditions required by the scheme in order to satisfy global entropy-stability properties. Section 6 presents some targeted computational experiments. These experiments focus on a single critical numerical test: the

Diocotron instability. The computational setup of the Diocotron instability is thoroughly described in 6.2. In Sections 6.3-6.7 we provide strong computational evidence showing that the numerical schemes advanced in this report can indeed approximate and provide efficient solutions near the magnetic drift-limit without suffering degradation of their robustness or time-step size.

At this point, due to the compressed time-schedule, all the computational experiments provided in Section 6 offer mostly qualitative information. In other words, we present minimal quantitative metrics (e.g. convergence rates, growth-rates, etc). In spite of this, we strongly encourage the reader to take a serious look at the results advanced in Section 6: these computational experiments supply critical information in relationship to the proper design of schemes which, we believe, is very hard to challenge. A future follow-up report/paper with primary focus in quantitative metrics (convergence rates, growth rates, wall-clock time, etc) is planned.

2. ISOTHERMAL EULER-POISSON AND DRIFT-LIMITS

2.1. Euler-Poisson system with ‘given’ magnetic field.

The starting point of our discussion is the isothermal Euler-Poisson model with given magnetic field:

$$\partial_t \rho + \operatorname{div} \mathbf{p} = 0\,, \tag{1a}$$

$$\partial_t \mathbf{p} + \operatorname{div}(\rho^{-1}\mathbf{p}\mathbf{p}^\top + \mathbb{I}p) = -\tfrac{q_e}{m_e}\rho\nabla\varphi + \tfrac{q_e}{m_e}\mathbf{p}\times\mathbf{B} - \tfrac{1}{\mathscr{T}}\mathbf{p}\,, \tag{1b}$$

$$-\varepsilon\Delta\partial_t\varphi = -\tfrac{q_e}{m_e}\operatorname{div}\mathbf{p}\,, \tag{1c}$$

where $\rho = m_e n_e$, $\mathbf{p} = m_e n_e \mathbf{v}$ and $p = \theta\rho$, θ is the temperature, $\mathscr{T}$ has units of time. Here m_e is the specific electron mass, n_e is the particle number density, and $\mathbf{v}$ denotes the velocity. We assume that $\mathbf{B}$ is ‘given’ or ‘known’, but the electric potential φ is part of the unknown fields: it is computed in a self-consistent manner. We also assume that $|\mathbf{B}|_{\ell^2} \geq B^\flat > 0$ in the entirety of the domain. In the following remark we describe the primary stability property satisfied by PDE-system (1).

Remark 2.1 (Global entropy balance)**.** System (1a)-(1b) satisfies the following formal entropy flux-balance

$$\partial_t\eta(\mathbf{u}) + \operatorname{div}[\mathbf{v}\eta(\mathbf{u}) + \mathbf{v}\theta\rho] + \tfrac{1}{\mathscr{T}}\tfrac{|\mathbf{p}|^2}{\rho} = -\tfrac{q_e}{m_e}\nabla\varphi\cdot\mathbf{p}\,, \tag{2}$$

where $\mathbf{u} = [\rho, \mathbf{p}]^\top$ denotes the state of the hyperbolic subsystem (1a)-(1b), and $\eta(\mathbf{u}) = \frac{1}{2}\frac{|\mathbf{p}|^2}{\rho} + \theta\rho\ln\rho$ is its mathematical entropy, see for instance [77, p. 98]. In addition, (1c) satisfies the energy identity

$$\frac{\partial}{\partial t}\int_\Omega \tfrac{\varepsilon}{2}|\nabla\varphi|^2\,\mathrm{d}\boldsymbol{x} - \varepsilon\int_{\partial\Omega}\varphi\nabla\partial_t\varphi\cdot\mathrm{n}\,\mathrm{d}\boldsymbol{x} = \tfrac{q_e}{m_e}\int_\Omega \mathbf{p}\cdot\nabla\varphi\,\mathrm{d}\boldsymbol{x} - \tfrac{q_e}{m_e}\int_{\partial\Omega}\varphi\mathbf{p}\cdot\mathrm{n}\,\mathrm{d}\boldsymbol{x}\,. \tag{3}$$

Integrating (2) in space and adding it to (3) we get

$$\frac{\partial}{\partial t}\int_\Omega \eta(\mathbf{u}) + \tfrac{\varepsilon}{2}|\nabla\varphi|^2\,\mathrm{d}\boldsymbol{x} + \int_{\partial\Omega}\left[\tfrac{q_e}{m_e}\varphi\mathbf{p} + \big(\eta(\mathbf{u}) + \theta\rho\big)\mathbf{v} - \varepsilon\varphi\nabla\partial_t\varphi\right]\cdot\mathrm{n}\,\mathrm{d}\boldsymbol{s} + \int_\Omega \tfrac{1}{\mathscr{T}}\tfrac{|\mathbf{p}|^2}{\rho}\,\mathrm{d}\boldsymbol{x} = 0\,. \tag{4}$$

We highlight that (4) is just a formal balance, a consequence of assuming smoothness. The mathematical understanding of hyperbolic conservation laws is at its infancy [22, 3], in particular in two or more space dimensions. The mathematical understanding of hyperbolic balance laws is significantly less complete. PDE systems such as (1) should not be understood as 'physical models' per se, but rather as incomplete model descriptions. The most widely accepted consensus is that such models have to be understood as vanishing-viscosity limits, possibly complemented with vanishing-dissipation mechanisms. In such context we may replace (4) by

$$\frac{\partial}{\partial t}\int_{\Omega}\eta(\mathbf{u})+\tfrac{\varepsilon}{2}|\nabla\varphi|^2\,\mathrm{d}\boldsymbol{x}+\int_{\partial\Omega}\left[\tfrac{q_e}{m_e}\varphi\mathbf{p}+\big(\eta(\mathbf{u})+\theta\rho\big)\mathbf{v}-\varepsilon\varphi\nabla\partial_t\varphi\right]\cdot\mathrm{n}\,\mathrm{d}\boldsymbol{s}+\int_{\Omega}\tfrac{1}{\mathscr{T}}\tfrac{|\mathbf{p}|^2}{\rho}\,\mathrm{d}\boldsymbol{x}\leq 0\,. \tag{5}$$

Since $\int_{\Omega}\eta(\mathbf{u})+\frac{\varepsilon}{2}|\nabla\varphi|^2\,\mathrm{d}\boldsymbol{x}$ is not a norm, a positive definite quadratic functional, or a generalization of such concept, we say that $\int_{\Omega}\eta(\mathbf{u})+\frac{\varepsilon}{2}|\nabla\varphi|^2\,\mathrm{d}\boldsymbol{x}$ is the entropy of the system (1), and that (5) is an entropy-dissipation inequality, see for instance [61].

The goal of this manuscript is the development of schemes that attempt to preserve a discrete counterpart of (5): we may consider that vanishing-viscosity and vanishing-damping effects are not only consistent with the nature of the scheme but also desirable. This is just a bold assertion, that cannot be rigorously justified at this point in time. However, as we will see later in Sections 5 and 6.4, it appears to be correct and have major consequences in relationship to the proper design of numerical schemes.

2.2. Cold-plasma magnetic drift-limits.

Since $\rho=m_e n_e$ and $\mathbf{p}=m_e n_e\mathbf{v}$; where m_e is the electron mass, n_e is the electron number density, and $\mathbf{v}$ is the velocity; we can rewrite (1) as follows:

$$\partial_t n_e+\mathrm{div}\,(n_e\mathbf{v})=0\,, \tag{6a}$$

$$m_e\partial_t(n_e\mathbf{v})+m_e\mathrm{div}\,(n_e\mathbf{v}\mathbf{v}^{\top})+\nabla p=-q_e n_e\nabla\varphi+q_e n_e\mathbf{v}\times\mathbf{B}-\tfrac{m_e}{\mathscr{T}}n_e\mathbf{v}\,, \tag{6b}$$

$$-\varepsilon\Delta\partial_t\varphi=-q_e\mathrm{div}\,(n_e\mathbf{v})\,. \tag{6c}$$

Now, taking zero electron-mass limit $m_e\to 0^{+}$, system (6) reduces to:

$$\begin{aligned}\partial_t n_e+\mathrm{div}\,(n_e\mathbf{v})&=0\,,\\ \nabla p&=-q_e n_e\nabla\varphi+q_e n_e\mathbf{v}\times\mathbf{B}-\tfrac{m_e}{\mathscr{T}}n_e\mathbf{v}\,,\\ -\varepsilon\Delta\partial_t\varphi&=-q_e\mathrm{div}\,(n_e\mathbf{v})\,.\end{aligned} \tag{7a}$$

We can see that (7a) has no inertial terms, meaning, the velocity of the electrons can react instantaneously to any force. We define $\widehat{\mathbf{B}}=\mathbf{B}/|\mathbf{B}|$ and, for the sake of an argument, we neglect friction/resistive terms by setting $\mathscr{T}=+\infty$. Taking the dot product of (7a) with $\widehat{\mathbf{B}}$, and taking the cross of product of (7a) with $\widehat{\mathbf{B}}$ we get respectively: $\widehat{\mathbf{B}}$:

$$\nabla p\cdot\widehat{\mathbf{B}}=-q_e n_e\nabla\varphi\cdot\widehat{\mathbf{B}} \tag{8}$$

$$\nabla p\times\widehat{\mathbf{B}}=-q_e n_e\nabla\varphi\times\widehat{\mathbf{B}}+q_e n_e(\mathbf{v}\times\mathbf{B})\times\widehat{\mathbf{B}} \tag{9}$$

It is well-known that the difficulties associated to expression (8) are very fast pressure waves along the magnetic field lines [27, 11, 25]. On the other hand, the nature of (9), at least in the ‘pressureless’ or ‘cold-plasma’ limit (i.e., $\theta = 0$), is the presence of very high-frequency oscillatory phenomena. We may be inclined to say that model (1) is a multiscale problem, containing not only the time-scales associated to hyperbolic waves (material transport and acoustic waves) but also high-frequency ‘ringing’ associated to the source terms. We may simplify model (1) in order to eliminate, completely, all high-frequencies and obtain a model capable of capturing low-frequency transport-like waves that are representative of macroscopic motions. In order to further delve into this issue, we make the following assumptions on the entirety of the manuscript:

(A1) Two-dimensional hydrodynamics and electrostatics, combined with perpendicular magnetic fields, more precisely:

$$\mathbf{v} = [\mathbf{v}_1, \mathbf{v}_2, 0]^\top , \ \ \nabla\varphi = [\partial_x\varphi, \partial_y\varphi, 0]^\top \ , \ \ \mathbf{B} = [0, 0, B]^\top .$$

Therefore, we have the following orthogonality properties

$$\mathbf{v}\cdot\mathbf{B} \equiv 0\,,\ \nabla\varphi\cdot\mathbf{B} \equiv 0\,,\ \nabla p\cdot\mathbf{B} \equiv 0\,.$$

Although it is not strictly necessary, in order to fix ideas, we will assume that $B = const$ in time and space. We note however, that the vast majority of the results presented in this report hold true well beyond the context of such assumption.

(A2) Temperature is negligible, i.e. $\theta \cong 0$, $p \cong 0$, $\nabla p \cong 0$. Therefore, the presence of fast pressure waves related to (8) are not of our primary concern in this manuscript[1].

Using identity

$$\mathbf{A}\times(\mathbf{B}\times\mathbf{C}) = (\mathbf{A}\cdot\mathbf{C})\mathbf{B} - (\mathbf{A}\cdot\mathbf{B})\mathbf{C} \tag{10}$$

and assumptions (A1) and (A2), we deduce that $(\mathbf{v}\times\mathbf{B})\times\widehat{\mathbf{B}} = -|\mathbf{B}|\mathbf{v}$, therefore from (7a) we get that:

$$\mathbf{v} = \mathbf{v}_d := \tfrac{\mathbf{B}\times\nabla\varphi}{|\mathbf{B}|^2}\,. \tag{11}$$

Here $\mathbf{v}_d$ is the so-called magnetic-drift velocity which, at least in paper, is reached in the cold-plasma zero-electron mass limit. It is responsible for the ‘spinning or spiraling’ nature of currents in the cross-section of conductors, magnetically insulated transmission lines, tokamaks, etc. The drift-velocity is somewhat smooth and does not constitute a major limiting factor of numerical schemes. What is indeed problematic is that the drift-velocity co-exists with the cyclotron and plasma frequencies which induce low-amplitude high-frequency motions superposed on top of the drift-velocities.

Summarizing our findings: under assumptions (A1) and (A2), in the limit of $\theta \to 0^+$ and $m_e \to 0^+$ the solution $[n_e, \mathbf{v}, \varphi]$ of system (6) should coincide with the solution of the limiting

---

[1] ‘Stiff’ pressure waves in the direction of the magnetic field **B** pose a formidable mathematical and numerical challenge. However, even in the cold-plasma limit, the effect of electrostatic plasma oscillations and cyclotron motions are enough to produce catastrophic consequences in many plasma physics codes. Our research plan is to solve and understand one problem at a time. At the time of this writing, we have decided to focus our efforts on the high-frequency electromagnetic phenomena caused by electrostatic plasma-oscillation and cyclotron motion.

system

$$\begin{cases} q_e\partial_t n_e = -q_e \mathrm{div}\,(n_e\mathbf{v}) \\ \varepsilon\Delta\partial_t\varphi = q_e\mathrm{div}\,(n_e\mathbf{v}) \end{cases} \quad \text{where} \quad \mathbf{v} := \tfrac{\mathbf{B}\times\nabla\varphi}{|\mathbf{B}|^2}\,. \tag{12}$$

We see that:

- As written, system (12) is *intentionally redundant*: the evolution of the scalar-valued functions $q_e n_e$ and $-\varepsilon\Delta\varphi$ is identical. This means that either φ or n_e could be eliminated. It is not difficult to realize that if the initial data of (12) satisfies the relationship $-\varepsilon\Delta\varphi = q_e n_e$, then it does for all time. Therefore, we have that $\nabla\varphi = \frac{q_e}{\varepsilon}\nabla(-\Delta)^{-1}n_e$ for all time, which allows us to re-write (12) into a single evolutionary PDE:

  $$\partial_t n_e = -\tfrac{q_e}{\varepsilon}\mathrm{div}\left(n_e\tfrac{\mathbf{B}\times\nabla(-\Delta)^{-1}n_e}{|\mathbf{B}|^2}\right). \tag{13}$$

  Note that $\mathrm{div}\left(n_e\frac{\mathbf{B}\times\nabla(-\Delta)^{-1}n_e}{|\mathbf{B}|^2}\right)$ is a zero-order differential operator. Magnetic drift-limits are usually called 'diffusive-limits', however we may challenge this terminology since (13) does not describe a diffusion in any traditional sense. We may claim that (13) is a non-local ordinary differential equation or zero-order non-local PDE. The PDE-analysis literature has greatly benefited from non-local formulations such as (13), see for instance [42] and [80].

  However, beyond highly specialized audiences, non-local numerical formulations have found limited popularity in the context or large scale production codes. Therefore, some of the of the premises of these notes are: (i) Avoiding by all means non-local formulations such as (13), (ii) Exploiting *redundancy* to our favor in a numerical context. By using the redundant formulation (12) we may be able to recast elliptic constraints (e.g. $-\varepsilon\Delta\varphi = q_e n_e$) as an evolutionary PDEs. Exploiting redundancy and recasting elliptic constraints as an evolutionary process is not a new idea, at the very least, it was advanced in [83] by the authors.

- We have that $\mathrm{div}\left(\frac{\mathbf{B}\times\nabla\varphi}{|\mathbf{B}|^2}\right) = 0$ whenever $\mathrm{curl}\left(\frac{\mathbf{B}}{|\mathbf{B}|^2}\right) = \mathbf{0}$: this follows from identity $\mathrm{div}\,(\mathbf{A}\times\mathbf{C}) = \mathrm{curl}\,\mathbf{A}\cdot\mathbf{C} - \mathrm{curl}\,\mathbf{C}\cdot\mathbf{A}$. In particular, this situation occurs whenever $\mathbf{B} \equiv$ *const.* Or using words: the drift velocity becomes divergence-free in the context of constant magnetic fields. Whether this situation occurs in actual technical applications is somewhat debatable. However, a numerical scheme that is meant to work with absolute generality, in every possible context, should be able to accommodate that situation. By itself, approximating divergence-free or weakly divergence-free velocities is not an impossible task. In fact there are plenty of inf-sup compatible finite element pairs capable of doing so [7]. However, accommodating such constraints may not be trivial if we also want to satisfy other PDE-properties, in particular, pointwise stability properties (e.g. max-min principles and invariant sets, see for instance [53]).

  Hopefully, this observation is enough to convince the reader that even though we are neglecting fast pressure waves associated to (8), approximating the cold-plasma drift-limit of problem (1) is by no means a trivial problem. We mention in passing that short-time existence as well as blow-up of solutions of system (12) when $\mathrm{div}\,\mathbf{v}_d \equiv 0$ has been studied in [4].

- It is worth mentioning that the 2d vorticity formulation of the incompressible Euler equations consist of:

  $$\partial_t \omega + \operatorname{div}(\mathbf{v}\omega) = 0 \text{ and } \Delta\psi = \omega\,, \tag{14}$$

  where

  $$\mathbf{v} := \nabla^{\perp}\psi := \begin{bmatrix} -\partial_y\psi \\ \partial_x\psi \\ 0 \end{bmatrix} = \begin{bmatrix} 0 \\ 0 \\ 1 \end{bmatrix} \times \begin{bmatrix} \partial_x\psi \\ \partial_y\psi \\ 0 \end{bmatrix},$$

  see for instance [68]. Since $\Delta\partial_t\psi = \partial_t\omega$ we can rewrite (14) in *redundant* form

  $$\begin{cases} \partial_t\omega + \operatorname{div}(\mathbf{v}\omega) = 0 \\ \Delta\partial_t\psi + \operatorname{div}(\mathbf{v}\omega) = 0\,. \end{cases} \tag{15}$$

  If we set $\mathbf{B} \equiv [0,0,1]^{\top}$, $\varepsilon = 1$, $q_e = 1$, $n_e := \omega$, and consider the relabeling $\varphi := \psi$ in (12) then: systems (15) and (12) are completely equivalent. We might want to call $\Delta\psi = \omega$ the "vorticity Gauss-law".

- PDE model (12) does NOT exhibit plasma-oscillation or cyclotron frequency. Without inertial effects, such high-frequency phenomena cannot be described by model (12). Model (12) is not a multiscale problem and it only displays transport-like waves.

- The magnetic drift-limit model (12) alone is primarily of academic interest and it might not be immediately apparent how such a limiting model aligns with the broader goal of modeling and simulating fluid models of dense plasmas, which is a cornerstone of the DOE/SNL/NNSA enterprise. To this end we point out that such fluid models may indeed degenerate and operate at regimes very close to those satisfied by the magnetic drift-model (12). The primary goal of this manuscript is thus to advance and and develop numerical schemes for fluid-plasma models that can operate close the stated drift regime without suffering severe degradation of time-step size, loss of positivity and/or invariant-set properties, while also preserving entropy-dissipation properties.

Finally, we mention that system (12) can be found in the literature under various names, such as: cold-plasma magnetic-drift limit [23], guiding-center drift-limit [74, 75, 16, 35, 89, 86], E×B-drift limit, gyro-fluid drift-limit [27], 2d-striation model [4], and the vorticity-formulation of Euler's equations [68]. In every case, the underlying PDE-model is essentially equivalent. In the next Section we try to find the simplest numerical discretization for formulation (12) that attempts to recover some form of stability.

2.3. Basic properties of the magnetic drift-limit model

In this subsection we discuss schemes for the system (12). We highlight, again, that model described by (12) is meaningless unless we make the assumption $|\mathbf{B}|_{\ell^2} \geq B^{\flat} > 0$.

Proposition 2.1 (Formal stability properties)**.** *Model* (12) *is such that:*

- *The particle number density n_e remains non-negative provided that the initial data is non-negative.*

- *Total electric energy satisfies the following energy balance*

$$\frac{\partial}{\partial t}\Big(\frac{\varepsilon}{2}\int_{\Omega}\|\nabla\varphi\|^2\,\mathrm{d}\boldsymbol{x}\Big) = \int_{\partial\Omega}\varphi\big(\varepsilon\nabla\partial_t\varphi - q_e n_e\tfrac{\mathbf{B}\times\nabla\varphi}{|\mathbf{B}|^2}\big)\cdot\mathrm{n}\,\mathrm{d}\boldsymbol{s}\,. \tag{16}$$

- *Assuming that the initial data satisfies the constraint $-\varepsilon\Delta\varphi = q_e n_e$ at time $t = 0$, and that $\|n_e\|_{L^{6/5}(\Omega)}$ is uniformly bounded for all time, then the total electric energy satisfies the estimate*

$$\varepsilon\|\nabla\varphi\|_{L^2(\Omega)} \lesssim \sup_{t\in[0,t_F]}\|n_e\|_{L^{6/5}(\Omega)} \;\; \forall t\in[0,t_F]. \tag{17}$$

Proof. The fact that the $\partial_t n_e + \mathrm{div}\,(n_e\mathbf{v}) = 0$ preserves the sign of the initial data can be found in several academic references (see for instance [50, Section 3.1]) and we will not discuss it here. In order to prove that relationship (16) holds true we multiply the PDE for the potential in (12) by a smooth test function ω and using integration by parts we get

$$\varepsilon\int_{\Omega}\nabla\partial_t\varphi\cdot\nabla\omega\,\mathrm{d}\boldsymbol{x} - \varepsilon\int_{\partial\Omega}\omega\nabla\partial_t\varphi\cdot\mathrm{n}\,\mathrm{d}\boldsymbol{s} = q_e\int_{\Omega}n_e\mathbf{v}\cdot\nabla\omega\,\mathrm{d}\boldsymbol{x} - q_e\int_{\partial\Omega}\omega n_e\mathbf{v}\cdot\mathrm{n}\,\mathrm{d}\boldsymbol{s}\,. \tag{18}$$

Now, using expression (11) for the velocity $\mathbf{v}$, and setting $\omega\equiv\varphi$ we get

$$\frac{\partial}{\partial t}\Big(\frac{\varepsilon}{2}\int_{\Omega}|\nabla\varphi|^2\,\mathrm{d}\boldsymbol{x}\Big) - \varepsilon\int_{\partial\Omega}\varphi\nabla\partial_t\varphi\cdot\mathrm{n}\,\mathrm{d}\boldsymbol{s} = \underbrace{q_e\int_{\Omega}n_e\frac{\mathbf{B}\times\nabla\varphi}{|\mathbf{B}|^2}\cdot\nabla\varphi\,\mathrm{d}\boldsymbol{x}}_{=0} - q_e\int_{\partial\Omega}\varphi n_e\big(\tfrac{\mathbf{B}\times\nabla\varphi}{|\mathbf{B}|^2}\big)\cdot\mathrm{n}\,\mathrm{d}\boldsymbol{s}\,. \tag{19}$$

The remaining steps are just a matter of reorganization. Finally, estimate (17) is just a direct consequence of the Gauss-law $-\varepsilon\Delta\varphi = q_e n_e$, which leads to the energy-identity $\varepsilon\|\nabla\varphi\|^2_{L^2(\Omega)} = q_e\langle n_e,\varphi\rangle$. Assuming boundedness of $\langle n_e,\cdot\rangle$ in dual-norm leads to the requirement $n_e\in L^p(\Omega)$ with $p\geq 6/5$ which is a consequence of well-known Sobolev embedding theorems (see for instance [33, Ch. 5]). □

In this context, (16) and (17) are structural properties of the magnetic-drift-limit system (12). They are the template of properties we might want to preserve at the discrete level. In the following section we propose a scheme that attempts to strike a balance between property preservation and practical implementability.

3. A NUMERICAL SCHEME FOR THE DRIFT-LIMIT MODEL.

Let $\mathbf{u}^n = [n_e^n, \Delta\varphi^n]$ be the initial data for system (12), we consider the splitting $\partial_t\mathbf{u} = \mathcal{A}\mathbf{u} + \mathcal{B}\mathbf{u}$ with the operators $\mathcal{A}$ and $\mathcal{B}$ defined as

$$\partial_t\begin{bmatrix} n_e \\ \varepsilon\Delta\varphi\end{bmatrix} = \underbrace{\begin{bmatrix} -\mathrm{div}\,(\mathbf{v}_d\Box) & 0 \\ 0 & 0\end{bmatrix}}_{:=\mathcal{A}}\begin{bmatrix} n_e \\ \Delta\varphi\end{bmatrix} + \underbrace{\begin{bmatrix} 0 & 0 \\ 0 & q_e\mathrm{div}\,(n_e\frac{\mathbf{B}(t)\times\nabla\Delta^{-1}\Box}{|\mathbf{B}(t)|^2})\end{bmatrix}}_{:=\mathcal{B}}\begin{bmatrix} n_e \\ \Delta\varphi\end{bmatrix}.$$

Using this splitting, we define a formally-second order accurate time-integration scheme Algorithm 1.

Algorithm 1 `strang_one_time_step(`$\{n_e^n, \varphi^n, \mathbf{B}(t)\}$`)`

- ◇ **Stage #1:** compute $n_e^{n+\frac{1}{2}}$, solution of $\partial_t n_e + \operatorname{div}(n_e \mathbf{v}) = 0$, from initial time t^n to $t^{n+\frac{1}{2}} := t^n + \frac{1}{2}\tau$, where $\mathbf{v} = \frac{\mathbf{B}(t)\times\nabla\varphi^n}{|\mathbf{B}(t)|^2}$, with initial data given by n_e^n. Note: the potential φ^n does not evolve in this stage.
- ◇ **Stage #2:** find φ^{n+1}, solution of the following non-symmetric elliptic problem

$$-\varepsilon(\Delta\varphi^{n+1} - \Delta\varphi^n) + q_e \tau \operatorname{div}\left(n_e^{n+\frac{1}{2}} \frac{\mathbf{B}^{n+\frac{1}{2}} \times \nabla\varphi_h^{n+\frac{1}{2}}}{|\mathbf{B}^{n+\frac{1}{2}}|^2} \right) = 0\,, \tag{20}$$

  where $\varphi^{n+\frac{1}{2}} := \frac{1}{2}(\varphi^{n+1} + \varphi^n)$. Note: the density $n_e^{n+\frac{1}{2}}$, does not evolve in this stage.
- ◇ **Stage #3:** compute n_e^{n+1}, solution of $\partial_t n_e + \operatorname{div}(n_e \mathbf{v}) = 0$ from initial time $t^{n+\frac{1}{2}}$ to $t^{n+1} := t^n + \tau$ where $\mathbf{v} = \frac{\mathbf{B}(t)\times\nabla\varphi^{n+1}}{|\mathbf{B}(t)|^2}$ with initial data given by $n_e^{n+\frac{1}{2}}$. Note: the potential φ^{n+1} does not evolve in this stage.

Return: $\{n_e^{n+1}, \varphi^{n+1}\}$

Remark 3.1 (Stability of Stage #2)**.** The Stage #2 of the scheme described in Algorithm 1 respects the boundedness of the total electric energy, more precisely, we have that:

$$\varepsilon\|\nabla\varphi^{n+1}\|^2_{L^2(\Omega)} = \varepsilon\|\nabla\varphi^n\|^2_{L^2(\Omega)} + \text{Boundary Terms}\,, \tag{21}$$

which follows by multiplying (20) by a test function ω and integration by parts,

$$\varepsilon\int_\Omega \nabla\widetilde{\varphi}^{n+1}\cdot\nabla\omega\,\mathrm{d}\boldsymbol{x} - \tau q_e \underbrace{\int_\Omega n_e^{n+\frac{1}{2}} \left(\frac{\mathbf{B}^{n+\frac{1}{2}}\times\nabla\varphi^{n+\frac{1}{2}}}{|\mathbf{B}^{n+\frac{1}{2}}|^2}\right)\cdot\nabla\omega\,\mathrm{d}\boldsymbol{x}}_{\text{skew-symmetric term}} = \varepsilon\int_\Omega \nabla\varphi^n\cdot\nabla\omega\,\mathrm{d}\boldsymbol{x}\,, \tag{22}$$

and taking $\omega := \varphi^{n+\frac{1}{2}}$. Up to boundary terms, (21) mimics the time-continuous PDE property (16).

Remark 3.2 (Gauss-law violation)**.** In principle, Marchuk-Strang splitting scheme is formally second-order accurate. The expectation is that, Algorithm 1 will return a pair n_e^{n+1} and φ^{n+1} satisfying a formal error estimate:

$$\varepsilon\|\nabla\varphi(t^{n+1}) - \nabla\varphi^{n+1}\|_{L^2(\Omega)} + q_e\|n_e(t^{n+1}) - n_e^{n+1}\|_{L^2(\Omega)} \le \mathcal{O}(\tau^q)\,,$$

for some $q \le 2$, where $\varphi(t^{n+1})$ and $n_e(t^{n+1})$ represent the exact solutions, while φ^{n+1} and n_e^{n+1} represent the solutions returned by Algorithm 1. However, there is absolutely no good reason to expect that the Gauss-law is respected exactly. Meaning that, in general, the property $-\varepsilon\Delta\varphi^{n+1} = q_e n_e^{n+1} \in H^{-1}(\Omega)$ will not be satisfied. The purpose of this project was not the development of techniques in order to preserve/recover preservation of the Gauss-law. However, we needed to introduce a mechanism in order to evaluate the sensitivity and robustness of the numerical scheme described by Algorithm 1 with respect to the preservation (or violation) of the Gauss-law. In Appendix B we describe a simple procedure and prove that it is necessarily benign: that is, it cannot reduce the order of convergence of the scheme. The actual scheme that we would use in practice would follow the steps described in Algorithm 2.

Algorithm 2 `strang_with_restart`$(\{n_e^n, \varphi^n, \mathbf{B}(t)\})$

```
    $\{n_e^{n+1}, \varphi^{n+1}\}$ := strang_one_time_step($\{n_e^n, \varphi^n, \mathbf{B}(t)\}$
    $\kappa := \|\nabla\varphi^{n+1}\|$
    $\widehat{\varphi}^{n+1}$ := line_search_gauss_law_restart( $\{n_e^{n+1}, n_b^{n+1}, \varphi^{n+1}, \kappa\}$
Return: $\{n_e^{n+1}, \widehat{\varphi}^{n+1}\}$
```

4. NUMERICAL SCHEMES FOR THE EULER-POISSON SYSTEM WITH GIVEN MAGNETIC FIELD

4.1. Semi-implicit splitting of variables

In this section we follow the same line of thought introduced in Section 2.2 of [83]. The simplest approach to solve the system of equations (1) consists in considering two asymptotic regimes. In one of such regimes, the source terms are assumed to negligible. We will call it the hyperbolic-dominated regime:

$$\partial_t\rho + \operatorname{div}\mathbf{p} = 0\,, \tag{23a}$$
$$\partial_t\mathbf{p} + \operatorname{div}(\rho^{-1}\mathbf{p}\mathbf{p}^\top + \mathbb{I}p) = \mathbf{0}\,, \tag{23b}$$
$$-\varepsilon\Delta\partial_t\varphi = \mathbf{0}\,. \tag{23c}$$

We consider a second regime, where source terms dominate the dynamics and hyperbolic terms are negligible

$$\partial_t\rho = 0\,, \tag{24a}$$
$$\partial_t\mathbf{p} = -\tfrac{q_e}{m_e}\rho\nabla\varphi + \tfrac{q_e}{m_e}\mathbf{p}\times\mathbf{B} - \tfrac{1}{\mathscr{T}}\mathbf{p}\,, \tag{24b}$$
$$-\varepsilon\Delta\partial_t\varphi = -\tfrac{q_e}{m_e}\operatorname{div}\mathbf{p}\,, \tag{24c}$$

This structure lends itself naturally to the idea of using operator-splitting in time. The first-order scheme in this context is usually known as Yanenko operator splitting:

Algorithm 3 `yanenko_one_time_step`($\{\rho^n, \mathbf{p}^n, \varphi^n\}$)

- **Stage #1:** given the initial data $[\rho^n, \mathbf{p}^n]^\top$, compute $[\rho^{n+1}, \mathbf{p}^{n+\frac{1}{2}}]^\top$, solution of the hyperbolic system (23), from initial time t^n to $t^{n+1} := t^n + \tau$ (full time-step increment). Note that the electric potential does not evolve in this Stage #1, and that the density ρ^{n+1} computed in this stage is the final density returned by the Yanenko splitting scheme.
- **Stage #2:** given the data $[\rho^{n+1}, \mathbf{p}^{n+\frac{1}{2}}, \varphi^n]^\top$, compute $[\mathbf{p}^{n+1}, \varphi^{n+1}]^\top$, solution of the coupled source-system (24b)-(24c), from initial time t^n to $t^{n+1} := t^n + \tau$ (full time-step increment). Note that ρ^{n+1} does not evolve in this Stage #1.

Return: $\{\rho^{n+1}, \mathbf{p}^{n+1}, \varphi^{n+1}\}$

The second-order of operator splitting is called Marchuk-Strang splitting:

Algorithm 4 `strang_one_time_step`($\{\rho^n, \mathbf{p}^n, \varphi^n\}$)

- **Stage #1:** given the initial data $[\rho^n, \mathbf{p}^n]^\top$, compute $[\rho^{n+\frac{1}{2}}, \mathbf{p}^{n+\frac{1}{2}}]^\top$, solution of the hyperbolic system (23), from initial time t^n to $t^{n+\frac{1}{2}} := t^n + \frac{1}{2}\tau$ (half time-step increment). Note that the electric potential does not evolve in this Stage #1.
- **Stage #2:** given the data $[\rho^{n+\frac{1}{2}}, \mathbf{p}^{n+\frac{1}{2}}, \varphi^n]^\top$, compute $[\widetilde{\mathbf{p}}^{n+1}, \varphi^{n+1}]^\top$, solution of the coupled source-system (24b)-(24c), from initial time t^n to $t^{n+1} := t^n + \tau$ (full time-step increment). Note that $\rho^{n+\frac{1}{2}}$ does not evolve in this Stage #1.
- **Stage #3:** given the data $[\rho^{n+\frac{1}{2}}, \widetilde{\mathbf{p}}^{n+1}]^\top$, compute $[\rho^{n+1}, \mathbf{p}^{n+1}]^\top$, solution of the hyperbolic system (23), from initial time t^n to $t^{n+\frac{1}{2}} := t^n + \frac{1}{2}\tau$ (half time-step increment). Note that the electric potential does not evolve in this Stage #1.

Return: $\{\rho^{n+1}, \mathbf{p}^{n+1}, \varphi^{n+1}\}$

In practice, Yanenko splitting is rarely ever used. In fact we never implemented it. All the computations in presented in this manuscript use Marchuk-Strang splitting as described in Algorithm 4. However, Yanenko splitting is very useful as a pedagogical resource. The presentation of some mathematical results is greatly benefited by considering the Yanenko splitting, with such results becoming immediately true for the case of Marchuk-Strang splitting too, see Section 5.

We note that the scheme described by Algorithm 4 leaves open pretty much all choices regarding space and time discretization. Operator-splitting, and generally speaking semi-implicit time integration, by itself, does not describe a scheme, but rather a loose collection of ideas. For instance, the choice of explicit-implicit splitting is rarely even unique: some choices of splitting lead to a stable scheme but other choices may not. In Algorithm 4, the choice of splitting is quite clear, which is outlined by (23) and (24). Similarly, the choice of space and time discretization for each stage will in general have a profound effect on the mathematical properties of the resulting scheme, in particular, it will affect the well-posedness of the resulting linear algebra system and energy-stability properties, see for instance [83, 48]. This is why designing an Operator-Splitting scheme that indeed preserves relevant mathematical properties is a quite technical task while improvised used of operator splitting is rarely ever a productive enterprise.

The numerical scheme for the hyperbolic subsystem (23) is a graph-based invariant domain preserving schemes described in [53, 66]. Some of the key ideas of invariant domain preserving schemes are summarized in Appendix C and shall not discussed them in this manuscript any further. In Section 4.2 we provide a precise description of the space and time discretization for the source-system (24b)-(24c). In Section 4.3 we provide three choices for the source-update scheme, and we discuss their actual implementation in Section 4.4.

4.2. Space discretization

We assume that we have at hand a mesh $\mathcal{T}_h$ consisting of a set of quadrilateral elements, to be denoted as K. For the sake of concreteness we assume that the potential is discretized using continuous Lagrangian first-order quadrilateral space $\mathbb{H}$, more precisely,

$$\mathbb{H} = \left\{ \omega_h \in \mathcal{C}^0(\Omega) \;\middle|\; \omega_h \circ \boldsymbol{T}_K \in \mathbb{Q}^1(\widehat{K}) \; \forall K \in \mathcal{T}_h \right\}. \tag{25}$$

Here, $\boldsymbol{T}_K : \widehat{K} \to K$ denotes a diffeomorphism mapping the reference element $\widehat{K}$ to the physical element $K \in \mathcal{T}_h$. For each component of the hyperbolic system we use scalar-valued Lagrangian first-order discontinuous finite element space $\mathbb{V}$, as described by

$$\mathbb{V} = \left\{ z_h \in L^2(\Omega) \;\middle|\; z_h \circ \boldsymbol{T}_K \in \mathbb{Q}^1(\widehat{K}) \; \forall K \in \mathcal{T}_h \right\}. \tag{26}$$

We assume that we have at hand a basis for the finite element space $\mathbb{H}$ denoted as $\{\chi_i\}_{i\in\mathcal{V}_P}$, where $\mathcal{V}_P$ denotes the set of indices for the shape functions. Similarly, we assume that we have at hand a basis for the finite element space $\{\phi_i\}_{i\in\mathcal{V}_H}$, where $\mathcal{V}_H$ denotes the corresponding set of indices for the shape functions. Since we use Lagrange finite elements, $\mathcal{V}_H$ can also be used to identify the set of interpolation points $\{\boldsymbol{x}_i\}_{i\in\mathcal{V}_H}$ of the finite element space $\mathbb{V}$. The finite element space for the velocity and/or momentum will be denoted as $\mathbf{V} := [\mathbb{V}]^d$ with vector-valued finite element basis given by $\{\boldsymbol{\phi}_i\}_{i\in\mathcal{V}_V}$ where $\mathcal{V}_V$ is the corresponding set of indices of shape functions.

In the previous paragraph we defined the global sets of indices $\mathcal{V}_P$, $\mathcal{V}_H$, and $\mathcal{V}_V$. In this manuscript we will find situations where we are only concerned with a subset of such indices. In particular, for a given element $K \in \mathcal{T}_h$, we will be interested only on the indices of shape functions with support in such cell. For this reason we also define the following notation describing subsets:

$$\begin{aligned}
\mathcal{V}_P(K) &= \{ j \in \mathcal{V}_P \,|\, \mathrm{supp}(\chi_j) \cap K \not\equiv \emptyset \}, \\
\mathcal{V}_H(K) &= \{ j \in \mathcal{V}_H \,|\, \mathrm{supp}(\phi_j) \cap K \not\equiv \emptyset \}, \\
\mathcal{V}_V(K) &= \{ j \in \mathcal{V}_V \,|\, \mathrm{supp}(\boldsymbol{\phi}_j) \cap K \not\equiv \emptyset \}.
\end{aligned} \tag{27}$$

Remark 4.1. For all finite element spaces the basis functions are generated using the reference-to-physical map $\boldsymbol{T}_K$. That is, Lagrangian shape functions are defined in the reference element satisfying the property $\widehat{\phi}_k(\widehat{\boldsymbol{x}}_j) = \delta_{jk}$ where $\{\widehat{\boldsymbol{x}}_k\}_{k\in\mathcal{N}}$ are the coordinates of the interpolation nodes in the reference element, and $\mathcal{N}$ denotes the set of integers used to identify such nodes (e.g. $\mathcal{N} = \{1 : 4\}$ for $\mathbb{Q}^1(\widehat{K})$ elements in 2d). In each physical element K, the shape functions can be defined using a local indexation $\phi_{K,k}(\boldsymbol{x}) := \widehat{\phi}_k(\boldsymbol{T}_K^{-1}(\boldsymbol{x}))$ for all $k \in \mathcal{N}$.

Let $\mathcal{C}^0(\mathcal{T}_h)$ denote the space of scalar-valued piecewise continuous functions on the triangulation, that is: functions with well-defined point-values on each element. Similarly we define the space of piecewise continuous vector-valued functions as $[\mathcal{C}^0(\mathcal{T}_h)]^d$. Let $f, g \in \mathcal{C}^0(\mathcal{T}_h)$: we define the bilinear form $\langle f, g\rangle : \mathcal{C}^0(\mathcal{T}_h) \times \mathcal{C}^0(\mathcal{T}_h) \to \mathbb{R}$ as follows:

$$\langle f, g\rangle := \sum_{K\in\mathcal{T}_h} \sum_{k\in\mathcal{N}} f(\boldsymbol{x}_k) g(\boldsymbol{x}_k) w_{K,k}, \tag{28}$$

where $\boldsymbol{x}_k = \boldsymbol{T}_K(\widehat{\boldsymbol{x}}_k)$ and $w_{K,k} := \int_K \phi_{K,k}(\boldsymbol{x})\,\mathrm{d}\boldsymbol{x}$, and with an obvious extension when $\boldsymbol{f}, \boldsymbol{g} \in [\mathcal{C}^0(\mathcal{T}_h)]^d$. Whenever the bilinear form $\langle\cdot,\cdot\rangle$ is applied to finite dimensional spaces $\mathbb{V}$, $\boldsymbol{\mathbb{V}}$, $\mathbb{H}$, or $\nabla\mathbb{H}$ we will call it a lumped inner-product. Such inner-product is second-order accurate in the context of affine or asymptotically-affine mesh-sequences but may fail to be second-order accurate in distorted non-nested mesh-sequences.

4.3. Fully-discrete source-update schemes

In this section we describe three possible schemes for the discretization of (24b)-(24c): Backward-Euler, Crank-Nicolson, and the Crouzeix's DIKR23 scheme. Let us start by writing down a semi-discrete Backward-Euler scheme:

$$\begin{aligned}
\rho^n\mathbf{v}^{n+1} - \rho^n\mathbf{v}^n &= -\tfrac{\tau q_e}{m_e}\rho^n\nabla\varphi^{n+1} + \tfrac{\tau q_e}{m_e}\rho^n\mathbf{v}^{n+1}\times\mathbf{B} - \tfrac{\tau}{\mathscr{T}}\rho^n\mathbf{v}^{n+1}, \\
-\varepsilon(\Delta\varphi^{n+1} - \Delta\varphi^n) &= -\tfrac{\tau q_e}{m_e}\mathrm{div}\,(\rho^n\mathbf{v}^{n+1}) + \tfrac{\tau q_b}{m_b}\partial_t\rho_b(t^{n+1}),
\end{aligned}$$

where q_b is the specific electric charge of the background density, m_b is the specific mass, and $\partial_t\rho_b$ is the time derivative of the background mass-density ρ_b. We assume that both ρ_b and $\partial_t\rho_b$ are given data. The corresponding weak formulation is:

$$(\rho^n\mathbf{v}^{n+1} - \rho^n\mathbf{v}^n, \mathbf{z}) = -\tfrac{\tau q_e}{m_e}(\rho^n\nabla\varphi^{n+1}, \mathbf{z}) + \tfrac{q_e}{m_e}(\rho^n\mathbf{v}^{n+1}\times\mathbf{B}, \mathbf{z}) - \tfrac{1}{\mathscr{T}}\rho^n\mathbf{v}^{n+1}, \mathbf{z}), \tag{29}$$

$$(\nabla\varphi^{n+1} - \nabla\varphi^n, \nabla\omega) = \tfrac{q_e}{m_e}(\rho^n\mathbf{v}^{n+1}, \nabla\omega) + \tfrac{\tau q_b}{m_b}(\partial_t\rho_b(t^{n+1}), \omega), \tag{30}$$

for all $\mathbf{z}$ and ω in some proper test space. For the time-being, (29)-(30) represent the weak formulation of a semi discretization. In order to incorporate a space discretization we assume that $\varphi_h^{n+1} = \sum_{j\in\mathcal{V}_P}\Phi_j\chi_j \in \mathbb{H}$ and that $\mathbf{v}_h^{n+1} = \sum_{j\in\mathcal{V}_V}\mathbf{V}_j\boldsymbol{\phi}_j \in \boldsymbol{\mathbb{V}}$, which leads to the following fully-discrete formulation (we ignore boundary conditions in order to provide a cleaner presentation):

$$\langle\rho_h^n\mathbf{v}_h^{n+1} - \rho_h^n\mathbf{v}_h^n, \mathbf{z}_h\rangle = -\tfrac{\tau q_e}{m_e}(\rho_h^n\nabla\varphi_h^{n+1}, \mathbf{z}_h) + \tfrac{q_e}{m_e}(\rho_h^n\mathbf{v}_h^{n+1}\times\mathbf{B}, \mathbf{z}_h) - \tfrac{1}{\mathscr{T}}(\rho_h^n\mathbf{v}_h^{n+1}, \mathbf{z}_h), \tag{31}$$

$$(\nabla\varphi^{n+1} - \nabla\varphi^n, \nabla\omega_h) = \tfrac{q_e}{m_e}(\rho_h^n\mathbf{v}_h^{n+1}, \nabla\omega_h) + \tfrac{\tau q_b}{m_b}(\partial_t\rho_b(t^{n+1}), \omega_h), \tag{32}$$

for all $\mathbf{z}_h \in \boldsymbol{\mathbb{V}}$ and all $\omega_h \in \mathbb{H}$.

Proposition 4.1 (Energy-Stability)**.** *Note that for the sake of simplicity we neglect the effect of background charges and damping. The source-update scheme* (31)-(32) *satisfies the following energy-identity*

$$\sum_{i\in\mathcal{V}_H} \tfrac{m_i}{2}\tfrac{|\mathbf{p}_i^{n+1}|^2}{\rho_i^n} + \tfrac{\varepsilon}{2}\|\nabla\varphi_h^{n+1}\|_{L^2(\Omega)}^2 + Q(\mathbf{u}_h^n,\mathbf{u}_h^{n+1}) = \sum_{i\in\mathcal{V}_H} \tfrac{m_i}{2}\tfrac{|\mathbf{p}_i^{n}|^2}{\rho_i^n} + \tfrac{\varepsilon}{2}\|\nabla\varphi_h^{n}\|_{L^2(\Omega)}^2$$

where $\mathbf{u}_h^n = [\mathbf{p}_h^n, \varphi_h^n]^\top$*,* $\mathbf{u}_h^{n+1} = [\mathbf{p}_h^{n+1}, \varphi_h^{n+1}]^\top$ *and*

$$Q(\mathbf{u}_h^n,\mathbf{u}_h^{n+1}) := \sum_{i\in\mathcal{V}_H} \tfrac{m_i}{2}\tfrac{|\mathbf{p}_i^{n+1}-\mathbf{p}_i^n|^2}{\rho_i^n} + \tfrac{\varepsilon}{2}\|\nabla\varphi_h^{n+1}-\nabla\varphi_h^n\|_{L^2(\Omega)}^2\,, \tag{33}$$

is the artificial-dissipation term associated to Backward-Euler.

Proof. The proof is pretty standard and follows by taking $\mathbf{z}_h = \mathbf{v}_h^{n+1}$ in (31) and $\omega_h = \varphi_h^{n+1}$ in (32). The rest is a consequence of the polarization identity $(a-b,a) = \frac{1}{2}|a|^2 - \frac{1}{2}|b|^2 + \frac{1}{2}|a-b|^2$. □

We also consider the θ-scheme:

$$\begin{aligned}
\langle \rho_h^n\mathbf{v}_h^{n+1} - \rho_h^n\mathbf{v}_h^n, \mathbf{z}_h\rangle &= -\tfrac{\tau q_e}{2m_e}(\rho_h^n((1-\theta)\nabla\varphi_h^n + \theta\nabla\varphi_h^{n+1}), \mathbf{z}_h) \\
&\quad + \tfrac{q_e}{2m_e}(\rho_h^n((1-\theta)\mathbf{v}_h^n + \theta\mathbf{v}_h^{n+1}) \times \mathbf{B}, \mathbf{z}_h) \\
&\quad - \tfrac{1}{2\mathscr{T}}(\rho_h^n((1-\theta)\mathbf{v}_h^n + \theta\mathbf{v}_h^{n+1}), \mathbf{z}_h),
\end{aligned} \tag{34}$$

$$(\nabla\varphi^{n+1} - \nabla\varphi^n, \nabla\omega_h) = \tfrac{q_e}{2m_e}(\rho_h^n((1-\theta)\mathbf{v}_h^n + \theta\mathbf{v}_h^{n+1}, \nabla\omega_h) + \tfrac{\tau q_b}{m_b}(\partial_t\rho_b(t^{n+\theta}), \omega_h)\,, \tag{35}$$

where $\theta \in [\frac{1}{2}, 1]$ and $t^{n+\theta} = t^n + \theta\tau$. As it is well known the case of $\theta = 1$ corresponds with Backward-Euler, while the case $\theta = \frac{1}{2}$ is known as Crank-Nicolson.

Proposition 4.2. *Note that for the sake of simplicity we neglect the effect of background charges and damping. The source-update scheme* (34)-(35)*, with* $\theta = \frac{1}{2}$ *satisfies the following energy-identity*

$$\sum_{i\in\mathcal{V}_H} \tfrac{m_i}{2}\tfrac{|\mathbf{p}_i^{n+1}|^2}{\rho_i^n} + \tfrac{\varepsilon}{2}\|\nabla\varphi_h^{n+1}\|_{L^2(\Omega)}^2 , = \sum_{i\in\mathcal{V}_H} \tfrac{m_i}{2}\tfrac{|\mathbf{p}_i^{n}|^2}{\rho_i^n} + \tfrac{\varepsilon}{2}\|\nabla\varphi_h^{n}\|_{L^2(\Omega)}^2 \,.$$

The proof of this stability property is pretty standard and follows by taking $\mathbf{z}_h = \frac{1}{2}(\mathbf{v}_h^n + \mathbf{v}_h^{n+1})$ in (34) and $\omega_h = \frac{1}{2}(\varphi_h^n + \varphi_h^{n+1})$ in (35). We note that Crank-Nicolson has no artificial dissipation. In the absence of resistive effects, we note that (24b)-(24c) preserves quadratic invariants. Therefore Crank-Nicolson's scheme is, perhaps, the most natural choice of source-update scheme. In addition, in our previous work pertaining the Euler-Poisson system without magnetic fields, see [83], Crank-Nicolson's scheme showed very promising results in the context of the shock-hydrodynamics regime. However, as we will see later in Section 6.4, this time integration scheme does not appear to have the right properties that enable neither efficient nor accurate solution for the new problem at hand.

Finally, we consider Crouzeix's DIRK23 scheme. In Appendix A we describe the Crouzeix DIRK23 scheme in a very general setting: we explain how it is implemented in practice (see

Remark A.1), and describe the energy-stability property satisfied by any evolutionary problem within the Gelfand-triple Hilbert-space framework (see Lemma A.1). From a practical point of view, Crouzeix's scheme is a two-stage method: Stages #1 and #2, as described in (69) and (70), are computed using Backward-Euler's method, and the final solution is computed as a linear extrapolation/combination, as described in (71). The scheme is straightforward to implement provided we have an implementation of a Backward-Euler method at hand. In this manuscript we implemented DIRK23 scheme using the fully discrete implementation of Backward-Euler method described by (31)-(32). The following corollary is just a direct consequence of Lemma A.1 and the specific structure of the Backward-Euler scheme (31)-(32).

Proposition 4.3 (DIRK23 scheme energy-identity)**.** *Note: the sake of simplicity, we neglect the effect of background charges, and damping. The final solution of DIRK23 scheme, with Stages #1 and #2 computed using Backward-Euler's implementation* (24b)-(24c)*, satisfies the following stability estimate:*

$$\sum_{i\in\mathcal{V}_H} \frac{m_i}{2}\frac{|\mathbf{p}_i^{n+1}|^2}{\rho_i^n} + \frac{\varepsilon}{2}\|\nabla\varphi_h^{n+1}\|^2_{L^2(\Omega)} + \mathcal{Q}(\mathbf{u}_h^n,\mathbf{u}_h^1,\mathbf{u}_h^2) = \sum_{i\in\mathcal{V}_H} \frac{m_i}{2}\frac{|\mathbf{p}_i^n|^2}{\rho_i^n} + \frac{\varepsilon}{2}\|\nabla\varphi_h^n\|^2_{L^2(\Omega)}$$

where $\mathbf{u}_h^n = [\mathbf{p}_h^n, \varphi_h^n]^\top$ *is the initial state, while* $\mathbf{u}_h^1 = [\mathbf{p}_h^1, \varphi_h^1]^\top$ *denotes the solution from the Stage #1,* $\mathbf{u}_h^2 = [\mathbf{p}_h^2, \varphi_h^2]^\top$ *denotes the solution from the Stage #2, and* $\mathcal{Q}(\mathbf{u}_h^n,\mathbf{u}_h^1,\mathbf{u}_h^2)$ *is a positive semi-definite homogeneous of degree-2 quadratic form given by*

$$\begin{aligned}\mathcal{Q}(\mathbf{u}_h^n,\mathbf{u}_h^1,\mathbf{u}_h^2) := \sum_{i\in\mathcal{V}_H} m_i \Big[\delta_1 \frac{|\mathbf{p}_i^1-\mathbf{p}_i^n|^2}{\rho_i^n} + \delta_2 \frac{|\mathbf{p}_i^2-\mathbf{p}_i^1|^2}{\rho_i^n} + \delta_{12}(\mathbf{p}_i^1-\mathbf{p}_i^n)\cdot(\mathbf{p}_i^2-\mathbf{p}_i^1)\Big] \\ + \varepsilon\delta_1\|\nabla\varphi_h^1-\nabla\varphi_h^n\|_{L^2(\Omega)} + \varepsilon\delta_2\|\nabla\varphi_h^2-\nabla\varphi_h^1\|_{L^2(\Omega)} \\ + \varepsilon\delta_{12}(\nabla\varphi_h^1-\nabla\varphi_h^n, \nabla\varphi_h^2-\nabla\varphi_h^1)_{L^2(\Omega)}\end{aligned} \tag{36}$$

is the artificial-dissipation term of Crouzeix's DIRK23 scheme, with δ_1*,* δ_2 *and* δ_{12} *as defined in* (74).

Here, we highlight that the quadratic form $\mathcal{Q}(\mathbf{u}_h^n,\mathbf{u}_h^1,\mathbf{u}_h^2)$, defined in (36), represents so-called 'high-frequency artificial damping', meaning that, it introduces a very subtle form of dissipation on high order moments (e.g. high-order divided-differences) of the solution. This is very different from the artificial damping introduced by Backward-Euler that penalizes the first order divided differences of the solution. We may think of $\mathcal{Q}(\mathbf{u}_h^n,\mathbf{u}_h^1,\mathbf{u}_h^2)$ as 'high-frequency filter', but rather than using ad-hoc filter, we use a filter that is already built-in to the scheme that is capable of regularizing high-frequencies while also providing mathematically guaranteed energy-stability.

4.4. Efficient assembly/implementation

In this section explain how to implement an efficient assembly of the schemes described by (31)-(32), (34)-(35), and DIRK23 scheme. With a proper assembly strategy the linear problems that we have to solve a each time-step are not that different from a scalar Poisson problem. We explain the primary idea using Backward-Euler's scheme. We also summarize the respective assembly for the case of the θ-scheme in Remark 4.5.

The standard practice, is to break down the assembly into element contributions and add them into a single large sparse matrix. Let us consider the case of Backward-Euler scheme as described by (31)-(32):

- The assembly corresponding to the space discretization of the potential (32) will invoke the following loop on all cells:

$$\begin{aligned}\sum_{K\in\mathcal{T}_h}\sum_{j\in\mathcal{V}_P(K)}\Phi_j^{n+1}\Big[\varepsilon(\nabla\chi_j,\nabla\chi_i)_K\Big]+\sum_{K\in\mathcal{T}_h}\sum_{j\in\mathcal{V}_V(K)}\mathbf{V}_j\Big[-\tfrac{\tau q_e}{m_e}(\rho_e\boldsymbol{\phi}_j,\nabla\chi_i)_K\Big]=\\ =\sum_{K\in\mathcal{T}_h}\sum_{j\in\mathcal{V}_P(K)}\Phi_j^n\,\Big[\varepsilon(\nabla\varphi^n,\nabla\chi_i)_K\Big]+\tfrac{\tau q_b}{m_b}(\partial_t\rho_b(t^{n+1}),\chi_i)_K\end{aligned} \tag{37}$$

  where the index-sets $\mathcal{V}_P(K)$ and $\mathcal{V}_V(K)$ were defined in (27). Expression (37) can be rewritten in terms of element-matrix and element-vector contributions:

$$\sum_{K\in\mathcal{T}_h}\mathcal{K}_K\Phi_K^{n+1}+\mathcal{B}_K\mathbf{V}_K^{n+1}=\sum_{K\in\mathcal{T}_h}\mathcal{K}_K\Phi_K^n+\mathbf{R}_K\,, \tag{38}$$

  where

$$\begin{aligned}\{\mathcal{K}_K\}_{ij}&:=\varepsilon(\nabla\chi_j,\nabla\chi_i)_K\,,\\ \{\mathcal{B}_K\}_{ij}&:=-\tfrac{\tau q_e}{m_e}(\rho_e\boldsymbol{\phi}_j,\nabla\chi_i)_K,\\ \{\mathbf{R}_K\}_i&:=\tfrac{\tau q_b}{m_b}(\partial_t\rho_b(t^{n+1}),\chi_i)_K,\end{aligned} \tag{39}$$

  and Φ_K^{n+1}, $\mathbf{V}_K^{n+1}$, and Φ_K^n represent the vector of local degrees of freedom (DOFs) on the cell K. On the other hand, we have assumed that the time-derivative of the background density $\partial_t\rho_b$ is an analytic function. If that is not the case, we might consider computing $\mathbf{R}_K$ as

$$\{\mathbf{R}_K\}_i=\sum_{j\in\mathcal{V}_H(K)}\mathcal{E}_{ij}\{\partial_t\rho_b(t^{n+1})\}_j\ \ \forall i\in\mathcal{V}_P(K)\ \text{ where }\ \mathcal{E}_{ij}=\tfrac{\tau q_b}{m_b}(\phi_j,\chi_i)_K\,,$$

  where the index-set $\mathcal{V}_H(K)$ was defined in (27).

- Similarly, (31) can be localized and written in compact form as

$$\mathcal{C}_K\Phi_K^{n+1}+(\mathcal{M}_K+\mathcal{D}_K+\mathcal{S}_K^v)\mathbf{V}_K^{n+1}=\mathcal{M}_K\mathbf{V}_K^n\quad\forall K\in\mathcal{T}_h\,, \tag{40}$$

  where $\{\mathcal{C}_K\}_{ij}$, $\{\mathcal{M}_K\}_{ij}$ and $\{\mathcal{S}_K^v\}_{ij}$ and $\{\mathcal{D}_K\}_{ij}$ are matrices associated to each element K defined as

$$\begin{aligned}\{\mathcal{C}_K\}_{ij}&:=\tfrac{\tau q_e}{m_e}(\rho_e\nabla\chi_j,\boldsymbol{\phi}_i)_K\,,\\ \{\mathcal{M}_K\}_{ij}&:=\delta_{ij}\rho_i(\boldsymbol{\phi}_i,1)_K\,,\\ \{\mathcal{D}_K\}_{ij}&:=\tfrac{\tau}{\mathscr{T}}\{\mathcal{M}_K\}_{ij}\,,\\ \{\mathcal{S}_K^v\}_{ij}&:=-\tfrac{\tau q_e}{m_e}(\rho_e\boldsymbol{\phi}_j\times\mathbf{B},\boldsymbol{\phi}_i)_K\,,\end{aligned} \tag{41}$$

  for all $i,j\in\mathcal{V}_V(K)$. We note in passing that $\{\mathcal{M}_K\}_{ij}$ describes a density-weighted lumped mass matrix and that $\mathcal{C}_K=-\mathcal{B}_K^\top$.

We note that, from (40), we can always solve for $\mathbf{V}_K^{n+1}$:

$$\mathbf{V}_K^{n+1} = \mathcal{G}_K \mathcal{M}_K \mathbf{V}_K^{n} - \mathcal{G}_K \mathcal{C}_K \Phi_K^{n+1} \;\text{ with }\; \mathcal{G}_K := \big[(1+\tfrac{\tau}{\mathscr{T}})\mathcal{M}_K + \mathcal{S}_K^{v}.\big]^{-1} \tag{42}$$

Inserting this identity into (38) and reorganizing the terms we get:

$$\sum_{K\in\mathcal{T}_h} \big(\mathcal{K}_K - \mathcal{B}_K \mathcal{G}_K \mathcal{C}_K\big)\Phi_K^{n+1} = \sum_{K\in\mathcal{T}_h} \mathcal{K}_K \Phi_K^{n} - \mathcal{B}_K \mathcal{G}_K \mathcal{M}_K \mathbf{V}_K^{n}\,. \tag{43}$$

In other words: since the local (unknown) velocity DOFs $\mathbf{V}_K^{n+1}$ can be eliminated at 'assembly-time' the right hand side of (43) only depends on data from time-step n. Local elimination of unknowns during assembly is commonly known as static-condensation in the finite element and numerical linear algebra literature, see Remark 4.4 for some background on the topic. We summarize the assembly-loop in the following remark.

Remark 4.2 (Assembly Loop)**.** Expression (43) means that we have to solve the linear algebra system $\mathcal{A}\Phi^{n+1} = \mathbf{F}$ for the potential, where the matrix $\mathcal{A}$ and the vector $\mathbf{F}$ are assembled using the usual gather-scatter loop:

```
Clean matrices/vectors: $\mathcal{A} = 0\,, \mathbf{F} = 0$
for all $K \in \mathcal{T}_h$
  $\rho_K \leftarrow$ gather_from_vector($\rho$)
  $\mathbf{B}_K \leftarrow$ gather_from_vector($\mathbf{B}$)
  Assemble: $\mathcal{K}_K\,,\ \mathcal{B}_K\,,\ \mathcal{C}_K\,,\ \mathcal{M}_K^{v},\ \mathcal{D}_K^{v},\ \mathcal{S}_K^{v}$
  Assign: $\mathcal{G}_K \leftarrow \big[(1+\tfrac{\tau}{\mathscr{T}})\mathcal{M}_K + \mathcal{S}_K^{v})\big]^{-1}$        (44)
  Assign: $\mathcal{A}_K \leftarrow \mathcal{K}_K - \mathcal{B}_K \mathcal{G}_K \mathcal{C}_K$
  Assign: $\mathbf{F}_K \leftarrow \mathcal{K}_K \Phi_K^{n} - \mathcal{B}_K \mathcal{G}_K \mathcal{M}_K \mathbf{V}_K^{n}$
  scatter_into_matrix($\mathcal{A}_K, \mathcal{A}$)
  scatter_into_vector($\mathbf{F}_K, \mathbf{F}$)
end for
```

Once we compute the new potential Φ^{n+1} we can compute the new velocities $\mathbf{V}_K^{n+1}$ at each cell K using (42). We note that the matrix $\mathcal{A}$ resulting the assembly loop (44) will indeed be a Schur complement. However, we highlight the following practical merits:

- *Optimal sparsity-pattern.* This Schur complement will be sparse, in fact, it can be easily shown that the sparsity pattern of the matrix $\mathcal{A}$ is optimal: it will use the exactly the same sparsity pattern required to assemble the Poisson matrix $\mathcal{K}_{ij} = \int_\Omega \nabla\chi_i \cdot \nabla\chi_j \,\mathrm{d}\boldsymbol{x}$. See Remark 4.3 for a concrete example.
- *Simple data-structures, simple linear algebra, and inexpensive matrix-vector products.* We avoided all data-structures and DOF-managers usually associated to mixed-formulations. This allowed us to avoid, among other things, assembly and storage of global block-matrix and block-vectors. Because of this, solution of the linear algebra system associated to the potential will not use or invoke matrix-vector products of block-matrix and block-vector

systems. With proper computational implementation, as detailed in the following paragraph, this leads to a speed-up of up to an order of magnitude.

As an example, let us assume that we use the finite element spaces proposed in (25) and (26) and we want to use blocked DOF-manager and blocked linear-algebra. Then, for the case of $d = 2$, the finite element space $\boldsymbol{\mathbb{V}} := [\mathbb{V}]^d$ used for the momentum/velocity, has eight times more degrees of freedom (DOFs) than the finite element space $\mathbb{H}$ used for the potential. This is because the velocity has two components and, in two space dimensions, discontinuous $\mathbb{Q}^1$ finite element spaces have four times more DOFs than its continuous counterpart. Assuming that the cardinality of the finite element space used for the potential is N, then corresponding blocked-vectors would have approximate size $9N$. On the other hand, the vectors involved in iterative solution of the linear algebra system $\mathcal{A}\Phi^{n+1} = \mathbf{F}$, resulting from the static-condensation Algorithm (44) will have size N. Given that the complexity of matrix-vector products used in Krylov space methods scales like $O(N)$ the solution of the statically-condensed linear algebra systems is guaranteed to be almost one order of magnitude faster than that of the corresponding block-vector system. We hope that this example is enough to convince the reader that statically-condensed elimination of the Schur complement is a very appealing idea.

- *Efficient implementation of Dirichlet boundary conditions.* Since $\mathcal{A}$ is sparse, we have explicit access to it. This means that Dirichlet-like boundary conditions of the potential can be enforced directly into $\mathcal{A}$ either during its assembly or once the assembly is done. This is in general, not true for arbitrary mixed formulations where modifications of the block off-diagonal terms is required before actually using the Schur-complement action[2] in order to solve the linear system.
- *Matrix-free ready.* We note in passing that the assembly loop (44) is readily compatible with matrix-free iterative solution strategies, see for instance [64] and references therein.

Remark 4.3 (Dimensionality example)**.** With the choice of finite element spaces proposed in (25) and (26), in two space dimensions we have that the element-matrices will have the following dimensionality:

$$\mathcal{K}_K \in \mathbb{R}^{4\times 4};\ \mathcal{B}_K \in \mathbb{R}^{4\times 8};\ \mathcal{C}_K \in \mathbb{R}^{8\times 4};\ \mathcal{M}_K, \mathcal{S}_K^{v}, \mathcal{G}_K \in \mathbb{R}^{8\times 8},$$

and

$$\Phi_K^n, \Phi_K^{n+1} \in \mathbb{R}^4 \text{ and } \mathbf{V}_K^n, \mathbf{V}_K^{n+1} \in \mathbb{R}^8,$$

which shows that scattering the entries of the matrix $\mathcal{A}_K$, as defined in the pseudo-code, uses the same non-zero entries required to scatter the local matrix $\mathcal{K}_K$.

Remark 4.4 (Static-condensation for PDE-ODE coupling)**.** We highlight that static condensation is a fairly old idea, which is well-known in the context of finite elements and mixed formulations, see for instance [85, 17, 31] and references therein. However, we point-out that here, we are making use of it in a non-standard context.

---

[2] In practice Schur complements are rarely ever sparse. Therefore it's not possible to construct then, store them, or even read its individual entries. But none of that is necessary. Usually, we only need have the capability to compute matrix vector products.

Let us start by noting that (24b)-(24c) does not describe two coupled PDEs. System (24b)-(24c) describes an elliptic PDE, i.e., equation (24c), coupled to an ODE, i.e., equation (24b). The computational implementation of static-condensation is feasible simply because (24b) is an ODE. Just like any other ODE, it describes purely local behavior, therefore, it can always be eliminated from the linear algebra system regardless of the space discretization of choice (continuous finite elements, discontinuous finite elements, finite volumes, finite differences, etc).

Numerical coupling of an Elliptic PDE to an ODE is a problem that, to the best of our knowledge, is not covered in any standard textbook of numerical analysis of partial differential equations, see for instance standard references [32, 78, 70, 46]. Similarly, we are not aware of any publication advancing the use of static condensation in the context of PDE-ODE coupling. However, PDE-ODE-coupling is a recurrent motif in the context of computational physics. Perhaps, the biggest example is particle-in-cell-method (PIC), and generally speaking the evolution of particle systems subject to forces, with such forces usually being the computed from the solution of an elliptic/parabolic/hyperbolic PDE. In this very specific context, we think that our application of static condensation may be an original idea that could have applications beyond the context of the current report.

For the sake of completeness, in the following remark, we provide the statically-condensed assembly loop for the case of the θ-scheme as described in (34)-(35).

Remark 4.5 (θ-scheme static condensation assembly)**.** The assembly of the θ-scheme (34)-(35) can be written as

$$\sum_{K\in\mathcal{T}_h} \mathcal{K}_K\Phi_K^{n+1} + \theta\mathcal{B}_K\mathbf{V}_K^{n+1} = \sum_{K\in\mathcal{T}_h} \mathcal{K}_K\Phi_K^{n} - (1-\theta)\mathcal{B}_K\mathbf{V}_K^{n}, \tag{45}$$

$$\theta\mathcal{C}_K\Phi_K^{n+1} + \big[\mathcal{M}_K + \theta(\mathcal{D}_K + \mathcal{S}_K^{\nu})\big]\mathbf{V}_K^{n+1} = \big[\mathcal{M}_K - (1-\theta)(\mathcal{D}_K + \mathcal{S}_K^{\nu})\big]\mathbf{V}_K^{n} - (1-\theta)\mathcal{C}_K\Phi_K^{n}. \tag{46}$$

Here, the element matrices $\mathcal{K}_K$, $\mathcal{B}_K$, $\mathcal{C}_K$, $\mathcal{M}_K$, $\mathcal{D}_K$, and $\mathcal{S}_K^{\nu}$ follow definitions (39) and (41). From (46), we can solve for $\mathbf{V}_K^{n+1}$ to get

$$\mathbf{V}_K^{n+1} = \mathcal{G}_K\big[\mathcal{M}_K - (1-\theta)(\mathcal{D}_K + \mathcal{S}_K^{\nu})\big]\mathbf{V}_K^{n} - \mathcal{G}_K\mathcal{C}_K[(1-\theta)\Phi_K^{n} + \theta\Phi_K^{n+1}] \tag{47}$$

where $\mathcal{G}_K := \big[\mathcal{M}_K + \theta(\mathcal{D}_K + \mathcal{S}_K^{\nu})\big]^{-1}$. Multiplying (47) by $\theta\mathcal{B}_K$ and inserting the resulting identity in (45), after some reorganization we get

$$\begin{aligned}
&\mathcal{K}_K\Phi_K^{n+1} - \theta^2\mathcal{B}_K\mathcal{G}_K\mathcal{C}_K\Phi_K^{n+1} = \\
&\quad = \big[\mathcal{K}_K + \theta(1-\theta)\mathcal{B}_K\mathcal{G}_K\mathcal{C}_K\big]\Phi_K^{n} \\
&\quad - \big\{(1-\theta)\mathcal{B}_K + \theta\mathcal{B}_K\mathcal{G}_K\big[(1-\tfrac{\tau}{\mathcal{T}}(1-\theta))\mathcal{M}_K - (1-\theta)\mathcal{S}_K^{\nu})\big]\big\}\mathbf{V}_K^{n}.
\end{aligned}$$

Therefore, we consider the following gather-scatter loop in order to implement the θ-scheme:

```
Clean matrices/vectors: $\mathcal{A} = 0\,, \mathbf{F} = 0$
for all $K \in \mathcal{T}_h$
  $\rho_K \leftarrow$ gather_from_vector($\rho$)
  $\mathbf{B}_K \leftarrow$ gather_from_vector($\mathbf{B}$)
  Assemble: $\mathcal{K}_K\,,\ \mathcal{B}_K\,,\ \mathcal{C}_K\,,\ \mathcal{M}_K^v,\ \mathcal{D}_K^v,\ \mathcal{S}_K^v$
  Assign: $\mathcal{G}_K \leftarrow \big[(1 + \frac{\theta\tau}{\mathcal{T}})\mathcal{M}_K + \theta\mathcal{S}_K^v)\big]^{-1}$
  Assign: $\mathcal{A}_K \leftarrow \mathcal{K}_K - \theta^2 \mathcal{B}_K \mathcal{G}_K \mathcal{C}_K$                                        (48)
  Assign: $\mathbf{F}_K \leftarrow \big[\mathcal{K}_K + \theta(1-\theta)\mathcal{B}_K \mathcal{G}_K \mathcal{C}_K\big]\Phi_K^n$
                 $- \big\{(1-\theta)\mathcal{B}_K + \theta\mathcal{B}_K \mathcal{G}_K \big[\mathcal{M}_K - (1-\theta)(\mathcal{D}_K + \mathcal{S}_K^v)\big]\big\}\mathbf{V}_K^n$
  scatter_into_matrix($\mathcal{A}_K, \mathcal{A}$)
  scatter_into_vector($\mathbf{F}_K, \mathbf{F}$)
end for
```

Remark 4.6 (Choice of finite element spaces)**.** When considering the numerical implementation of any mixed-like formulation, it is fundamental to guarantee that the contribution resulting from the off-diagonal block-matrices end-up being equivalent to a full-rank matrix. Otherwise, the linear algebra system may either be non-invertible, exhibit strong degradation of its condition number when $h \to 0^+$, or severely ill-posed at extreme regimes, in particular, when $\frac{q_e^2}{\varepsilon m_e^2} \max_{i \in \mathcal{V}_H} \rho_i$ is large (see Section 4.2 of [83]).

On the other hand, an entire body of mathematical theory was developed in order to obtain well-posed mixed formulations that today we know as the finite element inf-sup theory [7, 32]. In the context of our problem, the off-diagonal blocks are defined by the elemental matrices $\mathcal{B}_K$ and $\mathcal{C}_K$ defined in (39) and (41) respectively. The finite element spaces $\boldsymbol{\mathbb{V}} := [\mathbb{V}]^2$ for the velocity/momentum, and $\mathbb{H}$ for the potential, as defined in Section 4.2, are only an 'educated guess' based on some acquired experience. We assumed that the finite element pair $\{\boldsymbol{\mathbb{V}}, \mathbb{H}\}$ was the best candidate for the satisfaction of inf-sup compatibility conditions and other coding-related constraints. We made no effort in order to establish that inf-sup compatibility conditions hold rigorously.

However, we have fairly strong evidence suggesting that the finite element $\{\boldsymbol{\mathbb{V}}, \mathbb{H}\}$ is well-behaved. Even at extreme regimes, while also pushing some parameters well-past the limits of $\mathcal{O}(10^9)$ or $\mathcal{O}(10^{-9})$, the resulting linear algebra system, preconditioned with one exact LU-factorization[3] of the symmetric homogeneous Laplacian, does not use more than one BiCgStab iteration. This means that the non-symmetric matrix $\mathcal{A}$, resulting from the assembly described in Algorithms (44) or (48), is as well-conditioned as the matrix of the Poisson equation. This can be easily explained from the scaling of the block $\mathcal{B}_K \mathcal{G}_K \mathcal{C}_K$ in the assembly loops. Some inspection reveals that $\mathcal{B}_K \mathcal{G}_K \mathcal{C}_K = \mathcal{O}(\frac{\tau^2}{h^2})$. But since the scheme is bound by the *cfl* conditions from the hyperbolics solver, we have that $\frac{\tau}{h} \lesssim \mathcal{O}(1)$, therefore we conclude that $\mathcal{B}_K \mathcal{G}_K \mathcal{C}_K \simeq \mathcal{O}(\frac{\tau^2}{h^2}) = \mathcal{O}(1)$. Still rigorous analysis and further testing might be needed.

---

[3] We used the Sparse Multifrontal solver UMFPACK for such tests.

5. MINIMAL CONDITIONS FOR ENTROPY-STABILITY

For the sake of simplicity, in this section we assume that we use Yanenko-splitting as described in Algorithm 3. The proof of stability of Marchuk-Strang splitting is rather similar, but it is lengthier and conveys no additional intellectual value (details are left to the reader).

Lemma 5.1 (Minimal conditions for entropy/energy stability)**.** *We assume a closed bounded smooth domain, and Euler-Poisson system as described in* (1) *using: reflecting boundary conditions for the Euler's subsystem, meaning* $\mathbf{p} \cdot \mathrm{n} = 0$*, and either homogeneous Dirichlet* $\varphi = 0$*, or homogeneous Neumann* $\nabla\varphi \cdot \mathrm{n} = 0$*, boundary conditions on the entirety of the boundary. In addition, we also assume* $\frac{1}{\mathscr{T}} \equiv 0$*, that is, we assume no physical dissipation mechanism. With such a setup of boundary conditions and no physical dissipation mechanisms, from* (1) *and* (5)*, we know that mass and momentum should be conserved, while total entropy should be either conserved or dissipated. In essence, all energy/entropy fluxes at the boundary vanish: i.e., we consider an electro-mechanically isolated system.*

Now, for Stage #1 of Yanenko's scheme, as described in Algorithm 3, assume that the numerical method used to solve Euler's equation is either entropy-conservative or entropy-dissipative in the sense that:

$$\sum_{i\in\mathcal{V}_H} m_i \eta(\mathbf{u}_i^{n+\frac{1}{2}}) \leq \sum_{i\in\mathcal{V}_H} m_i \eta(\mathbf{u}_i^n), \tag{49}$$

where $\mathcal{V}_H$ *is the set of all nodes of the finite element space* $\mathbb{V}$ *(see Section 4.2),* $\mathbf{u}^n = [\rho^n, \mathbf{p}^n]^\top$*,* $\mathbf{u}^{n+\frac{1}{2}} = [\rho^{n+1}, \mathbf{p}^{n+\frac{1}{2}}]^\top$*, and* $\eta(\mathbf{u}) = \eta([\rho, \mathbf{p}]^\top) = \frac{1}{2}\frac{|\mathbf{p}|^2}{\rho} + \theta\rho\ln\rho$*. Similarly, for the Stage #2 of Algorithm 3, assume that we use either an energy-conservative or energy-dissipative scheme in the sense that*

$$\sum_{i\in\mathcal{V}_H} \frac{m_i}{2}\frac{|\mathbf{p}_i^{n+1}|^2}{\rho_i^{n+1}} + \frac{\varepsilon}{2}\|\nabla\varphi_h^{n+1}\|_{L^2(\Omega)}^2 \leq \sum_{i\in\mathcal{V}_H} \frac{m_i}{2}\frac{|\mathbf{p}_i^{n+\frac{1}{2}}|^2}{\rho_i^{n+1}} + \frac{\varepsilon}{2}\|\nabla\varphi_h^{n}\|_{L^2(\Omega)}^2, \tag{50}$$

then we have that

$$\sum_{i\in\mathcal{V}_H} m_i \eta(\mathbf{u}_i^{n+1}) + \frac{\varepsilon}{2}\|\nabla\varphi_h^{n+1}\|_{L^2(\Omega)}^2 \leq \sum_{i\in\mathcal{V}_H} m_i \eta(\mathbf{u}_i^n) + \frac{\varepsilon}{2}\|\nabla\varphi_h^{n}\|_{L^2(\Omega)}^2, \tag{51}$$

which is a discrete counterpart of the entropy estimate (5)*.*

Proof. The proof is rather trivial, it just follows by using the definition of $\eta(\mathbf{u}) = \frac{1}{2}\frac{|\mathbf{p}|^2}{\rho} + \theta\rho\ln\rho$, with $\mathbf{u} = [\rho^{n+1}, \mathbf{p}^{n+\frac{1}{2}}]^\top$ for the left-hand side of (49), and $\mathbf{u} = [\rho^n, \mathbf{p}^n]^\top$ for its right-hand, which leads to:

$$\sum_{i\in\mathcal{V}_H} m_i\Big(\frac{1}{2}\frac{|\mathbf{p}_i^{n+\frac{1}{2}}|^2}{\rho_i^{n+1}} + \theta\rho_i^{n+1}\ln\rho_i^{n+1}\Big) \leq \sum_{i\in\mathcal{V}_H} m_i\Big(\frac{1}{2}\frac{|\mathbf{p}_i^{n}|^2}{\rho_i^{n}} + \theta\rho_i^{n}\ln\rho_i^{n}\Big). \tag{52}$$

Now, adding (52) and (50) we get

$$\sum_{i\in\mathcal{V}_H} m_i\Big(\frac{1}{2}\frac{|\mathbf{p}_i^{n+1}|^2}{\rho_i^{n+1}} + \theta\rho_i^{n+1}\ln\rho_i^{n+1}\Big) + \frac{\varepsilon}{2}\|\nabla\varphi_h^{n+1}\|_{L^2(\Omega)}^2 \leq \\ \sum_{i\in\mathcal{V}_H} m_i\Big(\frac{1}{2}\frac{|\mathbf{p}_i^{n}|^2}{\rho_i^{n}} + \theta\rho_i^{n}\ln\rho_i^{n}\Big) + \tfrac{\varepsilon}{2}\|\nabla\varphi_h^{n}\|_{L^2(\Omega)}^2 \,, \tag{53}$$

which is just a re-writing of (51). □

We highlight here:

- Extension of this proof for the case of isentropic closure, meaning $p = \kappa\rho^\gamma$ with $\gamma > 1$ is relatively straightforward: the reader only needs to change the definition of entropy $\eta(\mathbf{u})$.
- Extension of this proof beyond the case of barotropic Euler models (isothermal or isentropic) into the full-Euler models having an evolution equation for the total mechanical energy can also be accommodated. See the proof of energy-stability in [83, Lemma 3.3] for the case of the full Euler-Maxwell system.

In order to study the role of the source-update scheme in relationship to numerical stability and entropy dissipation, let us consider the following rather trivial proposition:

Proposition 5.1 (Entropy productive source-update schemes)**.** *Assume that* (49) *is satisfied with an exact equality sign. Assume that* (50) *is satisfied with a strict inequality sign. Then,* (51) *will be satisfied with a strict inequality.*

An important consequence of this proposition is that even if the hyperbolic-solver is entropy conservative, the overall behavior of the operator splitting scheme might still be entropy dissipative. Without any additional rigorous argument and/or computational evidence, at this point in time, it is unclear whether using a dissipative source-update scheme is either beneficial or detrimental the to whole stability of the scheme. Therefore, we define the following ‘classification criteria’ of source-update schemes:

- *Non-entropic.* For instance the Crank-Nicolson scheme, as described by (34)-(35) with $\theta = 1/2$, is *non-entropic* since it cannot contribute to the production of entropy, i.e. it satisfies (50) with an exact equality.
- *Entropic.* We say that Backward-Euler scheme, defined in (31)-(32), is *entropic*, since the functional $Q(\mathbf{u}_h^n, \mathbf{u}_h^{n+1})$, as defined in (33), is non-negative. In fact, unless the numerical solution happens to be constant in time, Backward-Euler will satisfy (50) with strict inequality sign. Similarly, the Crouzeix DIRK23 scheme is *entropic*, since the dissipation functional $Q(\mathbf{u}_h^n, \mathbf{u}_h^1, \mathbf{u}_h^2)$, as defined in (36), is non-negative.

Later in the Section 6.4, computational experiments seem to provide a reasonable answer as to whether the source-update scheme should be *entropic* or *non-entropic*.

6. COMPUTATIONAL EXPERIMENTS

6.1. Target regime of interest

The numerical experiments considered in this report target very specifically the following regime:

(i) Large Magnetic fields: $|\mathbf{B}| \gg 1$.

(ii) Small electron mass: $m_e \ll 1$.

(iii) Small electric permittivity $\varepsilon \ll 1$.

(iv) Large density contrast-ratio: i.e., given an electron mass density $\rho(\boldsymbol{x})$ with $\boldsymbol{x} \in \Omega$, we define the density contrast-ratio as

$$r_\rho := \frac{\max_{\boldsymbol{x}\in\Omega} \rho(\boldsymbol{x})}{\min_{\boldsymbol{x}\in\Omega} \rho(\boldsymbol{x})} .$$

We are interested in regimes where $r_\rho \gg 1$.

(v) Strongly non-neutral plasma. We are interested in regimes where the vast majority of the plasma in the domain is electrically non-neutral. In practice, what this means is that, we want to consider an electron-gas with minimal to no screening from the background charges.

(vi) Low pressure/temperature: in the context of isothermal Euler-Poisson model we assume $\theta \ll 1$.

The regime described by (i) – (vi) is indeed problematic, even in the absence of shocks or strong expansions, most shock-hydrodynamics fluid-plasma codes will struggle to bring simulations to completion. This regime is strongly dominated by very high-frequency phenomena ‘superposed’ on top of macroscopic transport, strong source terms leading to quite violent accelerations, and the formation of diffusive-like internal layers. The degree of difficulty of this regime is rather different from the canonical shock-hydrodynamics physics. In this context three kinds of failure can occur:

- *Catastrophic failure:* the scheme crashes in one time step because positive density or internal energy cannot be preserved. In our case, this is not possible, since the schemes used for the hyperbolic subsystem are based on the invariant domain discretization methods described in [53] for which catastrophic failure is simply not possible.
- *Non-entropic failure:* the numerical scheme appears to succeed, but delivers a solution that cannot be physical. When this happens we will call such solution *non-entropic*.
- *Technical failure:* this is when no catastrophic failure occurs, but abnormally high material velocities or sound speeds occur at some points in the domain. Using various codes and schemes, we have observed that in the asymptotic drift-regime, seemingly innocuous simulations of smooth flows, may develop abnormally high speeds of propagation. Since the time-step size is controlled by the hyperbolic *cfl*, this can easily lead to some simulations requiring in excess of a trillion time-steps to reach completion. For any practical purpose, most simulations requiring a trillion time-steps have no *technical utility* and are preemptively aborted.

The three most important characteristic frequencies associated to the regime described by bullets (i)-(vi) are the plasma angular frequency, the cyclotron frequency, and the Diocotron frequency, defined respectively by

$$\omega_p = \sqrt{\frac{n_e q_e^2}{\varepsilon m_e}}\,,\ \omega_c = \frac{|\mathbf{B}| q_e}{m_e}\,,\ \omega_d = \frac{\omega_p^2}{\omega_c}\,, \tag{54}$$

with respective characteristic plasma period, cyclotron period, and the Diocotron period defined by

$$T_p = \frac{2\pi}{\omega_p}\,,\ T_c = \frac{2\pi}{\omega_c}\,,\ T_d = \frac{2\pi}{\omega_d}\,.$$

A precise physical meaning of the plasma and cyclotron frequencies can be found in the introductory section of countless plasma physics books, see for instance [14, 6]. Both the plasma and cyclotron oscillation represent very high-frequency motions that, in general, will not lead to coherent macroscopic motion of the fluid. In general, time-resolving plasma and cyclotron high-frequency oscillation do not represent technically meaningful goals. On the other hand, the Diocotron frequency ω_d is related to a slower dynamics that can be related (at least with some approximate arguments) to the averaged material velocity $\overline{\mathbf{v}} = \frac{1}{T}\int_0^T \mathbf{v}(t)\mathrm{d}t$ for some $T \gg \max\{T_p, T_c\}$. See also Remark 6.2 for more details.

6.2. Setup of the Diocotron instability

A challenging test problem for the development and testing of numerical methods for the regime described in the previous subsection is the so-called cold-plasma Diocotron instability. The initial setup consists circular domain, with an uniform negative electric charge density within the support of an annulus, rotating around the origin, at negligible temperature (i.e., negligible pressure). The initial conditions should be in a state of force equilibrium: the electrostatic forces, pressure forces, and centrifugal forces, all of them pushing the electrons outwards, are in perfect equilibrium with the Lorentz force pushing the electron inwards.

Therefore, we consider a circular domain Ω of radius $r_3 = 16$, that is

$$\Omega = \{\boldsymbol{x} \in \mathbb{R}^2 \,|\, |\boldsymbol{x}|_{\ell^2} \leq r_3\}\,, \tag{55}$$

with boundary conditions $\mathbf{p}\cdot\mathrm{n} = 0$ and $\varphi = 0$ on the entirety of $\partial\Omega$. We consider two positive small parameters $0 < \delta \ll 1$ and $0 < \upsilon \ll 1$, and set the values of the physical constants as follows:

$$m_e = \delta,\ \varepsilon = \delta,\ |\mathbf{B}| = \tfrac{1000}{\delta}\,,\ q_e = -1\,,\ \theta = \upsilon\,. \tag{56}$$

We define the radii r_2 and r_1:

$$r_2 = c_1 \cdot r_3\,,\ r_1 = c_2 \cdot r_2\,,\quad \text{with}\ \ c_1 = 0.5\,,\ c_2 = 0.815\,, \tag{57}$$

which are used to define a negatively charged particle number density n_e as

$$n_e = \begin{cases} \upsilon n_0 & \text{if } |\boldsymbol{x}|_{\ell^2} \leq r_1 \\ n_0(1 + 0.01\sin(2\pi\ell\theta)) & \text{if } r_1 < |\boldsymbol{x}|_{\ell^2} \leq r_2 \\ \upsilon n_0 & \text{if } r_2 < |\boldsymbol{x}|_{\ell^2} \leq r_3 \end{cases} \quad \text{with}\ \ n_0 = 1\,, \tag{58}$$

where $\ell = 5$. We also set a fixed, constant in time and space, positive background charge in the entirety of the domain of value $q_b n_b = -q_e \cdot \delta_2 \cdot n_0$. In all our simulations we use the final time t_F defined by:

$$t_F = 6\frac{2\pi}{\omega_{d0}} \ \text{ where } \ \omega_{d0} = \frac{\omega_{p0}^2}{\omega_c} \ \text{ and } \ \omega_{p0}^2 = \frac{n_0 q_e^2}{\varepsilon m_e} \tag{59}$$

while ω_c follows from (54). In other words, the final time is equal to to six times the initial value of the Diocotron period. From a macroscopic perspective this should translate, approximately, into six 'solid body rotations' of the Diocotron instability.

Finally, the initial velocity is given by:

$$\mathbf{v} := \boldsymbol{\omega}(r) \times \boldsymbol{r} \ \text{ where } \ \boldsymbol{\omega} = \omega(r)\widehat{k}\ , \ \ \boldsymbol{r} = [\boldsymbol{r}_1, \boldsymbol{r}_2, 0]^\top \ , \ \ r = |\boldsymbol{x}|\ , \tag{60}$$

In Remark 6.2 we describe a quasi-analytical procedure in order to compute $\boldsymbol{\omega}(r)$ (numerically) leading to force equilibrium in the context fluid-plasmas with negligible (but non-zero) pressure.

The setup described by (55)-(60) is anything but accidental. In the following remark we briefly explain how it was developed.

Remark 6.1. We describe how the setup (55)-(60) was chosen:

- ◇ The coefficients c_1 and c_2 defined in (57) were picked by visual inspection from Fig. 3 in [24]. Such coefficients were specifically selected and fined-tuned (by trial and error) in order to maximize the excitation of the 5-mode of the Diocotron instability. An alternative to visual inspection is using the formulas (26)-(28) in [24] in order to compute the growth-rates.
- ◇ In order to guarantee that the Euler-Poisson with a given magnetic field is operating in the E×B-drift limit we have to satisfy the condition $\frac{\omega_p^2}{\omega_c^2} \ll 1$, see for instance [24, 74]. Using the formulas in (56), a direct computation shows that for any value of δ we have that $\frac{\omega_p^2}{\omega_c^2} = \delta^2 10^{-6}$.
- ◇ From reference [24] we also know that it is almost impossible to excite 'just one' Diocotron mode. For instance, we note from Fig. 3 in [24], that exciting the 5-mode will necessarily excite the 4-mode and 6-mode. Pollution from other higher and lower modes will necessarily lead to destructive interference. This motivates seeding the initial profile, as described in (58), in order to minimize pollution from other modes. Even with such preparation of the data, on the long run, the 4-mode and 6-mode will eventually grow fast enough to destroy the θ-periodicity of the solution. That is why in all the simulations presented in this manuscript we use the final time described in (59). Direct computation of the final time, using (59) and definitions (56), reveals that $\omega_d = 10^{-3}$. Therefore the final time t_F is always a constant independent of δ.
- ◇ Overall, the problem setup (55)-(60) is heavily inspired from that one described in [19, 20] but slightly tweaked in order to make the testing conditions even more severe (e.g. larger plasma frequency, larger cyclotron frequency, stronger vacuum, etc).

Hopefully, these explanations are enough to convince the reader that, indeed, the setup proposed by (55)-(60) is computationally challenging and that it is representative of the E×B asymptotic drift limit.

Remark 6.2 (Quasi-analytical computation of equilibrium profiles)**.** The initial velocity profile $\mathbf{v}$ of the Diocotron problem satisfies the following equilibrium relationship:

$$\rho(\mathbf{v}\cdot\nabla)\mathbf{v}+\nabla p=-\tfrac{q_e}{m_e}\rho\nabla\varphi+\tfrac{q_e}{m_e}\rho\mathbf{v}\times\mathbf{B}\,. \tag{61}$$

Using (60) we can rewrite (61) as follows

$$-\rho\omega(r)^2\boldsymbol{r}+\nabla p=-\tfrac{q_e}{m_e}\rho\nabla\varphi+\tfrac{q_e}{m_e}\rho\omega(r)(\boldsymbol{r}_\perp\times\mathbf{B}) \text{ where } \boldsymbol{r}_\perp:=[-\boldsymbol{r}_2,\boldsymbol{r}_1,0]^\top\,.$$

Taking the dot product with $\boldsymbol{r}$ we get

$$-\rho\omega(r)^2|\boldsymbol{r}|_{\ell^2}^2+\nabla p\cdot\boldsymbol{r}=-\tfrac{q_e}{m_e}\rho\nabla\varphi\cdot\boldsymbol{r}+\tfrac{q_e}{m_e}\rho\omega(r)(\boldsymbol{r}_\perp\times\mathbf{B})\cdot\boldsymbol{r}\,,$$

which can be finally reorganized as

$$\underbrace{(\rho|\boldsymbol{r}|_{\ell^2}^2)}_{=a}\omega(r)^2+\underbrace{\big(\tfrac{q_e}{m_e}\rho(\boldsymbol{r}_\perp\times\mathbf{B})\cdot\boldsymbol{r}\big)}_{=b}\omega(r)\underbrace{-\big(\nabla p\cdot\boldsymbol{r}+\tfrac{q_e}{m_e}\rho\nabla\varphi\cdot\boldsymbol{r}\big)}_{=c}=0\,, \tag{62}$$

which is clearly a quadratic equation for $\omega(r)$. Therefore, the algorithm/script required to compute equilibrium profiles consists in the following steps: (i) Choose a θ-symmetric electron density and background density profiles n_e and n_b respectively, (ii) Compute the pressure $p=\theta_0\rho=\theta_0 m_e n_e$ using the electron density profile n_e chosen in step (i), (iii) find the corresponding electrical potential by solving $-\varepsilon\Delta\varphi=q_e n_e+q_b n_b$ with proper boundary conditions, (iv) Solve the quadratic equation:

$$(\rho_i|\boldsymbol{r}_i|_{\ell^2}^2)\omega(r_i)^2+\big(\tfrac{q_e}{m_e}\rho_i(\boldsymbol{r}_{i,\perp}\times\mathbf{B})\cdot\boldsymbol{r}_i\big)\omega(r_i)-\big((\nabla_h p_h)_i\cdot\boldsymbol{r}_i+\tfrac{q_e}{m_e}\rho_i(\nabla\varphi_h)_i\cdot\boldsymbol{r}_i\big)=0 \tag{63}$$

for all $i\in\mathcal{V}_H(K)$, where $\rho_i=\rho_h(\boldsymbol{x}_i)$ is the discontinuous finite element density evaluated at the node $\boldsymbol{x}_i$, similarly $(\nabla_h p_h)_i=\nabla_h p_h\big|_K(\boldsymbol{x}_i)$ represents the broken-gradient of the pressure evaluated at the node $\boldsymbol{x}_i$, and $(\nabla\varphi_h)_i=\nabla_h\varphi_h\big|_K(\boldsymbol{x}_i)$ represents the finite element gradient of the potential evaluated at the corresponding node[4]. As expected, (63) has two solutions, $\omega_1(r_i)^2$ and $\omega_2(r_i)^2$, and it is important to know how to pick the right one. Some inspection reveals that:

- $\omega_1(r_i)^2=\frac{-b_i-\sqrt{b_i^2-4a_ic_i}}{2a_i}$: under the assumption of $\frac{\omega_p^2}{\omega_c^2}\ll 1$, some informal asymptotics implies that $\omega_1(r_i)\approx\omega_d$. This corresponds with the unstable equilibrium profile.
- $\omega_2(r_i)^2=\frac{-b_i+\sqrt{b_i^2-4a_ic_i}}{2a_i}$: again under the assumption of $\frac{\omega_p^2}{\omega_c^2}\ll 1$, the educated guess is that $\omega_2(r_i)\approx\omega_c$. See also [74], formulas (8)-(10), for some analytical details.

Therefore, in all the computations reported in this manuscript we always choose $\omega_1(r_i)$ in order to define an initial velocity profile. This algorithm can be encoded into any reasonable finite element library/framework and will deliver quite accurate equilibrium profiles without resorting to iterative solution methods. We highlight that we are not aware of any other scientific publication reporting a systematic procedure for the construction of initial equilibrium profiles.

---

[4] Note that the gradient of $\mathcal{C}^0$ finite element functions is multi-valued at nodes. In this context, the value of the gradient at the node means: the restriction $\nabla\varphi_h\big|_K$ evaluated at the node $\boldsymbol{x}_i$

6.3. Computational study #1: computation of reference solution

In this section we consider the setup described by (55)-(60) with $\delta = 0.01$ and $\upsilon = 10^{-5}$, in order to provide a reference/well-resolved solution.

We used the scheme for isothermal Euler-Poisson with a given magnetic field, advanced in Section 4, with the Crouzeix's DIRK23 scheme for the source update scheme, adaptive time-step size in order to preserve a constant hyperbolic $cfl = 0.75$ (which is rather aggressive), and Gauss-law line-search restart as described in Algorithm 5. The mesh was generated from a base-coarse mesh to which we applied 8 uniform refinements using the bisection method, see Figure 6-1. This lead to 327,680 quadrilateral cells, 328,193 DOFs for the potential, and 1,310,720 DOFs for each component of the hyperbolic subsystem. The total computation uses a total of 58127 time-steps. From this total of 58127 time steps, we sampled 1600 frames, each one at an (approximate) temporal distance of $t_F/1600$ from each other. Some results are shown in Figure in 6-2.

At the start of the simulation the plasma, cyclotron, and Diocotron period are $T_p = 0.0628319$, $T_c = 6.28319 \cdot 10^{-7}$, and $T_d = 12566.4$ respectively, using formula (59) this leads to a final time $t_F = 75398.2$. The numerical scheme makes no attempt or provision to time-resolve, under-resolve or over-resolve the electrostatic plasma or cyclotron oscillation. In fact, the time-stepping logic is completely agnostic of such characteristic time-scales. For all the computations presented in this report: time-step size is solely determined by the choice time-explicit hyperbolic *cfl*, maximum speed of propagation of the hyperbolic sub-system (material and acoustic waves), and the meshsize h. The average time-step size τ throughout out the entire simulation is approximately 1.29, which is almost two orders of magnitude larger than the plasma period and eight orders of magnitude larger than the cyclotron period.

Some references from the mathematics literature reporting computational results for the Diocotron instability are [35, 36, 87, 76, 54, 69, 84, 30], similarly from physics journals we have [75, 15, 8, 88, 72, 62, 65, 60]. In light of these references, we highlight that all the computations presented in this report are rather unique, in the sense, that beyond reference [19] authored by the Co-PI, we are not aware of any pre-existing publication/report showing computations of the Diocotron instability using full-fledged fluid plasma models in Eulerian description. To the best of our knowledge all the pre-existing literature on the matter use either particle schemes (PIC), or drift-models (e.g. the guiding center model) with a semi-Lagrangian discretization[5] or a particle method. Strictly speaking, drift-models are not genuine fluid model, since they do not contain Euler's equation of gas dynamics as a subsystem. In particular, drift-models will necessarily neglect large portions of the physics associated to the electron dynamics, acoustic waves, and related inertial effects, therefore, their scope of utility is rather limited.

We also want to note that meshes used in the context semi-Lagrangian methods for drift-limit models use approximately 1,000,000 to 4,000,000 cells on the plane in order to reproduce the Diocotron instability, and highly specialized hermite-like space discretizations for the electrostatic problem, see for instance [35, 76]. On the other hand, as shown in Figure 6-2, we can resolve the instability using 327,680 cells. We believe this illustrates that traditional fluid-plasma models in Eulerian formulation can be very efficient when solved with proper numerical methods. Even with modest second-order space-time accuracy, it is possible to use relatively coarse meshes

---

[5] Semi-Lagrangian methods may be considered as an evolution of characteristics based methods.

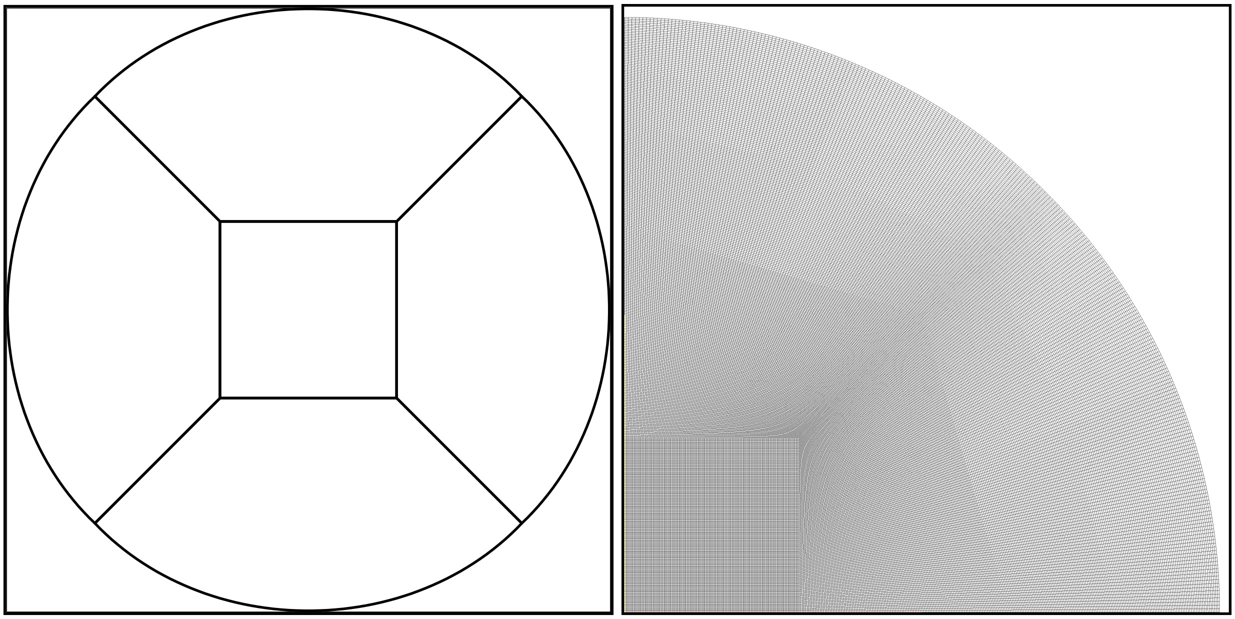

Figure 6-1 Mesh Generation. The picture in the left is the base coarse mesh having 5 cells. After the application of 8 uniform refinements using the bisection method we obtain a mesh with $5 \cdot 4^8 = 327,680$ cells which we display on the right (only one quarter of the whole geometry). Even though the figure in the left displays curved boundaries, we note that the actual finite element discretization uses local-to-global $\mathbb{Q}^1$ map. This means that for any computational purpose, the actual boundary of the 'numerical mesh' is polygonal (no curvature). We also want to highlight that even though this is a structured mesh, mesh quality by itself is not particularly good: some elements have significant distortion, in addition the transition of element size and/or width is not particularly smooth in some parts of the domain. Such mesh features are well-known to produce mesh imprint in the solution in the context of hyperbolic PDEs.

and still get meaningful results.

6.4. Computational study #2: entropic vs non-entropic source-update schemes.

In this section we consider the setup described by (55)-(60) with $\delta = 0.01$ and $\upsilon = 10^{-5}$. The mesh generation follows the same procedure described in Section 6.3, see Figure 6-1, but we only apply 7 uniform refinements to the base coarse mesh, which leads to 81,920 cells, 82,177 DOFs for the potential, and 327,680 DOFs for each scalar component of the hyperbolic subsystem.

We compare the performance of three different source-update schemes described in Section 4.3: Backward-Euler (31)-(32), Crank-Nicolson (34)-(35), and the Crouzeix's DIRK23 scheme. The primary metrics to evaluate the quality of the schemes are: qualitative visual comparison and time-step size statistics. In Figures 6-3 and 6-4 the reader can find the results for the Backward-Euler and DIRK23 schemes respectively. In Figure 6-6 we compare time-step size evolution for Backward-Euler, Crank-Nicolson and Crouzeix's DIRK23 scheme.

Neither Backward-Euler, nor Crank-Nicolson, nor DIRK23 scheme can fail catastrophically since the hyperbolic update (e.g. Stages #1 and #3 in the Context of Marchuk-Strang splitting, see

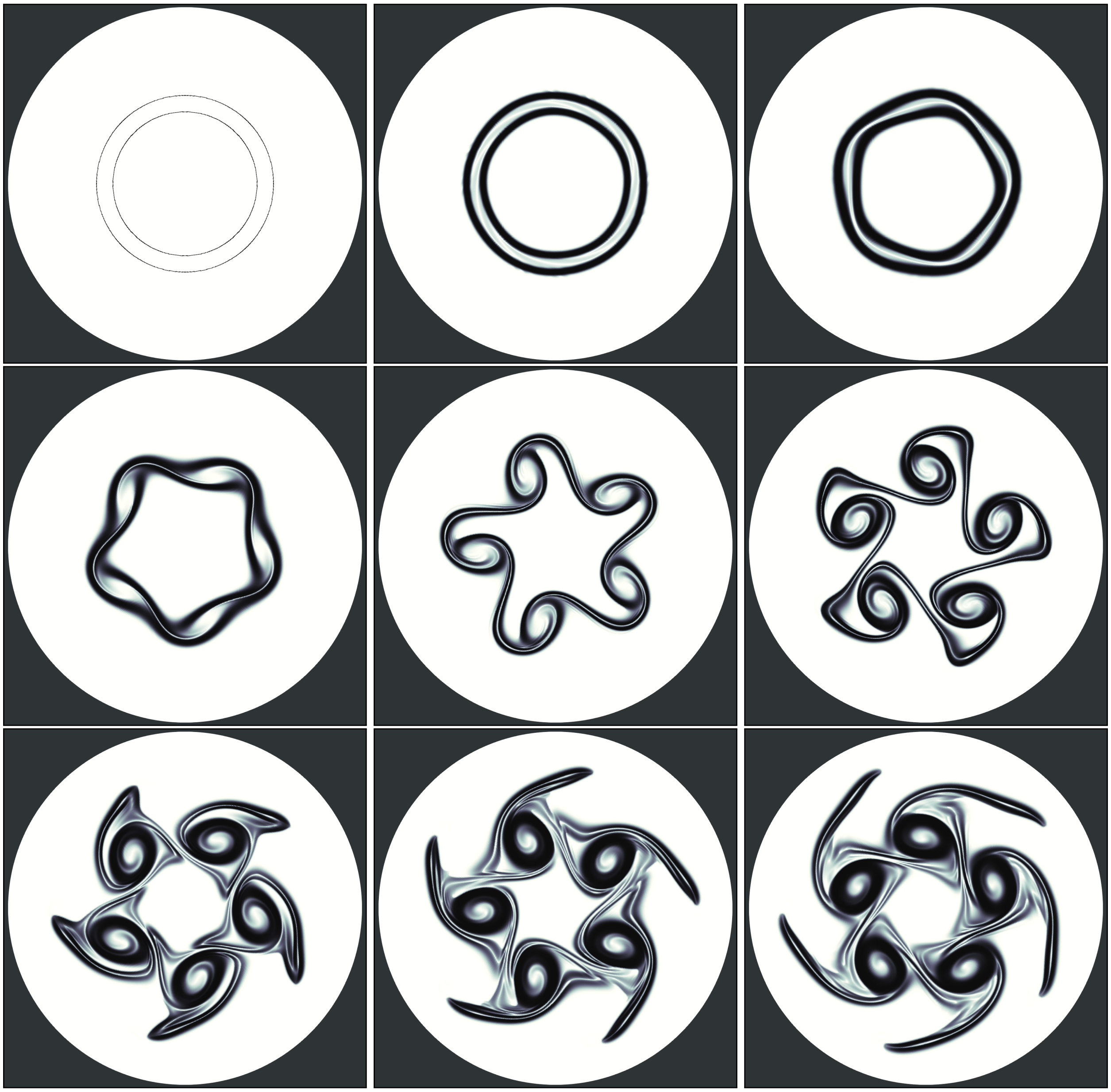

Figure 6-2 Reference solution. Schlieren snapshots 0, 200, 400, 600, 800, 1,000, 1,200, 1,400, and 1,600; corresponding with approximate times 0, $0.125t_F$, $0.25t_F$, $0.375t_F$, $0.5t_F$, $0.625t_F$, $0.75t_F$, $0.875t_F$, t_F. This is an over resolved 'reference computation' in order to compare the results using slightly coarser meshes. See Figure 6-1 for details in relationship to mesh geometry.

Algorithm 4) use the schemes described in [53] which have unconditional guarantees of robustness. However, Crank-Nicolson scheme could not meaningfully reach completion in any timely fashion: a crude estimate lead us to conclude that Crank-Nicolson requires in excess of a trillion time-steps in order to reach completion. All the computations using Crank-Nicolson were preemptively aborted. This was not our first encounter with such problems when using Crank-Nicolson's scheme, see [83]. This prompted us to consider the implementation of the θ-scheme as described in (34)-(35) in order to explain, or at least to try to understand, this behavior[6]. We considered running the θ-scheme with θ arbitrarily close to 0.5. After some experimentation we set $\theta = 0.500001$. With such a setup, the θ-scheme should provide a marginal/negligible supply or artificial dissipation, while still being representative of the Crank-Nicolson scheme.

The results of Backward-Euler and DIRK23 are somewhat expectable. In Figure 6-2 we can see that even though Backward-Euler works, its artificial dissipation damps all perturbations, both artificial and physical perturbations, leading to an overdamped picture of the Diocotron instability. On the other hand, in Figure 6-4 we can appreciate that the high-frequency artificial damping of DIRK23's scheme effectively trims the unresolved fast dynamics of the solution (the cyclotron and electrostatic plasma oscillations) leading to a smooth resolution of the macroscopic motions. We may think of DIRK23 scheme as numerical method with built-in high-order vanishing-damping mechanisms.

On the other hand, the results for Crank-Nicolson's scheme are rather shocking. The results in displayed in Figure 6-5 may lead us to prematurely conjecture that: *non-entropic* source-update schemes cannot meaningfully approximate a physically valid solution. It is worth noting that the computational experiments shown in Figure 6-5 are rather singular and are not stable with respect to perturbations. For instance, the computations shown in Figure 6-5 were repeated by adding 3% mesh distortion, and indeed, the Diocotron instability appears to manifest. However, such computations require in excess of 2 million time-steps in order to reach completion (compare with the modest number of 28,651 time-steps used by DIRK23). Similarly, using slightly larger or smaller value of θ might also slightly different final results.

We believe that the computational results shown in Figure 6-5 are strong evidence indicating that vanishing-damping mechanisms, see for instance formula (36), are an essential, if not fundamental, part of any numerical scheme that solves Euler-Maxwell and Euler-Poisson systems. At this point in time, this comment may be rightfully judged as premature and speculatory in nature. However, from purely pragmatic/utilitarian point of view, it is a our firm assessment that Crank-Nicolson scheme does not represent a computationally, mathematically, or physically meaningful solution. The computations of Figure 6-5 using Crank-Nicolson's scheme do not use a very large number of DOFs in two-space dimensions, but they still require an outrageous number of time steps in order to reach completion. For the time being, using DIRK23 for the source-update scheme appears to be the only technically meaningful solution in order to reach second-order accuracy while also using a modest number of time steps.

It is not possible to give a fully satisfactory mathematical explanation to the results of Figure 6-5. However, we highlight that such kind of nonphysical behavior is not unprecedented. In the context of hyperbolic system of conservation laws, non-entropic schemes have been reported, and

---

[6] In this manuscript the θ-scheme described in (34)-(35) was solely introduced in order to understand why Crank-Nicolson displays such a poor performance. Beyond that context, it's use was never intended.

in some cases mathematically proven, to produce fake stationary contacts/fronts, see for instance Lemma 3.2 in [52]. However, this is by no means an explanation of the results observed here.

6.5. Computational study #3: dependence on Gauss-law-restart

In this section we consider the setup described by (55)-(60) with $\delta = 0.01$ and $\upsilon = 10^{-5}$. The mesh generation follows the same procedure described in Section 6.3, see Figure 6-1, but we only apply 7 uniform refinements. With this setup, we compare the performance of three different kinds of Gauss-law restart:

- *Line-search Gauss-law restart:* this entails performing a line search for $\lambda \in [0,1]$ as described in Algorithm 5. This method is mathematically guaranteed to be energy-stable and provide some partial compliance with the Gauss-law.
- *No Gauss-law restart:* equivalent to hard-coding $\lambda = 0$ in Algorithm 5. This method is mathematically guaranteed to be energy-stable. Even though the scheme for the Euler-Poisson system advanced in this manuscript is high-order consistent (in-time) with respect to the Gauss-law, we can only expect that the violations of the Gauss-law will accumulate over the course of hundreds/thousands of time steps. Such deviation will necessarily have a qualitative impact in the solution, see Figure 6-7 first row, columns two and three.
- *Full Gauss-law restart:* equivalent to hard-coding $\lambda = 1$ in Algorithm 5. Note that this approach is fully compliant with the Gauss-law but cannot be guaranteed to be energy-stable.

See Figure 6-7 for visual comparison of the three different kinds of Gauss-law restart. The differences between line-search Gauss-law restart and full Gauss-law restart are pretty much minimal.

Preservation of the Gauss-law in the context of fluid plasma models is a rather technical issue. We might want to add some comments to this section that serve as important background:

- At this point in time, developing a scheme that is energy stable does not pose a challenge, see for instance [83]. Similarly, developing a scheme the preserves the Gauss-law $-\varepsilon\Delta\varphi = q_e n_e$ (with the equality understood in some weak sense) is not that difficult either, see for instance [18]. The real obstacles appear when we try to satisfy both energy-stability and Gauss-law. The fundamental problem has nothing to do with the numerical scheme, or the space discretization, or the time discretization. The antagonistic nature of 'energy-stability vs Gauss-law' is in the intrinsic nature of the PDE as we explain in the following bullet.
- If the Gauss-law is meant to be preserved by the exact solution, we should not expect it to hold true in a pointwise sense. Even expecting the Gauss-law to hold in an L^p-sense with p arbitrary is asking too much. More precisely, we have that $-\varepsilon\Delta\varphi = q_e n_e \in H^{-1}(\Omega)$ provided that $n_e \in L^p(\Omega)$ with $p \geq 6/5$, see Appendix B. The notion of a 'strong' Gauss-law carries no particular meaning in the context of the Euler-Poisson system. Even the notion of a weak Gauss-law hangs on a thin thread: there is absolutely no good reason to believe that the electron density will satisfy the conditions $n_e \in L^p(\Omega)$ with $p \geq 6/5$ for all time. If during the time evolution of exact solution, we have that $n_e \in L^p(\Omega)$ with $p < 6/5$, then the it will not be possible to guarantee that $\|\nabla\varphi\|_{L^2(\Omega)} \leq \mathit{const}$, and the exact

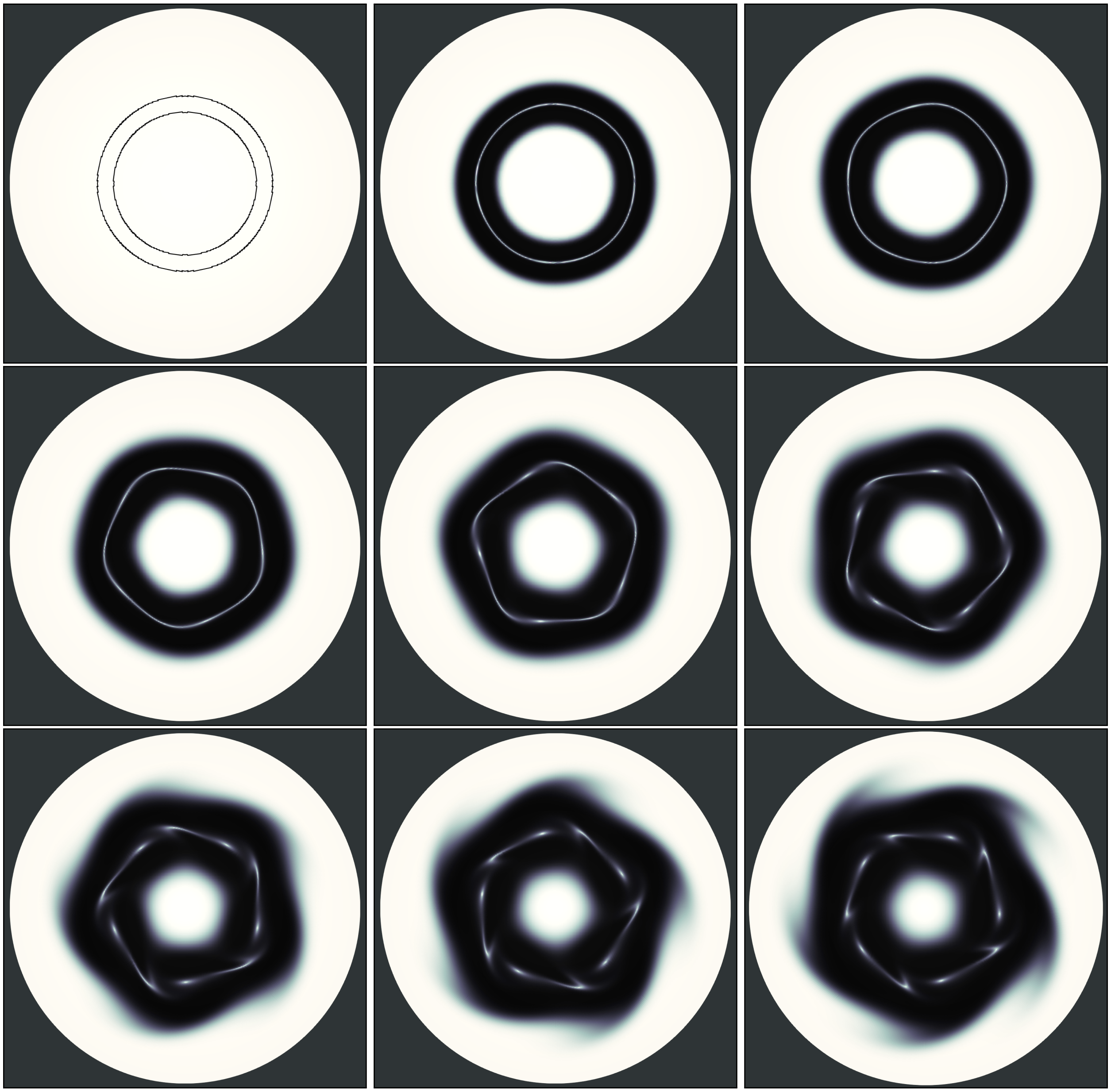

Figure 6-3 Backward-Euler. Schlieren snapshots 0, 200, 400, 600, 800, 1,000, 1,200, 1,400, and 1,600; corresponding with approximate times 0, $0.125t_F$, $0.25t_F$, $0.375t_F$, $0.5t_F$, $0.625t_F$, $0.75t_F$, $0.875t_F$, t_F. This computation uses a total of 27086 time-steps. These snapshots are meant to be compared with those of Figure 6-2. Essentially, when using the Backward-Euler method for the source-update scheme, we get an overdamped Diocotron instability. This is not completely surprising. In the context of computational fluid dynamics it is somewhat known that first-order methods (either in time or space) struggle to reproduce hydrodynamic instabilities, and sometimes they are unable to manifest them at all, see for instance [67].

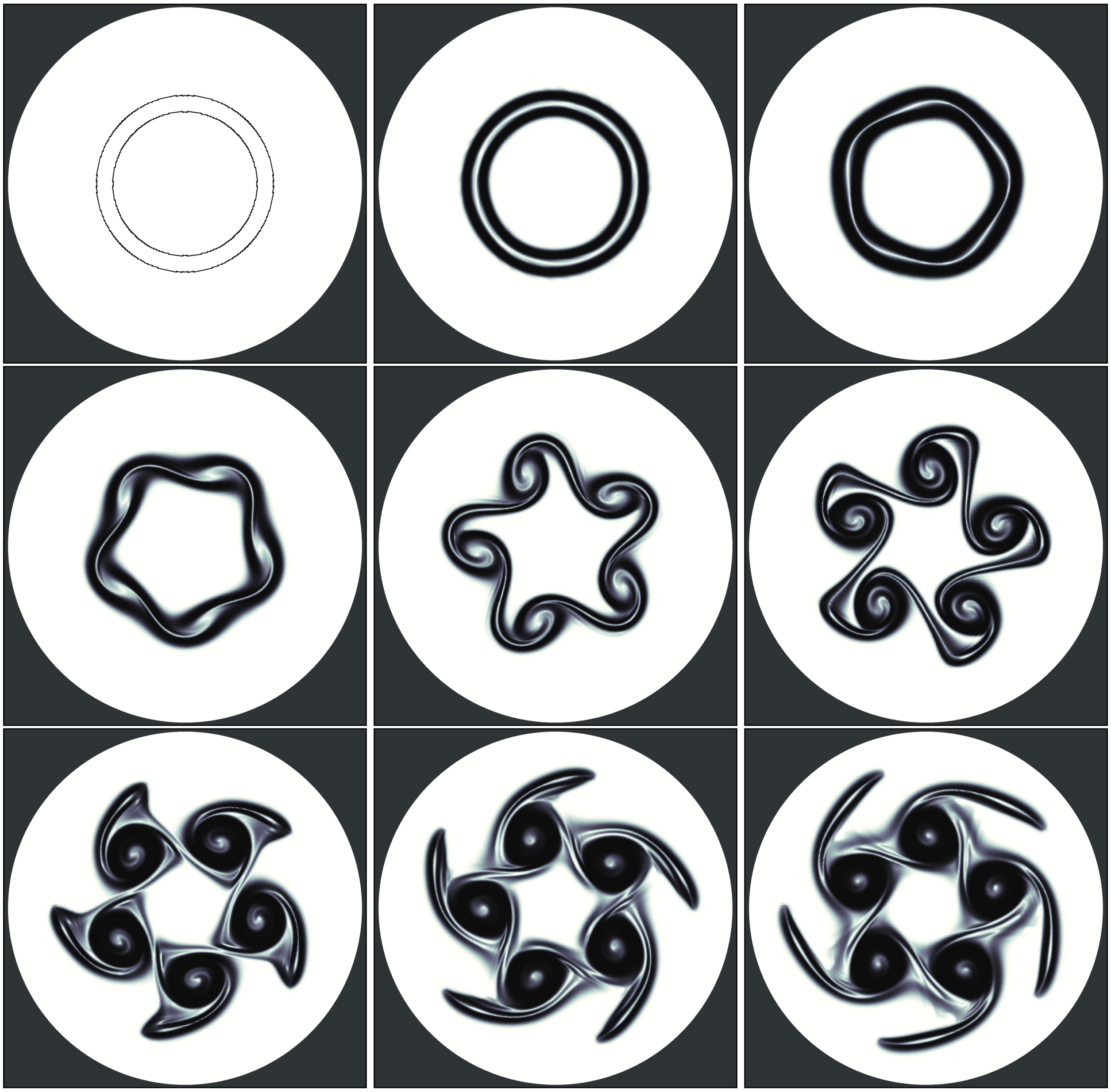

Figure 6-4 Crouzeix's DIRK23. Schlieren snapshots 0, 200, 400, 600, 800, 1,000, 1,200, 1,400, and 1,600; corresponding with approximate times 0, $0.125t_F$, $0.25t_F$, $0.375t_F$, $0.5t_F$, $0.625t_F$, $0.75t_F$, $0.875t_F$, t_F**. This computation uses a total of 2,8651 time-steps. These snapshots compare favorably with those of Figure 6-2.**

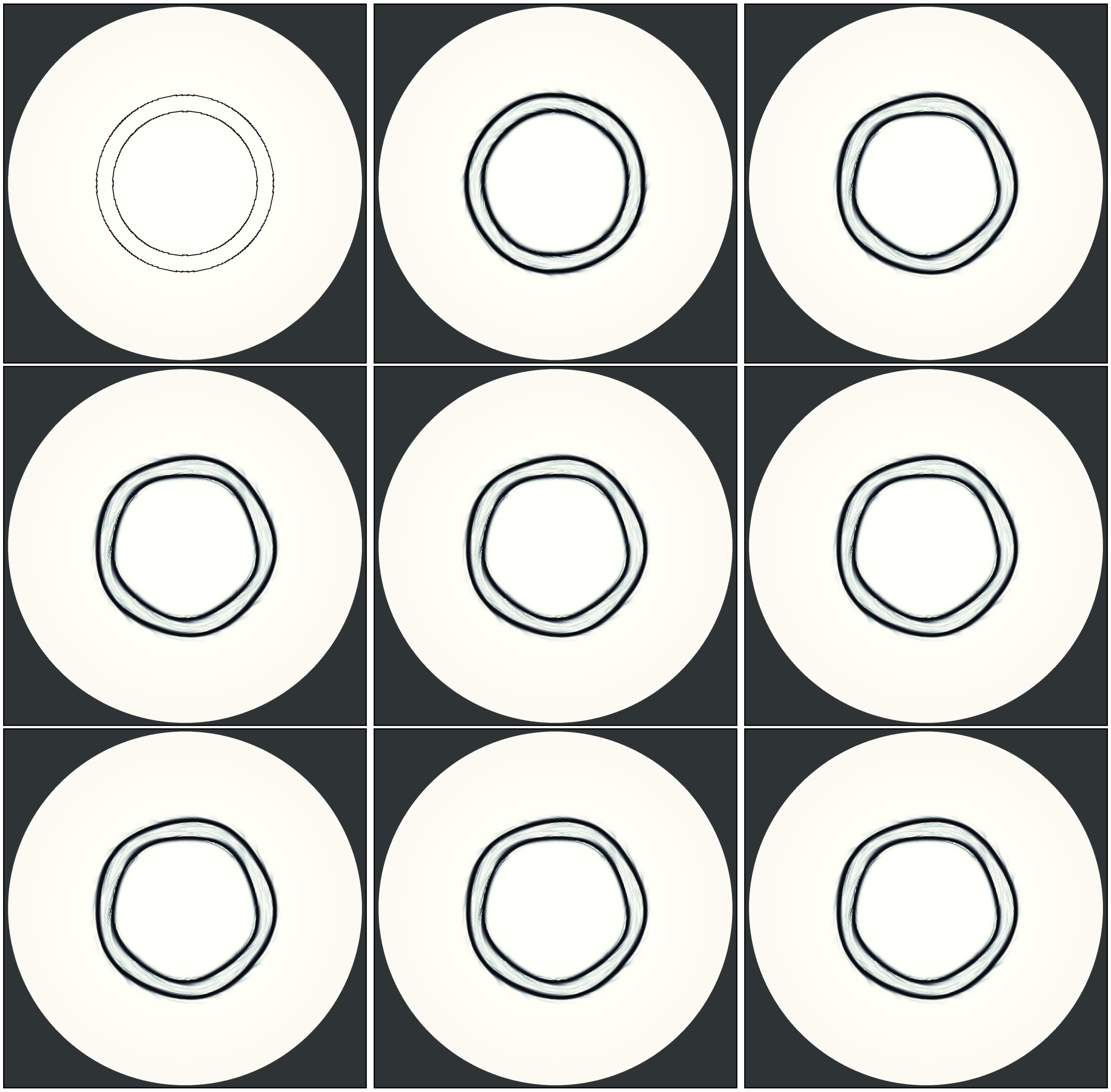

Figure 6-5 Crank-Nicolson. Schlieren snapshots 0, 200, 400, 600, 800, 1,000, 1,200, 1,400, and 1,600. Strictly speaking, these computations do not use Crank-Nicolson scheme but rather the θ-scheme with $\theta = 0.500001$. This computation uses a total of 399,770 time-steps: almost 14 times more time-steps than Backward-Euler or DIRK23 scheme. After snapshot 800 the scheme appears to produce highly defective numerical results: even though the fluid is still rotating, the electron density pattern stays in the same position. In other words, the interface between the annulus of electrons and the vacuum behaves like a 'stationary contact' or 'stationary internal layer'.

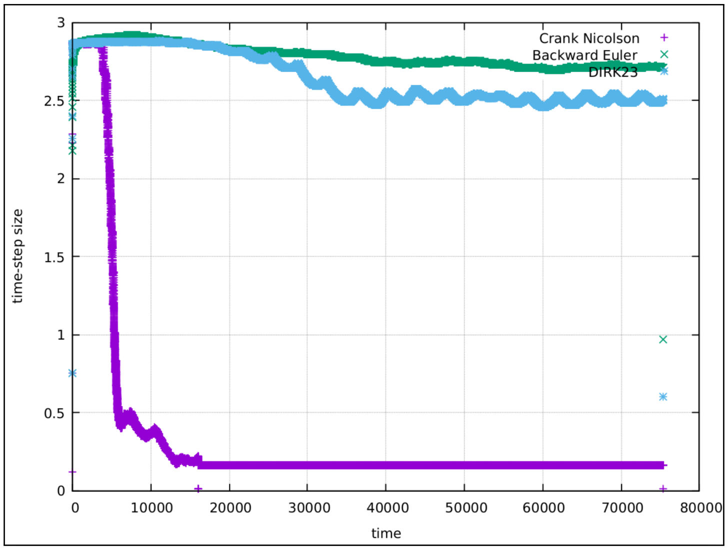

Figure 6-6 Time-step size evolution. Evolution of the time-step size along the simulation time: Crank-Nicolson (purple), Backward-Euler (green), and Crouzeix's DIRK23 (light blue). We can see that the time-step size of Crank-Nicolson is more than an order of magnitude smaller than that one required by either Backward-Euler or Crouzeix's scheme. On the other hand, we can appreciate that both Backward-Euler and Crouzeix's scheme display a quite stable time-step size throughout the entire simulation time.

solution is unlikely to preserve energy-stability.

- From the previous bullet we may be inclined to say that any attempt to develop a scheme that preserves both energy-stability and Gauss-law (stringently) is a roadmap for failure. Such goal, appears to be out of touch with the actual nature of the PDE. That is why at early stages of this project, when we started to design a scheme for the Euler-Poisson system, we decided to prioritize energy-stability over Gauss-law.
- Computational implementation of the 'idealized' or 'abstract' Gauss-law restart, as defined in (75) and (76), might not be computationally efficient. However, our early experiments using numerical implementations of simplified Gauss-law restart strategies, such as Algorithm 5, are quite promising, see Figure 6-7.

At this point in time, we have largely drifted away from the specifics advanced in Algorithm 5. We do not report such schemes due to limitations of time. Such schemes were tested in the shocked-regime (i.e., discontinuous solutions) leading to early results where *full-restart* and *line-search* restart were nearly indistinguishable. Overall, addressing the preservation of the Gauss law as a post-processing stage, rather than a property built-in to the scheme, appears to be technically sound and very promising.

6.6. Computational study #3: dependence on small parameter δ.

We consider the setup described by (55)-(60) with fixed value $\upsilon = 10^{-5}$, but develop a parametric study on δ. More precisely, we consider $\delta = 10^{-2}, 10^{-3}, 10^{-4}, 10^{-5}$. From (56), we know that

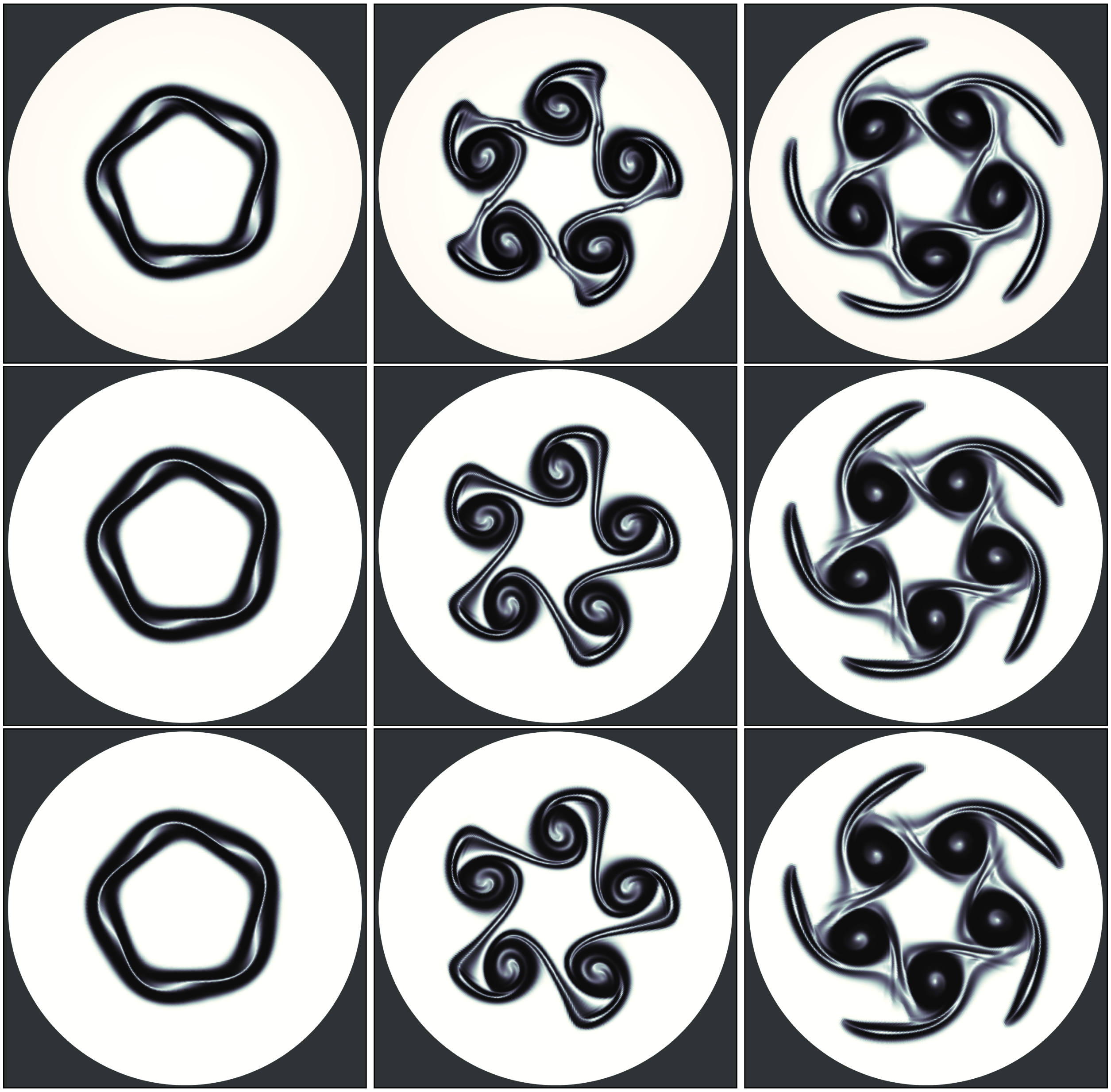

Figure 6-7 Gauss-law restart: visual comparison. Schlieren snapshots 500 (left), 1,000 (middle), 1,500 (right). There are approximately 7,000 time-steps between snapshot 500 and 1,000, and between snapshots 1,000 and 1,500. These snapshots correspond with: no Gauss-law restart (top row), line-search Gauss-law restart (middle row), and full Gauss-law restart (bottom row). We note that the differences between the last two rows are almost imperceptible under visual inspection, suggesting that the line-search Gauss-law restart as described in Algorithm 5 does exactly what we need. Regarding the first row (no restart), we notice that Snapshot 1,000 and 1,500 have some additional features/kinks that do not appear with any of the other two Gauss-law restart techniques. It is worth mentioning that running the scheme with no Gauss-law restart (at all) is never intended or suggested. Still, the baseline second-order scheme, without no Gauss-law restart, seems to be pretty good at preserving major features of the flow, even after 7,000 time-steps (as shown in the first column), which is rather remarkable.

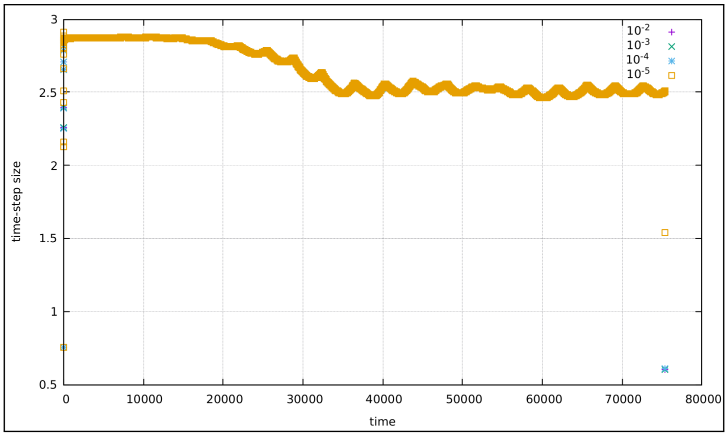

Figure 6-8 Time vs time-step: parametric study on δ. We consider the cases of $\delta = 10^{-2}$, $\delta = 10^{-3}$, $\delta = 10^{-4}$, $\delta = 10^{-5}$. The curves are literally on top of each other. These four cases use (exactly) 28,651 time steps. For reference, for the case of $\delta = 10^{-5}$, which is the most severe, the initial plasma period is $T_p = 6.28 \cdot 10^{-5}$, while the cyclotron period is $T_c = 6.28 \cdot 10^{-13}$, and the average time step size is $\tau \approx 2.6$ as it can be appreciated in the plot. That is: we are overstepping the plasma period by six-orders of magnitude, while we are overstepping the cyclotron period by almost fifteen orders of magnitude. Hopefully, this is enough to illustrate that the proposed scheme is indeed capable to overstepping high-frequency oscillatory phenomena without exhibiting degradation of its performance.

gradually smaller values of δ will lead to smaller electron masses m_e, and smaller electrical permittivity ε. The compounded effect of both constants going to zero is a dramatic growth of the plasma and cyclotron angular frequencies. From a dynamic point of view, this will make electrostatic forces more violent and will lead to sharper accelerations.

Our initial expectation was to observe a severe degradation of the time-step size, or at least, experience a major loss of the time-step size stability throughout the simulation time. Similarly, we were expecting a qualitative picture severely polluted by convective-like numerical instabilities. However, none of that happened. Regarding time-step size stability, the reader can check Figure 6-8 comparing the evolution of the time-step size for the different values of δ. As with all the computations presented in this report, the time-step size is solely determined by the hyperbolic *cfl*, and within such limitations, the number of time-steps remains pretty much constant (i.e. independent of the value of δ). Regarding qualitative picture, the reader can take a look at Figure 6-9 using $\delta = 10^{-5}$.

6.7. Computational study #4: dependence on small parameter υ.

We consider the setup described by (55)-(60) with fixed value $\delta = 10^{-2}$, but explore a parametric study on υ. More precisely we will consider using $\upsilon = 10^{-5}$, $\upsilon = 10^{-7}$, $\upsilon = 10^{-9}$, $\upsilon = 10^{-11}$ (almost a trillionth). From (55)-(60), we know that υ determines the strength of the vacuum conditions outside the annulus of negative electric charge and the plasma temperature. In Figure 6-10 we can see some results showing the history of the time-step size for each value of υ. Essentially, as we use stronger vacuum and lower temperatures the scheme is capable of using

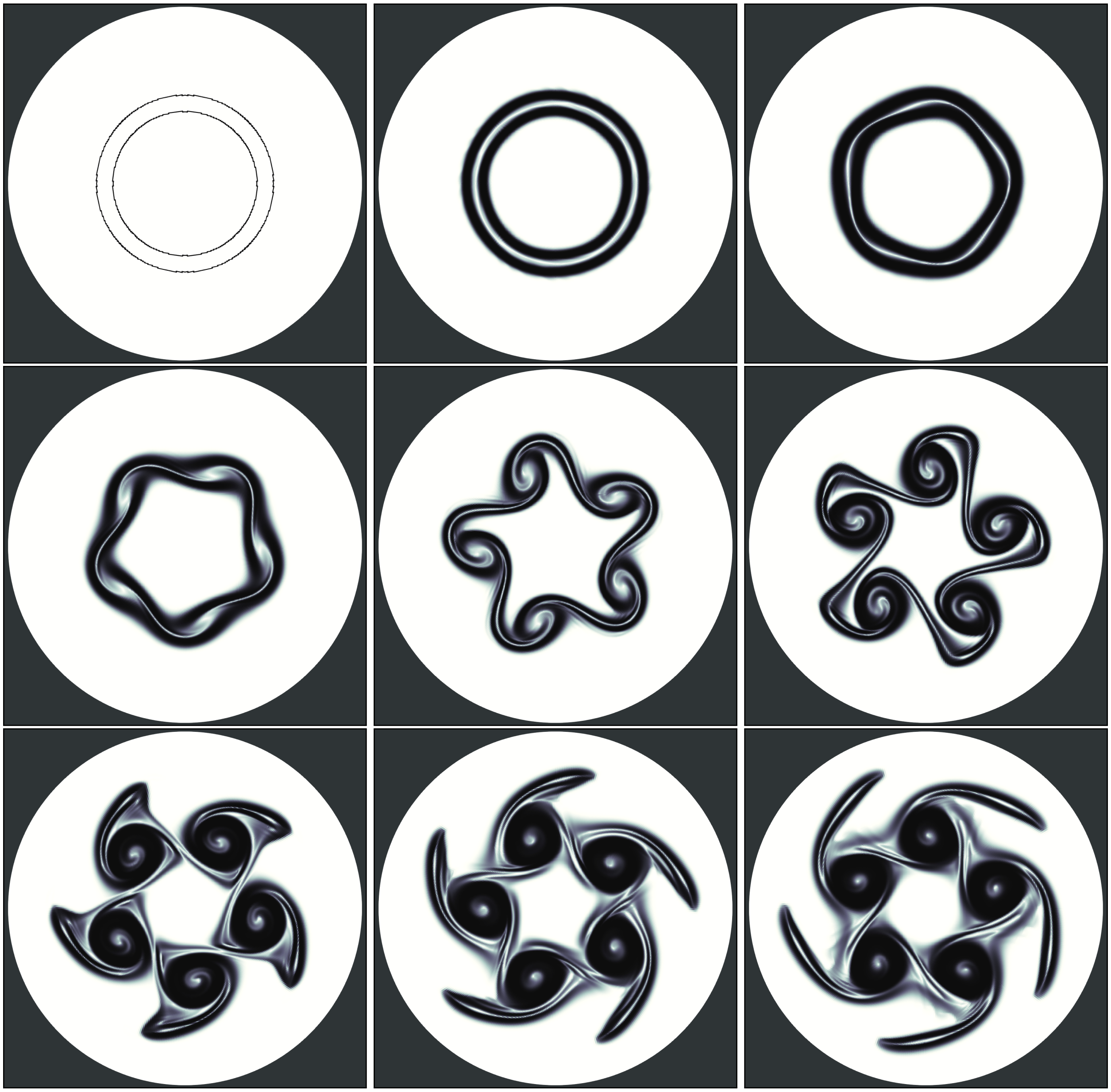

Figure 6-9 DIRK23 scheme using $\delta = 10^{-5}$. Using this value of δ we obtain $T_p \approx 6.28 \cdot 10^{-5}$, $T_c \approx 6.28 \cdot 10^{-13}$ and $T_d \approx 12566$, and the average time step size is $\tau \approx 2.6$ (see Figure 6-8). These results appear to be qualitatively right with no major questionable features. Note that there is, in principle, no good reason to think that these results should resemble those of Figure 6-4 using $\delta = 10^{-2}$. Their similarity appears to be just a happy consequence of the choice of scaling.

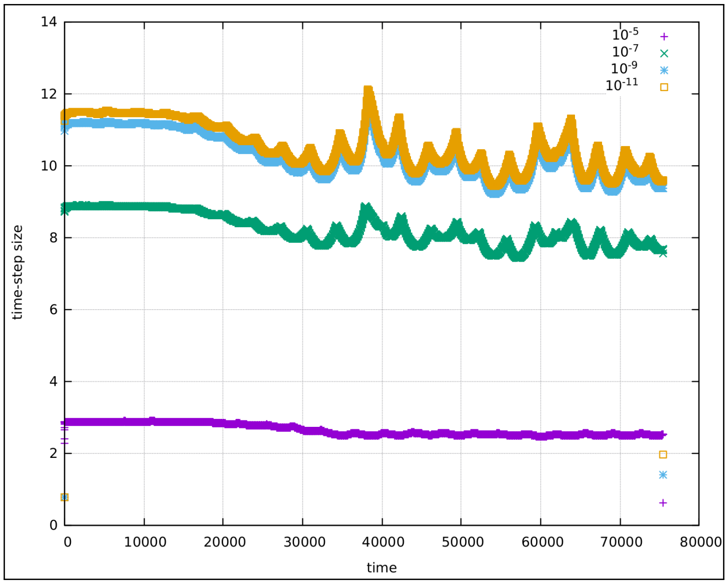

Figure 6-10 Time vs. time-step size: parametric study on υ. In this plot we consider, from lowest to highest location in the plot: $\upsilon = 10^{-5}$ (bottom purple curve), $\upsilon = 10^{-7}$, $\upsilon = 10^{-9}$ $\upsilon = 10^{-11}$ (top yellow curve). The most important observation is that, regardless of the density contrast-ratio, the time-step appears to be stable throughout the entire simulation time. For reference: bottom curve, corresponding with $\upsilon = 10^{-5}$ uses a total of 28,651 time-steps; while top curve, corresponding with $\upsilon = 10^{-11}$ uses merely 7,178 time-steps. Generally speaking, the scheme excels as we use stronger vacuum conditions and lower temperatures (i.e. $\upsilon \to 0^+$ in the context of (55)-(60)). Part of this behavior can be explained looking at the maximum speed of propagation of the hyperbolic subsystem. For the isothermal Euler-Poisson system we have that $\lambda_{\max} \approx u + \sqrt{\theta}$, where u is a material velocity while $\sqrt{\theta}$ is the sound speed. Clearly for smaller values υ we will get smaller sound speeds, which allows to use larger time-step sizes.

larger time-step sizes. In Figure 6-11 we can see some Schlieren screenshots corresponding to the most extreme case using $\upsilon = 10^{-11}$.

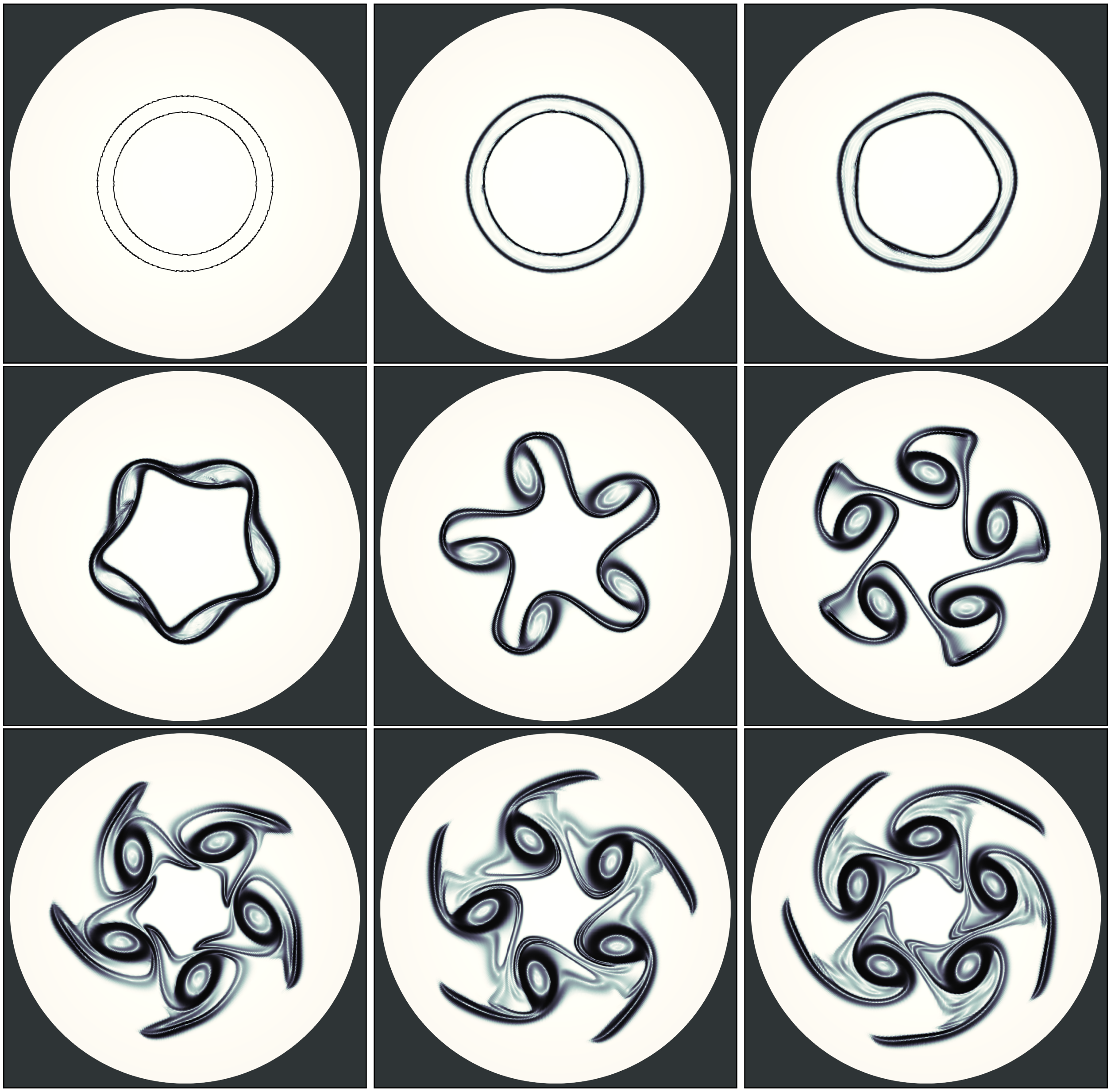

Figure 6-11 Computational results for the case of $\upsilon = 10^{-11}$. Snapshots 0, 200, 400, 600, 800, 1,000, 1,200, 1,400, and 1,600. This is a rather extreme computation with a density contrast-ratio of almost a trillion. Snapshots 600 and 800 show some jagged features. These computations used *cfl* $= 0.75$, which is somewhat too aggressive: using a smaller *cfl* removes these defects. Nonetheless we decided to present the current results 'as they are' in order to make meaningful comparison without resorting to any case-by-case tweaking. Beyond that, there are appears to be no other (evident to the naked) eye numerical issue. Note that there is no good reason to think that the results of this Figure should be comparable with those of Figure 6-2. The results of the current figure model a very cold plasma with temperature $\theta = 10^{-11}$, therefore acoustic waves are negligible. On the other hand, the results of Figure 6-2 use $\theta = 10^{-5}$, and while acoustic waves do not play a dominant role, they are non-negligible.

7. CONCLUSION

This report introduces a semi-implicit scheme for the isothermal Euler-Poisson system with a given magnetic field. The scheme splits the purely hyperbolic terms from the source-terms, see Section 4. The source terms couple implicitly the momentum and the potential. Fully implicit coupling between momentum and potential appears to be the minimal degree coupling we can introduce if we want to develop schemes that can overstep electrostatic plasma and cyclotron oscillation without suffering any degradation of the time-step size or numerical stability. The choice of splitting allowed us to isolate concerns, such as positivy preservation, since the hyperbolic subsystem can be solved with numerical schemes with mathematical guarantees of robustness. We note that in this context the magnetic field is ‘given data’, and assumed to be ‘constant’ or ‘frozen in-time’, this is however, perfectly compatible with second-order accuracy, see [83, Section 3.4].

The source-update scheme was implemented using statically condensed Schur-complements. In other words, we avoided blocked DOF-managers and blocked linear algebra in their entirety. This leads to a linear algebra system that is not that different from that one encountered when solving a scalar Poisson equation. Static condensation is by no means a new idea. However we believe that its application in the current context, PDE-ODE coupling, is an original technique, see Section 4.4 for more details.

Minimal conditions for entropy stability were introduced. The conditions seem to indicate that entropy production does not only depend on the choice of scheme used for the hyperbolic subsystem but also on the choice of time-integration scheme used for the source-update scheme. Our initial assessment is that vanishing-damping mechanisms appear to be of critical importance in order to recover entropic (i.e. physically valid) solutions. See Sections 5 and 6.4 for more details.

The scheme was tested in the high magnetic drift-regime, in order to approximate the solution of the guiding center drift-model. In order to prove preliminary concepts we chose the cold-plasma Diocotron instability, see Section 6.2. Our early numerical investigation provides quite strong computational evidence indicating that Crank-Nicolson scheme (for the source update scheme) has very little to no potential of working in the context of magnetic drift-regimes. This prompted us to develop an entire mathematical framework for Diagonally Implicit Runge-Kutta methods that satisfy a discrete energy law. The resulting scheme was shown to be capable of overstepping electrostatic plasma and cyclotron oscillations by several orders of magnitude, while also requiring a very modest number of time steps in order to complete simulations. Similarly, the scheme was also shown to be capable of working in the context of very large density contrast ratios (i.e. strong vacuum conditions). See Section 6 for more details.

The standard scheme does not preserve the Gauss-law exactly. However, the Gauss-law appears to be satisfied with very high-accuracy. This opened the possibility of recovering the preservation of the Gauss-law using simple but effective postprocessing techniques. These are early attempts in this direction: at this point in time, oversimplistic post-processing techniques are advanced in this report. Nonetheless, these initial attempts are promising, delivering results which are nearly indistinguishable from numerical solutions which are fully compliant with the Gauss law, see Section 6.5 for more details.

REFERENCES

[1] Roger Alexander. Diagonally implicit Runge-Kutta methods for stiff o.d.e.'s. *SIAM J. Numer. Anal.*, 14(6):1006–1021, 1977.

[2] Naoufel Ben Abdallah and Raymond El Hajj. Diffusion and guiding center approximation for particle transport in strong magnetic fields. *Kinet. Relat. Models*, 1(3):331–354, 2008.

[3] Sylvie Benzoni-Gavage and Denis Serre. *Multidimensional hyperbolic partial differential equations*. Oxford Mathematical Monographs. The Clarendon Press, Oxford University Press, Oxford, 2007. First-order systems and applications.

[4] C. Besse, P. Degond, Hj. Hwang, and R. Poncet. Nonlinear instability of the two-dimensional striation model about smooth steady states. *Comm. Partial Differential Equations*, 32(7-9):1017–1041, 2007.

[5] Christophe Besse, Pierre Degond, Fabrice Deluzet, Jean Claudel, Gérard Gallice, and Christian Tessieras. A model hierarchy for ionospheric plasma modeling. *Math. Models Methods Appl. Sci.*, 14(3):393–415, 2004.

[6] J. A. Bittencourt. *Fundamentals of plasma physics*. Pergamon Press, Oxford, 1986.

[7] Daniele Boffi, Franco Brezzi, and Michel Fortin. *Mixed finite element methods and applications*, volume 44 of *Springer Series in Computational Mathematics*. Springer, Heidelberg, 2013.

[8] John H Booske, Mark A Basten, AH Kumbasar, Thomas M Antonsen Jr, Steven W Bidwell, Yuval Carmel, William W Destler, Victor L Granatstein, and Daniel J Radack. Periodic magnetic focusing of sheet electron beams. *Physics of plasmas*, 1(5):1714–1720, 1994.

[9] Allen H Boozer. Guiding center drift equations. *The Physics of Fluids*, 23(5):904–908, 1980.

[10] Mihai Bostan. The Vlasov-Maxwell system with strong initial magnetic field: guiding-center approximation. *Multiscale Model. Simul.*, 6(3):1026–1058, 2007.

[11] Stéphane Brull, Pierre Degond, Fabrice Deluzet, and Alexandre Mouton. Asymptotic-preserving scheme for a bi-fluid Euler-Lorentz model. *Kinet. Relat. Models*, 4(4):991–1023, 2011.

[12] Stéphane Brull, Pierre Degond, Fabrice Deluzet, and Alexandre Mouton. Asymptotic-preserving scheme for a bi-fluid Euler-Lorentz model. *Kinet. Relat. Models*, 4(4):991–1023, 2011.

[13] Xiaofeng Cai, Wei Guo, and Jing-Mei Qiu. A high order semi-Lagrangian discontinuous Galerkin method for the two-dimensional incompressible Euler equations and the guiding center Vlasov model without operator splitting. *J. Sci. Comput.*, 79(2):1111–1134, 2019.

[14] Francis F Chen et al. *Introduction to plasma physics and controlled fusion*, volume 1. Springer, 1984.

[15] HC Chen and HS Uhm. Diocotron instability of an intense relativistic electron beam in an accelerator. *Physical Review A*, 32(3):1657, 1985.

[16] Andrew Christlieb, Wei Guo, Maureen Morton, and Jing-Mei Qiu. A high order time splitting method based on integral deferred correction for semi-Lagrangian Vlasov simulations. *J. Comput. Phys.*, 267:7–27, 2014.

[17] Bernardo Cockburn. Static condensation, hybridization, and the devising of the HDG methods. In *Building bridges: connections and challenges in modern approaches to numerical partial differential equations*, volume 114 of *Lect. Notes Comput. Sci. Eng.*, pages 129–177. Springer, [Cham], 2016.

[18] Pierre Crispel, Pierre Degond, and Marie-Hélène Vignal. An asymptotic preserving scheme for the two-fluid Euler-Poisson model in the quasineutral limit. *J. Comput. Phys.*, 223(1):208–234, 2007.

[19] Michael Crockatt and John Shadid. Development, implementation, and verification of partially-ionized collisional multifluid plasma models in drekar. *OSTI*, 6 2021.

[20] Michael M. Crockatt, Sibusiso Mabuza, John N. Shadid, Sidafa Conde, Thomas M. Smith, and Roger P. Pawlowski. An implicit monolithic afc stabilization method for the cg finite element discretization of the fully-ionized ideal multifluid electromagnetic plasma system. *Journal of Computational Physics*, 2022. (accepted).

[21] Michel Crouzeix. Sur la B-stabilité des méthodes de Runge-Kutta. *Numer. Math.*, 32(1):75–82, 1979.

[22] Constantine M. Dafermos. *Hyperbolic conservation laws in continuum physics*, volume 325 of *Grundlehren der mathematischen Wissenschaften [Fundamental Principles of Mathematical Sciences]*. Springer-Verlag, Berlin, 2000.

[23] Ronald C Davidson. *Physics of nonneutral plasmas*. World Scientific Publishing Company, 2001.

[24] Ronald C Davidson and Gian Marco Felice. Influence of profile shape on the diocotron instability in a non-neutral plasma column. *Physics of Plasmas*, 5(10):3497–3511, 1998.

[25] Alexandra De Cecco, Fabrice Deluzet, Claudia Negulescu, and Stefan Possanner. Asymptotic transition from kinetic to adiabatic electrons along magnetic field lines. *Multiscale Model. Simul.*, 15(1):309–338, 2017.

[26] P. Degond. Asymptotic-preserving schemes for fluid models of plasmas. In *Numerical models for fusion*, volume 39/40 of *Panor. Synthèses*, pages 1–90. Soc. Math. France, Paris, 2013.

[27] P. Degond, F. Deluzet, A. Sangam, and M.-H. Vignal. An asymptotic preserving scheme for the Euler equations in a strong magnetic field. *J. Comput. Phys.*, 228(10):3540–3558, 2009.

[28] Pierre Degond and Fabrice Deluzet. Asymptotic-preserving methods and multiscale models for plasma physics. *J. Comput. Phys.*, 336:429–457, 2017.

[29] Fabrice Deluzet, Maurizio Ottaviani, and Stefan Possanner. A drift-asymptotic scheme for a fluid description of plasmas in strong magnetic fields. *Comput. Phys. Commun.*, 219:164–177, 2017.

[30] G. L. Delzanno, J. M. Finn, and G. Lapenta. Nonlinear phase of the compressional $m = 1$ diocotron instability: saturation and analogy with geophysical fluid dynamics. *Phys. Plasmas*, 9(12):5059–5069, 2002.

[31] V. Dobrev, T. Kolev, C. S. Lee, V. Tomov, and P. S. Vassilevski. Algebraic hybridization and static condensation with application to scalable $H(\mathrm{div})$ preconditioning. *SIAM J. Sci. Comput.*, 41(3):B425–B447, 2019.

[32] Alexandre Ern and Jean-Luc Guermond. *Theory and practice of finite elements*, volume 159

of *Applied Mathematical Sciences*. Springer-Verlag, New York, 2004.

[33] Lawrence C. Evans. *Partial differential equations*, volume 19 of *Graduate Studies in Mathematics*. American Mathematical Society, Providence, RI, 1998.

[34] Francis Filbet and Shi Jin. A class of asymptotic-preserving schemes for kinetic equations and related problems with stiff sources. *J. Comput. Phys.*, 229(20):7625–7648, 2010.

[35] Francis Filbet and Charles Prouveur. High order time discretization for backward semi-Lagrangian methods. *J. Comput. Appl. Math.*, 303:171–188, 2016.

[36] Francis Filbet and Luis Miguel Rodrigues. Asymptotically stable particle-in-cell methods for the Vlasov-Poisson system with a strong external magnetic field. *SIAM J. Numer. Anal.*, 54(2):1120–1146, 2016.

[37] Francis Filbet, Tao Xiong, and Eric Sonnendrücker. On the Vlasov-Maxwell system with a strong magnetic field. *SIAM J. Appl. Math.*, 78(2):1030–1055, 2018.

[38] E. Frénod and E. Sonnendrücker. Long time behavior of the two-dimensional Vlasov equation with a strong external magnetic field. *Math. Models Methods Appl. Sci.*, 10(4):539–553, 2000.

[39] Emmanuel Frénod, Sever A. Hirstoaga, Mathieu Lutz, and Eric Sonnendrücker. Long time behaviour of an exponential integrator for a Vlasov-Poisson system with strong magnetic field. *Commun. Comput. Phys.*, 18(2):263–296, 2015.

[40] Emmanuel Frénod and Eric Sonnendrücker. Homogenization of the Vlasov equation and of the Vlasov-Poisson system with a strong external magnetic field. *Asymptot. Anal.*, 18(3-4):193–213, 1998.

[41] François Golse and Laure Saint-Raymond. The Vlasov-Poisson system with strong magnetic field. *J. Math. Pures Appl. (9)*, 78(8):791–817, 1999.

[42] François Golse and Laure Saint-Raymond. The Vlasov-Poisson system with strong magnetic field. *J. Math. Pures Appl. (9)*, 78(8):791–817, 1999.

[43] Laurent Gosse and Giuseppe Toscani. An asymptotic-preserving well-balanced scheme for the hyperbolic heat equations. *C. R. Math. Acad. Sci. Paris*, 334(4):337–342, 2002.

[44] Sigal Gottlieb, Chi-Wang Shu, and Eitan Tadmor. Strong stability-preserving high-order time discretization methods. *SIAM Rev.*, 43(1):89–112, 2001.

[45] Leslie Greengard and Shidong Jiang. A new mixed potential representation for unsteady, incompressible flow. *SIAM Rev.*, 61(4):733–755, 2019.

[46] Christian Grossmann and Hans-Görg Roos. *Numerical treatment of partial differential equations*. Universitext. Springer, Berlin, 2007. Translated and revised from the 3rd (2005) German edition by Martin Stynes.

[47] Jean-Luc Guermond, Martin Kronbichler, Matthias Maier, Bojan Popov, and Ignacio Tomas. On the implementation of a robust and efficient finite element-based parallel solver for the compressible Navier-Stokes equations. *Comput. Methods Appl. Mech. Engrg.*, 389:Paper No. 114250, 26, 2022.

[48] Jean-Luc Guermond, Matthias Maier, Bojan Popov, and Ignacio Tomas. Second-order invariant domain preserving approximation of the compressible Navier-Stokes equations. *Comput. Methods Appl. Mech. Engrg.*, 375:Paper No. 113608, 17, 2021.

[49] Jean-Luc Guermond, Murtazo Nazarov, Bojan Popov, and Ignacio Tomas. Second-order

invariant domain preserving approximation of the Euler equations using convex limiting. *SIAM J. Sci. Comput.*, 40(5):A3211–A3239, 2018.

[50] Jean-Luc Guermond and Bojan Popov. Viscous regularization of the Euler equations and entropy principles. *SIAM J. Appl. Math.*, 74(2):284–305, 2014.

[51] Jean-Luc Guermond and Bojan Popov. Invariant domains and first-order continuous finite element approximation for hyperbolic systems. *SIAM J. Numer. Anal.*, 54(4):2466–2489, 2016.

[52] Jean-Luc Guermond and Bojan Popov. Invariant domains and second-order continuous finite element approximation for scalar conservation equations. *SIAM J. Numer. Anal.*, 55(6):3120–3146, 2017.

[53] Jean-Luc Guermond, Bojan Popov, and Ignacio Tomas. Invariant domain preserving discretization-independent schemes and convex limiting for hyperbolic systems. *Comput. Methods Appl. Mech. Engrg.*, 347:143–175, 2019.

[54] Adnane Hamiaz, Michel Mehrenberger, Aurore Back, and Pierre Navaro. Guiding center simulations on curvilinear grids. In *CEMRACS 2014—numerical modeling of plasmas*, volume 53 of *ESAIM Proc. Surveys*, pages 99–119. EDP Sci., Les Ulis, 2016.

[55] N. D. Hamlin and C. E. Seyler. The influence of hall physics on power-flow along a coaxial transmission line. *Physics of Plasmas*, 25(10):102705, 2018.

[56] Daniel Han-Kwan. Effect of the polarization drift in a strongly magnetized plasma. *ESAIM Math. Model. Numer. Anal.*, 46(4):929–947, 2012.

[57] Maxime Herda. On massless electron limit for a multispecies kinetic system with external magnetic field. *J. Differential Equations*, 260(11):7861–7891, 2016.

[58] Jiann-Sheng Jiang and Chi-Kun Lin. Guiding center drift induced by homogenization. *Math. Models Methods Appl. Sci.*, 22(5):1150027, 20, 2012.

[59] Shi Jin. Asymptotic preserving (AP) schemes for multiscale kinetic and hyperbolic equations: a review. *Riv. Math. Univ. Parma (N.S.)*, 3(2):177–216, 2012.

[60] YH Jo, JS Kim, G Stancari, Moses Chung, and Hae June Lee. Control of the diocotron instability of a hollow electron beam with periodic dipole magnets. *Physics of Plasmas*, 25(1):011607, 2018.

[61] Ansgar Jüngel. *Entropy methods for diffusive partial differential equations*. SpringerBriefs in Mathematics. Springer, [Cham], 2016.

[62] IN Kartashov and MV Kuzelev. Nonlinear dynamics of diocotron instability. *Plasma Physics Reports*, 36(6):524–532, 2010.

[63] C.A. Kennedy and M.H. Carpenter. *Diagonally Implicit RungeâĂŞKutta Methods for Ordinary Differential Equations: A Review*. NASA Langley Research Center, 2016.

[64] Martin Kronbichler and Katharina Kormann. Fast matrix-free evaluation of discontinuous Galerkin finite element operators. *ACM Trans. Math. Software*, 45(3):Art. 29, 40, 2019.

[65] SA Kurkin, AA Badarin, AA Koronovskii, and AE Hramov. The development and interaction of instabilities in intense relativistic electron beams. *Physics of Plasmas*, 22(12):122110, 2015.

[66] Matthias Maier and Martin Kronbichler. Efficient parallel 3D computation of the compressible Euler equations with an invariant-domain preserving second-order

finite-element scheme. *ACM Trans. Parallel Comput.*, 8(3):Art. 16, 30, 2021.

[67] Matthias Maier and Ignacio Tomas. Step-69: graph-based solver for compressible Euler's system, 2020. DOI 10.5281/zenodo.3698223, https://www.dealii.org/current/doxygen/deal.II/step_69.html.

[68] Andrew J. Majda and Andrea L. Bertozzi. *Vorticity and incompressible flow*, volume 27 of *Cambridge Texts in Applied Mathematics*. Cambridge University Press, Cambridge, 2002.

[69] Michel Mehrenberger, Laura S. Mendoza, Charles Prouveur, and Eric Sonnendrücker. Solving the guiding-center model on a regular hexagonal mesh. In *CEMRACS 2014—numerical modeling of plasmas*, volume 53 of *ESAIM Proc. Surveys*, pages 149–176. EDP Sci., Les Ulis, 2016.

[70] K. W. Morton and D. F. Mayers. *Numerical solution of partial differential equations*. Cambridge University Press, Cambridge, second edition, 2005. An introduction.

[71] F. Mottez. A guiding centre direct implicit scheme for magnetized plasma simulations. *J. Comput. Phys.*, 227(6):3260–3281, 2008.

[72] Scott Christopher Neu and George J Morales. Computer simulation of the diocotron instability. In *AIP Conference Proceedings*, volume 331, pages 124–128. American Institute of Physics, 1995.

[73] J Pétri, J Heyvaerts, and S Bonazzola. Diocotron instability in pulsar electrospheres-i. linear analysis. *Astronomy & Astrophysics*, 387(2):520–530, 2002.

[74] Jérôme Pétri. The diocotron instability in a pulsar cylindrical electrosphere. *Astronomy and Astrophysics*, 464, 11 2006.

[75] Jérôme Pétri. Non-linear evolution of the diocotron instability in a pulsar electrosphere: two-dimensional particle-in-cell simulations. *Astronomy & Astrophysics*, 503(1):1–12, 2009.

[76] Xiangfan Piao, Philsu Kim, and Dojin Kim. One-step $L(\alpha)$-stable temporal integration for the backward semi-Lagrangian scheme and its application in guiding center problems. *J. Comput. Phys.*, 366:327–340, 2018.

[77] F. Poupaud, M. Rascle, and J.-P. Vila. Global solutions to the isothermal Euler-Poisson system with arbitrarily large data. *J. Differential Equations*, 123(1):93–121, 1995.

[78] Alfio Quarteroni and Alberto Valli. *Numerical approximation of partial differential equations*, volume 23 of *Springer Series in Computational Mathematics*. Springer-Verlag, Berlin, 1994.

[79] LLNL Rognlien, T. D. Influence of etimesb and nablaital B deift terms in 2-d edge/sol transport simulations. 5 1998.

[80] Laure Saint-Raymond. Control of large velocities in the two-dimensional gyrokinetic approximation. *J. Math. Pures Appl. (9)*, 81(4):379–399, 2002.

[81] Abner J. Salgado and Ignacio Tomas. Diagonally implicit Runge-Kutta schemes: Discrete energy-balance laws and compactness properties, Arxiv Preprint 2205.13032, 2022.

[82] Ignacio Tomas, Matthias Maier, and John Shadid. Structure preserving finite element schemes for the euler-poisson equations. *To be submitted to Communications in Computational Physics*, 2023.

[83] Ignacio Tomas, John Shadid, Michael Crockatt, Roger Pawlowski, Matthias Maier, and Jean-Luc Guermond. Final report of activities for the ldrd-express project #223796 titled:

Fluid models of charged species transport: numerical methods with mathematically guaranteed properties, PI: Ignacio Tomas, Co-PI: John Shadid. *OSTI*, 9 2021.

[84] Yu. A. Tsidulko. Two-dimensional dynamics of two-component plasma with finite β. *Phys. Plasmas*, 11(9):4420–4428, 2004.

[85] Tomáš Vejchodský and Pavel Šolín. Static condensation, partial orthogonalization of basis functions, and ILU preconditioning in the *hp*-FEM. *J. Comput. Appl. Math.*, 218(1):192–200, 2008.

[86] Tao Xiong, Giovanni Russo, and Jing-Mei Qiu. High order multi-dimensional characteristics tracing for the incompressible Euler equation and the guiding-center Vlasov equation. *J. Sci. Comput.*, 77(1):263–282, 2018.

[87] Chang Yang and Francis Filbet. Conservative and non-conservative methods based on Hermite weighted essentially non-oscillatory reconstruction for Vlasov equations. *J. Comput. Phys.*, 279:18–36, 2014.

[88] Yuichi Yatsuyanagi, Yasuhito Kiwamoto, Toshikazu Ebisuzaki, Tadatsugu Hatori, and Tomokazu Kato. Simulations of diocotron instability using a special-purpose computer, mdgrape-2. *Physics of Plasmas*, 10(8):3188–3195, 2003.

[89] Hongqiang Zhu, Jianxian Qiu, and Jing-Mei Qiu. An *h*-adaptive RKDG method for the two-dimensional incompressible Euler equations and the guiding center Vlasov model. *J. Sci. Comput.*, 73(2-3):1316–1337, 2017.

APPENDIX A. DISCRETE ENERGY-LAW OF THE CROUZEIX DIRK23 SCHEME

Let $\mathbb{W} \subseteq \mathbb{U} \subseteq \mathbb{W}^*$ be a Gelfand triple. Here $\mathbb{W}^*$ is the dual space of $\mathbb{W}$. The inner product between objects of the $\mathbb{U}$-space will be denoted as $(\cdot,\cdot)_{\mathbb{U}}$, therefore the corresponding norm will be denoted as $|\cdot|_{\mathbb{U}} = (\cdot,\cdot)_{\mathbb{U}}^{1/2}$. The duality pairing between $\mathbb{W}$ and $\mathbb{W}^*$ is denoted by $\langle\cdot,\cdot\rangle_{\mathbb{W}^*,\mathbb{W}}$. We are interested in solving the evolutionary problem $\partial_t u + \mathcal{F}(t,u) = 0$ where $\mathcal{F}(t,u) : \mathbb{R}\times\mathbb{W} \to \mathbb{W}^*$, therefore $\partial_t u \in \mathbb{W}^*$, with initial data $u_0 \in \mathbb{U}$, in the interval of time $[0,t_F]$ with $t_F > 0$. We assume the following additive structure for $\mathcal{F}(t,u)$ that separates the autonomous part from the non-autonomous component as

$$\mathcal{F}(t,u) := \mathcal{A}(u) - f(t) \tag{64}$$

where $\mathcal{A}(u) : \mathbb{W} \to \mathbb{W}^*$ is the autonomous part of $\mathcal{F}(t,u)$, and $f(t) : [0,t_F] \to \mathbb{W}^*$ is the non-autonomous part. In practice boundary-data can be assimilated into $f(t)$.

The Crouzeix's two-stage third-order scheme is described by the following tableau:

$$\begin{array}{c|cc} \frac{1}{2}+\gamma & \frac{1}{2}+\gamma & \\ \frac{1}{2}-\gamma & -2\gamma & \frac{1}{2}+\gamma \\ \hline & \frac{1}{2} & \frac{1}{2} \end{array} \quad \text{with } \gamma = \frac{\sqrt{3}}{6}. \tag{65}$$

This tableau appears for the first time in [21].

Remark A.1 (Implementation of DIRK schemes)**.** Tableau (65) translates into the following sequence of steps: given an initial state u_n at time t_n we compute u_{n+1} as follows:

$$\text{Stage \#1} \quad u_1 - u_n = -(\tfrac{1}{2}+\gamma)\tau\mathcal{F}(t_1,u_1) \tag{66}$$

$$\text{Stage \#2} \quad u_2 - u_n = 2\gamma\tau\mathcal{F}(t_1,u_1) - (\tfrac{1}{2}+\gamma)\tau\mathcal{F}(t_2,u_2) \tag{67}$$

$$\text{Final solution \#3} \; u_{n+1} - u_n = -\tfrac{1}{2}\tau\mathcal{F}(t_1,u_1) - \tfrac{1}{2}\tau\mathcal{F}(t_2,u_2) \tag{68}$$

where $t_1 = t_n + (\frac{1}{2}+\gamma)\tau$ and $t_2 = t_n + (\frac{1}{2}-\gamma)\tau$. Note that the operations described by (66)-(68) are uncoupled: we first compute u_1 by solving an implicit problem in (66), then we use the value of u_1 in order to compute u_2 using (67), and finally we compute the solution u_{n+1} using (68). However, (66)-(68) is not representative of how these methods are actually implemented. For instance, storage of the vectors $\mathcal{F}(t_1,u_1)$ and $\mathcal{F}(t_2,u_2)$ is not only cumbersome but also unnecessary. An algebraically equivalent implementation of (66)-(68) consists of:

$$\text{Stage \#1:} \; u_1 + (\tfrac{1}{2}+\gamma)\tau\mathcal{F}(t_1,u_1) = u_n \tag{69}$$

$$\text{Stage \#2:} \; u_2 + (\tfrac{1}{2}+\gamma)\tau\mathcal{F}(t_2,u_2) = \upsilon_{12}u_1 + (1-\upsilon_{12})u_n \tag{70}$$

$$\text{Final solution \#3:} \qquad u_{n+1} = \upsilon_n u_n + \upsilon_1 u_1 + \upsilon_2 u_2 \tag{71}$$

where $\upsilon_{12} = 1-\sqrt{3}$, $\upsilon_n = 1-\sqrt{3}$, $\upsilon_1 = \frac{3\sqrt{3}}{2} - \frac{3}{2}$ and $\upsilon_2 = \frac{3}{2} - \frac{\sqrt{3}}{2}$. In the context of (69)-(71) it is clear that the DIRK23 scheme consists in two calls to a Backward-Euler solver, each time with different initial data, and a final linear extrapolation step. In other words: Backward-Euler should be understood as a separate routine/method. This small observation usually leads to better code organization.

The Crouzeix scheme is of one many so-called Diagonally Implicit Runge-Kutta schemes [1, 63], usually called DIRK-schemes for short. These kind of schemes have existed for quite a while, however their stability analysis is mostly to limited perturbative theories of stability. However, Crouzeix's scheme is quite special, in particular, since it satisfies a dissipative discrete energy-balance as detailed in the following lemma.

Lemma A.1. *Crouzeix's scheme, satisfies the following discrete energy-balance:*

$$\tfrac{1}{2}|u_{n+1}|_{\mathbb{U}}^2 + Q(u_n,u_1,u_2) + \tau\nu_1\langle\mathcal{F}(u_1),u_1\rangle_{\mathbb{W}^*,\mathbb{W}} + \tau\nu_2\langle\mathcal{F}(u_2),u_2\rangle_{\mathbb{W}^*,\mathbb{W}} = \tfrac{1}{2}|u_n|^2\,, \tag{72}$$

where $\nu_1 = \frac{1}{2}$, $\nu_2 = \frac{1}{2}$, *and* $Q(u,v,w) : \mathbb{H}\times\mathbb{H}\times\mathbb{H}\to\mathbb{R}$ *is positive semi-definite homogeneous of degree-2 quadratic form given by*

$$Q(u_n,u_1,u_2) := \left[\delta_1|u_1-u_n|_{\mathbb{U}}^2 + \delta_2|u_2-u_1|_{\mathbb{U}}^2 + \delta_{12}(u_1-u_n,u_2-u_1)_{\mathbb{U}}\right]. \tag{73}$$

with

$$\delta_1 = \sqrt{3}-\tfrac{3}{2}\,,\ \delta_2 = \tfrac{\sqrt{3}}{4}\ \text{ and }\ \delta_{12} = \tfrac{3}{2}-\tfrac{\sqrt{3}}{2}\,. \tag{74}$$

The proof of this lemma is rather non-trivial and goes well-beyond the context of this LDRD-project. Such proof is part of a separate body of mathematical research containing more general mathematical results in relationship to DIRK schemes, see arXiv pre-print [81]. We highlight that energy-identity (72)-(74) constitutes, by itself, an original result advanced specifically for the purposes addressed in this report.

APPENDIX B. GAUSS-LAW RESTART

Given a pair of electron number density n_e^n and potential φ^n returned by the call of Algorithm 1, for the case of guiding center drift-limit model, or Algorithm 4 for the case of Euler-Poisson model, in general we have that Gauss-law $-\varepsilon\Delta\varphi^n = q_e n_e^n + q_b n_b^n$ will not hold true. We say that a a 'Gauss-law restart' is any mathematical procedure that recovers either partial or total compliance with the Gauss-law while also preserving energy-stability property (21) for the case of Drift-limit model, or entropy-stability property (51) for the case of isothermal Euler-Poisson system. We may think of 'Gauss-law restart' as a post-processing technique that requires solving a constrained optimization problem. Therefore, we may want to find a new potential $\widehat{\varphi}^n$ defined as

$$\widehat{\varphi}^n = \underset{\{\varphi\in H^1(\Omega)\,|\,\|\nabla\varphi\|_{L^2(\Omega)}\leq\kappa\}}{\operatorname{argmin}} \|\varepsilon\Delta\varphi + q_e n_e^n + q_b n_b^n\|_{H^s(\Omega)}\,, \tag{75}$$

where $s\in\mathbb{R}$ and $\kappa\geq 0$ is a prescribed value. This begs quite a few questions: How can we devise such procedure? How can we make it inexpensive? What is the proper choice of norm $H^s(\Omega)$? More generally what is the proper functional-analytic framework in order to make problem (75) well-posed? What is the proper value of κ? Is it feasible to devise such procedure without spoiling the accuracy properties of Marchuk-Strang splitting scheme? However, the context of this narrowly-scoped LDRD-project, our goal is not to attempt to advance, develop or promote any optimal Gauss-law restart methodology. For the purposes of this manuscript, the primary goal is to devise the simplest and most inexpensive technique that allows us to enforce preservation of the Gauss-law either in whole or in part. The utilitarian purpose of such technique is to use it in order to evaluate the robustness and sensitivity of the numerical results with respect to the preservation (or violation) of the Gauss-law.

The proper choice of norm in (75) appears to be $H^s(\Omega)$ with $s=-1$. In this context (75) can be rewritten as

$$\widehat{\varphi}^{n+1} = \underset{\{\varphi\in H^1(\Omega)\,|\,\|\nabla\varphi\|_{L^2(\Omega)}\leq\kappa\}}{\operatorname{argmin}} \|\nabla\varphi - \nabla\varphi_g\|_{L^2(\Omega)}\,, \tag{76}$$

where φ_g is the solution of $-\varepsilon\Delta\varphi_g = q_e n_e^n + q_b n_b^n$. On the other hand, κ should be understood as a 'energy budget' that we are not allowed to violate. If we set $\kappa = \|\nabla\varphi^n\|_{L^2(\Omega)}$, we will guarantee that the Gauss-law restart does not spoil the entropy/energy stability properties of Marchuk-Strang splitting. In other words: forcefully replacing φ^n with φ_g^n will preserve stability of the scheme provided that $\|\nabla\varphi_g^n\|_{L^2(\Omega)} \leq \|\nabla\varphi^n\|_{L^2(\Omega)}$. However, if we use a dissipative scheme for the source-update scheme, we may pick-up the energy lost during the source update scheme and add it to κ in order to 'enlarge our energy budget'. For instance, in the context of isothermal Euler-Poisson system, if we use DIRK23 scheme in order to compute the source-update, we may consider setting

$$\kappa = \big(\|\nabla\varphi^{n+1}\|_{L^2(\Omega)}^2 + \frac{2}{\varepsilon}\mathcal{Q}(\mathbf{u}_h^n, \mathbf{u}_h^1, \mathbf{u}_h^2)\big)^{\frac{1}{2}}$$

where $\mathcal{Q}(\mathbf{u}_h^n, \mathbf{u}_h^1, \mathbf{u}_h^2)$ was defined in (36). This is perfectly compatible with energy-stability.

We will consider the following algorithm in order to restart the Gauss-law:

Algorithm 5 `line_search_gauss_law_restart`$(\{n_e, n_b, \varphi, \kappa\})$

```
◇ Step #1 (projection): compute $\varphi_g$ solution of $-\varepsilon\Delta\varphi_g = q_e n_e + q_b n_b$.
◇ Step #2 (line-search): compute $\lambda$ defined as
      $\lambda := \max\big\{s \in [0,1] \,\big|\, \|s\nabla\varphi_g - (1-s)\nabla\varphi\|_{L^2(\Omega)} \leq \kappa\big\}$.
◇ Step #3 (linear combination): set $\widehat{\varphi} := \lambda\varphi_g + (1-\lambda)\varphi$
Return: $\widehat{\varphi}$
```

Regarding the accuracy of Algorithm 5 we have compelling mathematical arguments in order to believe that it will not spoil the accuracy of the scheme. In what follows, Lemma B.1, Lemma B.2, and finally Proposition B.1, provide some comfort proving that $\widehat{\varphi}$, as defined in Step #3 of Algorithm 5, will preserve the accuracy of the scheme. We start with Lemma B.1 which establishes that if the scheme is sufficiently accurate, Gauss-law should exhibit a decay rate in dual-norm, even if Gauss-law is not strictly enforced by the scheme.

Lemma B.1 (Gauss-law-residual estimate)**.** *Let n_e^n and φ^n represent the solutions returned by a numerical scheme of q-th order of accuracy, meaning that it satisfies a formal error estimate of the form*

$$\varepsilon\|\nabla\varphi(t^n)-\nabla\varphi^n\|_{L^2(\Omega)}+q_e\|n_e(t^n)-n_e^n\|_{L^2(\Omega)}\leq O(\tau^q)\,, \tag{77}$$

where $n_e(t^n)$ and $\varphi(t^n)$ represent the exact solutions to the time integration problem. Such exact solutions, $n_e(t^n)$ and $\varphi(t^n)$, are assumed to satisfy the constraint $-\varepsilon\Delta\varphi(t)=q_e n_e(t)+q_b n_b(t)$ for all time $t\in[0,t_F]$. We define the Gauss-law residual $\mathcal{R}^n\in H^{-1}(\Omega)$ of the approximate solution as

$$\mathcal{R}^n:=\varepsilon\Delta\varphi^n+q_e n_e^n+q_b n_b^n\,. \tag{78}$$

Then, it follows that $\|\mathcal{R}^n\|_{H^{-1}(\Omega)}\leq O(\tau^q)$.

Proof. By definition of $H^{-1}(\Omega)$-norm we have

$$\begin{aligned}
\|\mathcal{R}^n\|_{H^{-1}(\Omega)} &= \sup_{\{\omega\in H^1\,|\,\|\omega\|_{H^1}=1\}} \langle\varepsilon\Delta\varphi^n+q_e n_e^n+q_b n_b^n,\omega\rangle\\
&= \sup_{\{\omega\in H^1\,|\,\|\omega\|_{H^1}=1\}} \langle\varepsilon\Delta\varphi^n+q_e n_e^n+q_b n_b^n-\underbrace{[\varepsilon\Delta\varphi(t^n)+q_e n_e(t^n)+q_b n_b(t^n)]}_{\equiv 0},\omega\rangle\\
&= \sup_{\{\omega\in H^1\,|\,\|\omega\|_{H^1}=1\}} \varepsilon(\nabla\varphi(t^n)-\nabla\varphi^n,\nabla\omega)+q_e(n_e^n-n_e(t^n),\omega)\\
&\leq \sup_{\{\omega\in H^1\,|\,\|\omega\|_{H^1}=1\}} \varepsilon(\nabla\varphi(t^n)-\nabla\varphi^n,\nabla\omega)+q_e\sup_{\{\omega\in H^1\,|\,\|\omega\|_{H^1}=1\}} q_e(n_e^n-n_e(t^n),\omega)\\
&\leq \varepsilon\|\nabla\varphi(t^n)-\nabla\varphi^n\|_{L^2(\Omega)}+q_e\sup_{\omega\in L^2(\Omega),\|\omega\|_{L^2(\Omega)}=1}(n_e^n-n_e(t^n),\omega)\\
&\leq \varepsilon\|\nabla\varphi(t^n)-\nabla\varphi^n\|_{L^2(\Omega)}+q_e\|n_e^n-n_e(t^n)\|_{L^2(\Omega)}
\end{aligned}$$

where we have used that the exact solution $\{n_e(t^n),\varphi(t^n)\}$ satisfies the Gauss-law exactly, the fact that $n_b(t^n)$ and n_b^n are equal in the semi-discrete context, integration by parts in order to rewrite the $\langle H^{-1},H^1\rangle$ pairing in terms of a Riesz representative, sub-additivity of the sup, and the monotonicity property $\sup_{H^1}\leq\sup_{L^2}$. The result follows readily applying the assumed estimate (77). ☐

The following lemma shows that Step #1 of Algorithm 5, computing a new potential φ_g that satisfies the Gauss-law, cannot be too different from the original potential delivered by our q-th order accurate scheme.

Lemma B.2 (Projection error)**.** *Let n_e^n and φ^n represent the solutions returned by a numerical scheme of q-th order of accuracy, see* (77)*. Let us define φ_g^n as the solution of*

$$-\varepsilon\Delta\varphi_g^n=q_e n_e^n+q_b n_b^n\,. \tag{79}$$

Then, under the assumptions of Lemma B.1, we have that

$$\varepsilon\|\nabla\varphi_g^n-\nabla\varphi^n\|_{L^2(\Omega)}\leq O(\tau^q)\,. \tag{80}$$

Proof. Subtracting (79) from (78) we get

$$-\varepsilon(\Delta\varphi_g^n - \Delta\varphi^n) = \mathcal{R}^{n+1}.$$

Taking the duality pairing with $\varphi_g^n - \varphi^n$ we get

$$\begin{aligned}\varepsilon\|\nabla\varphi_g^n - \nabla\varphi^n\|^2_{L^2(\Omega)} &= \langle \mathcal{R}^{n+1}, \varphi_g^n - \varphi^n \rangle \\ &\leq \|\mathcal{R}^n\|_{H^{-1}}\|\varphi_g^n - \varphi^n\|_{H^1} \\ &\lesssim \|\mathcal{R}^n\|_{H^{-1}}\|\nabla\varphi_g^n - \nabla\varphi^n\|_{L^2},\end{aligned}$$

where we used Poincare's inequality in the last step. The result follows by cancelling a factor of $\|\nabla\varphi_g - \nabla\varphi^n\|_{L^2}$ and using the decay rate for $\|\mathcal{R}^{n+1}\|_{H^{-1}}$ established in Lemma B.1. ☐

The following lemma shows that Step #3 of Algorithm 5, computing a new potential that is a convex combination of the projected potential and the original q-order potential, should be q-order accurate too.

Proposition B.1 (Accuracy of linear combinations). *Let n_e^n and φ^n represent the solutions returned by a numerical scheme of q-th order of accuracy. Let λ be any real number of order* $O(1)$. *Under the assumptions of Lemma B.1 we have that*

$$\|[\lambda\nabla\varphi_g^n + (1-\lambda)\nabla\varphi^n] - \nabla\varphi(t^n)\|_{L^2(\Omega)} \leq O(\tau^q) \tag{81}$$

with φ_g^n as defined in (79) *and $\varphi(t^n)$ being the exact solution of our time-integration process.*

Proof. The proof is rather trivial and follows by using $1 = \lambda + (1-\lambda)$ and the triangle inequality:

$$\begin{aligned}&\|[\lambda\nabla\varphi_g^n + (1-\lambda)\nabla\varphi^n] - \nabla\varphi(t^n)\|_{L^2(\Omega)} = \\ &\quad \|\lambda[\nabla\varphi_g^n - \nabla\varphi(t^n)] + (1-\lambda)[\nabla\varphi^n - \nabla\varphi(t^n)]\|_{L^2(\Omega)} \\ &\quad \leq \lambda\|\nabla\varphi_g^n - \nabla\varphi(t^n)\|_{L^2(\Omega)} + |1-\lambda|\|\nabla\varphi^n - \nabla\varphi(t^n)\|_{L^2(\Omega)} \\ &\quad \leq \lambda\|\nabla\varphi_g^n - \nabla\varphi^n\|_{L^2(\Omega)} + \lambda\|\nabla\varphi^n - \nabla\varphi(t^n)\|_{L^2(\Omega)} + |1-\lambda|\|\nabla\varphi^n - \nabla\varphi(t^n)\|_{L^2(\Omega)}.\end{aligned} \tag{82}$$

The three terms in (82) are estimated using (80), assumptions (77), and boundedness of λ and $1-\lambda$. ☐

In conclusion: estimate (81) tells us that any linear combination of potential computed by Gauss-law-restart indeed introduces and error, but this error is $O(\tau^q)$, therefore it cannot not hurt the asymptotic accuracy of the whole scheme. Finally, we would like to have an estimate on the total energy of the system, in particular the electrostatic energy, after restart.

Lemma B.3 (Energy difference). *Let n_e^n and φ^n represent the solutions returned by a numerical scheme of q-th order of accuracy, see* (77). *Assume that*

$$\|n_b^n\|_{L^2(\Omega)} + \|n_e^n\|_{L^2(\Omega)} + \|\nabla\varphi^n\|_{L^2(\Omega)} \leq const < \infty \tag{83}$$

Under the assumptions of the Lemma B.1 we have that

$$\varepsilon\left|\|\nabla\varphi^n\|^2_{L^2(\Omega)} - \|\nabla\varphi_g^n\|^2_{L^2(\Omega)}\right| \leq O(\tau^q)$$

where φ_g^n was defined in (79).

Proof. From (78) and (79) we have that

$$\begin{aligned}
\varepsilon\|\nabla\varphi^n\|^2_{L^2(\Omega)} &= (q_e n_e^n + q_b n_b^n, \varphi^n) - \langle \mathcal{R}^n, \varphi^n\rangle\,,\\
\varepsilon\|\nabla\varphi_g^n\|^2_{L^2(\Omega)} &= (q_e n_e^n + q_b n_b^n, \varphi_g^n)\,.
\end{aligned}$$

Taking their difference we get

$$\begin{aligned}
\varepsilon(\|\nabla\varphi_g^n\|^2_{L^2(\Omega)} - \|\nabla\varphi^n\|^2_{L^2(\Omega)}) &= (q_e n_e^n + q_b n_b^n, \varphi_g^n - \varphi^n) + \langle \mathcal{R}^n, \varphi^n\rangle\,,\\
&\lesssim (\|n_e^n\|_{L^2(\Omega)} + \|n_b^n\|_{L^2(\Omega)})\|\nabla\varphi_g^n - \nabla\varphi^n\|_{L^2(\Omega)} + \|\nabla\varphi^n\|_{L^2(\Omega)}\|\mathcal{R}^{n+1}\|_{H^{-1}}\\
&\lesssim \|\nabla\varphi_g^n - \nabla\varphi^n\|_{L^2(\Omega)} + \|\mathcal{R}^n\|_{H^{-1}}\,.
\end{aligned}$$

where we have used Poincare inequalities and the assumed bounds (83). The result follows using the convergence rate (80) and the decay rate of the Gauss-law residual $\|\mathcal{R}^n\|_{H^{-1}} \leq O(\tau^q)$. ☐

APPENDIX C. GRAPH-BASED HYPERBOLIC SOLVER

For the hyperbolic subsystem (23) we use a framework of numerical schemes based on a graph-viscosity stabilization and convex limiting [51, 49, 53, 66, 47]. The framework is discretization agnostic, meaning that it can in principle be used in conjunction with continuous or discontinuous finite element, finite volume, or finite difference formulations. In this report, however, we will use a discontinuous finite element spaces, see Section 4.2, for reasons discussed in Remark 4.6 related to local well-posedness of the linear algebra system. For the sake of completeness we summarize some implementation aspects in this appendix. For a complete overview of the methodology we refer the reader to [53].

C.1. Discrete divergence operator and stencil

For every $i \in \mathcal{V}_H(K)$ and every $j \in \mathcal{V}_H$ we define the vector $\mathbf{c}_{ij} \in \mathbb{R}^d$ as

$$\mathbf{c}_{ij} := \begin{cases} \mathbf{c}_{ij}^K - \mathbf{c}_{ij}^{\partial K} & \text{if } j \in \mathcal{V}_H(K),\\ \mathbf{c}_{ij}^{\partial K} & \text{if } j \in \mathcal{V}\backslash\mathcal{V}_H(K),\end{cases}$$

where

$$\mathbf{c}_{ij}^K := \int_K \phi_i \nabla\phi_j \,\mathrm{d}\boldsymbol{x}, \qquad \mathbf{c}_{ij}^{\partial K} := \frac{1}{2}\int_{\partial K\backslash\partial\Omega} \phi_j\phi_i \mathrm{n}_K \,\mathrm{d}\boldsymbol{s}.$$

where n_K is the outwards pointing normal of the element K. Note that: $\mathbf{c}_{ij}^{\partial K}$ will be necessarily zero if ϕ_j does not have support on the element K or on one of its immediate neighbors. With this observation in mind, we define the stencil at the node i as follows:

$$I(i) = \{j \in \mathcal{V}_H \mid \mathbf{c}_{ij} \neq 0\}.$$

The set of vectors $\{\mathbf{c}_{ij}\}_{j\in I(i)}$ is used to construct an approximation of the divergence operator at each node i in the spirit of a collocation scheme [53]. We highlight that this approximation of the divergence operator is consistent with the polynomial degree of the shape functions $\{\phi_i\}_{i\in\mathcal{V}_H}$ and will work with arbitrary meshes, see [53] for more details.

C.2. Scheme

For a given state $\mathbf{U}_i^n = [\rho_i, \mathbf{p}_i]^\top$ we define a low-order update $\mathbf{U}_i^{n+1,\mathrm{L}}$ approximating the solution of (23) as follows:

$$m_i \frac{\mathbf{U}_i^{n+1,\mathrm{L}} - \mathbf{U}_i^n}{\tau} + \sum_{j \in I(i)} \mathbb{f}(\mathbf{U}_j^n)\, \mathbf{c}_{ij} - d_{ij}^{n,\mathrm{L}}(\mathbf{U}_j^n - \mathbf{U}_i^n) = 0, \text{ for all } i \in \mathcal{V}_H, \tag{84}$$

where we have set $m_i = \int_\Omega \phi_i \,\mathrm{d}\boldsymbol{x}$, and where $\mathbb{f}(\mathbf{U}_j^n) \in \mathbb{R}^{(d+1)\times d}$ is the flux at the node $j \in I(i)$, and $d_{ij}^{n,\mathrm{L}} \in \mathbb{R}^+$ is a viscosity coefficient defined as

$$d_{ij}^{n,\mathrm{L}} := \max\{\lambda^{\max}(\mathbf{U}_i^n, \mathbf{U}_j^n, \mathbf{n}_{ij})|\mathbf{c}_{ij}|_{\ell^2}, \lambda^{\max}(\mathbf{U}_j^n, \mathbf{U}_i^n, \mathbf{n}_{ji})|\mathbf{c}_{ji}|_{\ell^2}\}\,.$$

Here, $\lambda^{\max}(\mathbf{U}_L, \mathbf{V}_R, \mathbf{n})$ is any upper-bound on the maximum wavespeed of propagation of the projected-Riemann problem (setting $x := \boldsymbol{x} \cdot \mathrm{n}$):

$$\partial_t \mathbf{U} + \partial_x(\mathbb{f}(\mathbf{U}) \cdot \mathrm{n}) = 0 \quad \text{with initial data} \quad \mathbf{U}_0 = \begin{cases} \mathbf{U}_L & \text{if } x \leq 0, \\ \mathbf{U}_R & \text{if } x > 0, \end{cases}$$

and we set $d_{ii}^{n,\mathrm{L}} = -\sum_{j \in I(i)\setminus\{i\}} d_{ij}^{n,\mathrm{L}}$. Then, under the hyperbolic *cfl* condition

$$\tau_n := -\mathrm{c}_{cfl} \min_{i \in \mathcal{V}_H} \Big(\frac{m_i}{2 d_{ii}^{n,\mathrm{L}}} \Big), \tag{85}$$

for some user selected $\mathrm{c}_{cfl} \in (0,1]$ the update $\mathbf{U}_i^{n+1,\mathrm{L}}$ as defined by (84) preserves the invariant domain and all entropy inequalities, see [51, 53].

C.3. High-order update and convex limiting

We also introduce a corresponding high-order method,

$$m_i \frac{\mathbf{U}_i^{n+1,\mathrm{H}} - \mathbf{U}_i^n}{\tau_n} + \sum_{j \in I(i)} \mathbb{f}(\mathbf{U}_j^n)\, \mathbf{c}_{ij} - d_{ij}^{n,\mathrm{H}}(\mathbf{U}_j^n - \mathbf{U}_i^n) = 0,$$

where the only difference with the low-order scheme (84) lies in the choice of a high-order viscosity $d_{ij}^{n,\mathrm{H}}$. The high-order graph viscosities are typically constructed such that $d_{ij}^{n,\mathrm{H}} \approx d_{ij}^{n,\mathrm{L}}$ near shocks and discontinuities, but $d_{ij}^{n,\mathrm{H}} \approx 0$ in smooth regions of the solution. A possible choice is to construct local indicators estimating the entropy production or local smoothness of the solution and use those to construct the high-order viscosity [52, 49]. In the computations reported in this manuscript, however, we use a rather simple approach to compute the high-order viscosities

$$d_{ij}^{n,\mathrm{H}} = \begin{cases} d_{ij}^{n,\mathrm{L}} & \text{if } \boldsymbol{x}_i = \boldsymbol{x}_j, \\ 0 & \text{otherwise.} \end{cases}$$

This definition is equivalent to using the low-order viscosity only on the faces of the elements. We observe numerically good convergence rates for $\mathbb{P}^1$ and $\mathbb{Q}^1$ elements. However, the high-order solution $\mathbf{U}_i^{n+1,\mathrm{H}}$ is not guaranteed to be invariant domain preserving and cannot be used directly [49, 53]. In order to maintain invariant domain preservation and the high approximation properties we blend the low-order solution and high-order solution together in a post-processing step by setting

$$\mathbf{U}_i^{n+1} = \mathbf{U}_i^{n+1,\mathrm{L}} + \sum_{j \in I(i)} \ell_{ij} \mathbf{A}_{ij} \quad \text{with} \quad \mathbf{A}_{ij} := \tau_n (d_{ij}^{n,\mathrm{H}} - d_{ij}^{n,\mathrm{L}})(\mathbf{U}_j^n - \mathbf{U}_i^n).$$

Here, the limiter matrix $\ell_{ij} \in [0,1]$ is computed using a convex limiting procedure that consisting of directional line searches that ensures that $\mathbf{U}_i^{n+1}$ remains in the invariant set, see [49, 53] for more details.

DISTRIBUTION

Hardcopy—External

Number of Copies	Name(s)	Company Name and Company Mailing Address

Hardcopy—Internal

Number of Copies	Name	Org.	Mailstop

Email—External (encrypt for OUO)

Name	Company Email Address	Company Name

Email—Internal (encrypt for OUO)

Name	Org.	Sandia Email Address
Technical Library	1911	sanddocs@sandia.gov

Sandia
National
Laboratories